AD-A130 408   EXPERIMENTS ON THE DYNAMICS AND HYDRODYNAMIC   1/ 3
                INSTABILITIES OF ABLATIVELY ACCELERATED TARGETS(U)
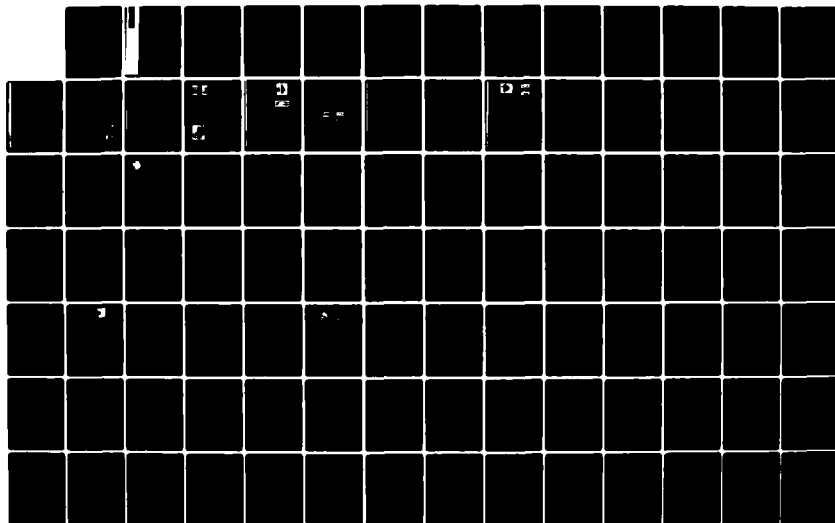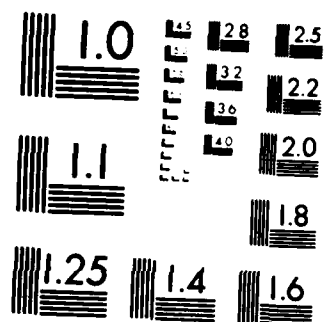   MISSION RESEARCH CORP ALEXANDRIA VA   FEB 83
UNCLASSIFIED   MRC/WDC-R-050 SBI-AD-E001 441   F/G 20/9   NL

MICROCOPY RESOLUTION TEST CHART
NATIONAL BUREAU OF STANDARDS 1963 A

ADA130409

TECHNICAL REPORT

Experiments on the Dynamics and
Hydrodynamic Instabilities of Ablatively
Accelerated Targets

February 1983

Submitted to: Naval Research Laboratory
Code 4730
4555 Overlook Avenue, SW
Washington, DC 20375

Attention: Dr. Barrett Ripin

DTIC
SELECTED
JUL 1 4 1983

A

MISSION RESEARCH CORPORATION
5503 Cherokee Avenue, Suite 201
Alexandria, Virginia 22312
(703) 750-3556

DTIC FILE COPY

83 06 24 012

Copy _11_   MRC/WDC-R-050

TECHNICAL REPORT

Experiments on the Dynamics and
Hydrodynamic Instabilities of Ablatively
Accelerated Targets

February 1983

Submitted to: Naval Research Laboratory
               Code 4730
               4555 Overlook Avenue, SW
               Washington, DC 20375

Attention: Dr. Barrett Ripin

MISSION RESEARCH CORPORATION
5503 Cherokee Avenue, Suite 201
Alexandria, Virginia   22312
        (703) 750-3556

TABLE OF CONTENTS

INTRODUCTION

The Laser-Plasma Interaction group at NRL is evaluating for the Department of Energy the feasibility of using direct laser drive to implode fusion pellets.[†] Mission Research Corporation (MRC) has contracted to support this experiment by using its best effort to perform the tasks summarized below:

- A parametric study shall be performed using the double foil technique on actual laser-foil experiments. Design parameters, to be varied as needed, include laser intensity, material and thickness of the first foil, material and thickness of the second foil, and the spacing between foils. Notched-edge configurations will also be investigated.

- In support of the above task, other diagnostic measurements will be performed. Such diagnostics include calorimeters, Faraday cups, and ballistic pendula.

- Analytical techniques and methods analyzing the experimental data will be developed and implemented on the existing PDP-11/10 system.

- We will investigate whether the x-ray tracer technique ... is suitable to track plasma flow from targets accelerated to high velocities. We will also investigate whether this technique is suitable for the study of plasma hydrodynamic instabilities. For this purpose we will experiment with target and tracer materials that are density matched and at the same time maintain a sufficient tracer/target x-ray emission contrast. We will also use plasma

---

[†] B. H. Ripin et al., Phys. Fluids 23(5), 1012 (1980); 24, 990 (E) (1981).

calorimeters and ion collectors to investigate laser absorption in long-density-scalelength plasmas. These studies will include, as needed, parametric variations of laser intensity, laser energy, laser profile, target thickness, and target density. We will operate and develop software for the 4052 Tektronix data acquisition system if this becomes necessary for the above experiments.

- Mission Research Corporation (MRC) will interface existing NRL x-ray detectors and particle detectors with digital data acquisition systems which are owned by NRL. MRC will operate, maintain, and upgrade these systems for the purpose of investigating the properties of laser interaction with matter. Software will be developed for these systems if necessary for the above experiment.

- The data obtained in the above tasks will be reduced and analyzed.

The following sections summarize our fulfillment of these tasks. Details are provided in the appendices.

DOUBLE-FOIL AND NOTCHED-EDGE EXPERIMENTS

Experiments using double-foils and notched-edge configurations have been performed. In particular:

- The validity of the double-foil method was verified using clear double-foils and x-ray backlighting methods.

- A low density plasma traveling ahead of the accelerated target has been identified and diagnosed.

- A triple-foil configuration was used to diagnose the impact foil.

- Target speeds up to 160 km/sec have been measured.

- Target pressure has been measured using the double-foil technique. These measurements verify earlier results obtained with ballistic pendula, plasma calorimeters, and ion collectors.

- The relationship between irradiance uniformity and target velocity uniformity was measured.

- A notched double-foil configuration was used to diagnose shocks in the impact foil.

Appendix A provides more details.

ABLATION-PLASMA ION MEASUREMENTS

Earlier experiments which inferred target pressure from measurements on the ablation plasma were compared to more recent experiments which inferred target pressure from its acceleration as measured with x-ray backlighting. Good agreement was found.

Appendices B an C provide more details.

ANALYSIS OF ION MEASUREMENTS

A program called MINCAL was written to analyze plasma calorimeter data aquired by NRL's PDP-11/10-based data acquisition system. MINCAL is a flexible, user-oriented program with the following features:

- Parameters are stored permanently on disk.

- The program provides options to list and/or change parameters.

- Energy and velocity data reduction is possible.

- Plots are done on a line printer using a line printer graphics (LPG) routine.

- Program stores all system constants (amplifier gain, etc.) and automatically reduces data to absolute values.

- Program reduces plasma calorimeter data, interpolates between data points, and plots energy and velocity versus angle.

- Program outputs useful calculations for user: $\theta_{1/2}$ (angle containing half the mass, momentum versus angle, others as specified by the user).

- Program is designed to easily incorporate new data reduction routines.

- Program is implemented on the DEC-10 and the PDP-11/10.

Program Listing is provided in Appendix D.

TRACER METHOD

The tracer method, coinvented by an MRC employee (J. Grun), has been used to study the ablation plasma flow from planar targets irradiated by uniform and perturbed laser beams. The experiment:

- Discovered that the ablating plasma flows away from the target as if it were an incompressible fluid.

- Explained the angular distribution of ablation plasma momentum, velocity, and mass as measured by diagnostics placed far from the target.

- Provided qualitative evidence for velocity smoothing caused by thermal conduction in the overdense ablation plasma.

Initial experiments to spectrally and spacially resolve the emission from a planar target irradiated by a nonuniform laser beam have been performed. From such measurements, the temperature and density of the plasma along the target surface may be resolved and, thus, the "cloudy day effect" may be quantitatively studied.

MRC has applied the tracer method to the study of hydrodynamically unstable targets. This aspect of our work will be discussed below.

MRC has also helped to use tracers to make local spectroscopic measurements within laser-produced plasmas. This application of the tracer method constitutes a major advance in plasma spectroscopy, since it potentially eliminates problems of interpreting spectra originating from regions of varying density and temperature in an inhomogeneous plasma and reduces complications due to plasma opacity.

Appendices A, E, and F provide more detail.

5

TEKTRONIX DATA ACQUISITION SYSTEM AND SOFTWARE

MRC recommended the purchase of a data acquisition system consisting of a Tektronix 4052 computer, 4907 disk drive, 7612D digitizers, 4631 hard copy unit, and an HP-IB 37203A extender. The installation and operation of this system was overseen by MRC. This system is being used to acquire ion time-of-flight data and plasma calorimeter data.

The data acquisition software for this system was custom built by Tektronix to MRC specifications. Subsequently, the Tektronix program was modified by MRC to help on-line analysis of the data. A listing of this software is in Appendix G.

Other software written to aid analysis of the data includes two programs to reduce focal spot size data (Appendix H) and a program used to calculate the speed and the number of classical Rayleigh-Taylor e-foldings of an ablatively-accelerated target (Appendix I).

TARGETS AND TRACERS FOR RAYLEIGH-TAYLOR EXPERIMENTS

MRC suggested that tracers embedded in perturbed targets be used to study the ablation plasma flow characteristic of hydrodynamically unstable targets. In our opinion these targets should have the following characteristics - some of which are necessary, others desirable:

- Targets should have uniform density.

- Periodic structure should have a wavelength $\geq 10 \mu m$ and perturbation magnitude of 0-2.

- Tracer emission should be significantly larger than target emission in the energy band being measured.

- Target perturbation period should be larger than the tracer period for acceptable resolution.

- Tracers should not perturb target areal density.

- Tracers should not perturb the dynamics of the ablation plasma (for example ρv^2 should be the same for the target and the tracer).

- It is desirable that the tracer period match the perturbation period for some experiments.

- It is desirable that the target manufacturing methods match the capabilities of the target fabrication group at NRL. In particular polystyrene targets are desirable since this group has had extensive experience making them.

MRC has evaluated over 40 materials for their suitability and has examined various manufacturing methods. We found that carbon targets with silicon or aluminum tracers met all our criteria except the last. To extend the capabilities of the NRL target fabrication group MRC located a used, ion-mill machine which was purchased by NRL permitting the manufacture of the above targets.

EXPERIMENTAL METHODS FOR RAYLEIGH-TAYLOR MEASUREMENTS

In addition to the tracer method as applied to the Rayleigh-Taylor problem, MRC invented a magnesium-layer method that may provide a measurement of the Rayleigh-Taylor growth rate.

The tracer and magnesium-layer methods and initial experiments are described in Appendix J.

LONG SCALELENGTH EXPERIMENTS

MRC has participated in long scalelength experiments in support of the NRL effort. Details are provided in Appendix K.

X-RAY DETECTORS

The existing NRL x-ray data acquisition system has been upgraded and operated by MRC. In particular:

- The detectors and their associated electronics have been reconfigured (with the addition of several new components and electrical shielding) in order to eliminate a pre-existing electrical noise problem.

- The x-ray detectors have been operated in conjunction with the NRL long-scalelength experiments.

- MRC has maintained and upgraded the NRL's PDP-11/10 computer system and software. This has included the purchase and installation of a new RT-11 operating system, as well as streamlining the computer interface for more reliable operation.

- A program titled PADCAL has been written to facilitate calibration of the x-ray detector system. This program has significantly reduced both the time and effort previously required in the performance of this task and allows calibrations to be performed much more frequently in the course of an experiment.

- MRC has investigated available options towards the possibility of integrating the Tektronix 4052 and PDP-11/10 data acquisition systems into a single, coherent system. These options will be considered by NRL personnel for future implementation.

APPENDIX A

Ablative acceleration of planar targets to high velocities

J. Grun,[a] S. P. Obenschain, B. H. Ripin, R. R. Whitlock, E. A. McLean, J. Gardner, M. J. Herbst,
and J. A. Stamper

Naval Research Laboratory, Washington, D. C. 20375

Laser irradiated targets are ablatively accelerated to velocities near those required for fusion pellet implosions while remaining relatively cool and uniform. The target velocities and velocity profiles are measured using a double-foil method, which is described in detail. Also, the ablation plasma flow from the target surface is spatially resolved, and the scalings with absorbed irradiance of the ablation pressure, ablation velocity, and mass ablation rate are determined. Results are compared with hydrodynamic code calculations.

I. INTRODUCTION

One approach to inertial confinement fusion involves the use of a multi-nanosecond, moderate-irradiance laser pulse to implode a hollow pellet containing DT fuel.[1] If this concept is to succeed, the imploding pellet shell must be efficiently and uniformly accelerated to a high velocity, and the DT fuel must be kept cool. Only then will the pellet compress to densities sufficient for a high gain thermonuclear burn.

In this paper, we describe experiments which utilize ablatively accelerated planar targets to model large pellet shells early in the implosion phase. We have made detailed measurements of the motion of such targets[2,3,4] and of the ablation plasma that accelerates them.[2,5,6] These measurements include: emitted light studies; visible light shadowgraphy and x-ray shadowgraphy on a novel target-impact foil (double-foil) configuration which is used to determine the mean velocities and velocity profiles of the dense part of the accelerated target, to study irradiance symmetrization, and to study double-foil interactions; diagnosis of the impact foil using a triple-foil configuration; spatially resolved studies of the ablation plasma flow from uniformly and nonuniformly irradiated targets; as well as measurements of the ablation plasma pressure, velocity, and mass ablation rate. The target velocity, velocity profiles, and the temperature of the target rear have been studied as a function of target thickness, irradiance, and irradiance uniformity. We have accelerated relatively cool and uniform targets to velocities of 160 km/sec— a velocity which is above the minimum thought to be required for laser fusion.[1] Our experimental results are compared to hydrodynamic code calculations.

The experimental arrangement is described in Sec. II. Measurements on the accelerated target are described in Sec. III; and measurements of the ablation parameters are described in Sec. IV. Conclusions are offered in Sec. V.

II. EXPERIMENTAL ARRANGEMENT

These experiments are performed using the NRL Pharos II Nd:glass laser ($\lambda = 1.05 \mu$m) which has been described elsewhere.[7] The laser beam is typically focused to a large diameter ($\simeq 1$ mm) spot on the target surface by a 1.2

m, f/6 aspheric lens. Such large diameter, quasinear field laser spots are used whenever possible to maximize irradiance uniformity and to minimize focal-spot-edge effects.[2,5,8] Irradiance profiles, such as those shown in Fig. 1, are measured on each discharge in an equivalent target plane.[9] These profiles are fairly uniform with small and large scale peak-to-valley variations of about $\pm$ 35%. Unless otherwise stated, irradiance is varied by adjusting the laser energy and not by changing the focal spot size. The laser pulse duration is 3–5 nsec FWHM.
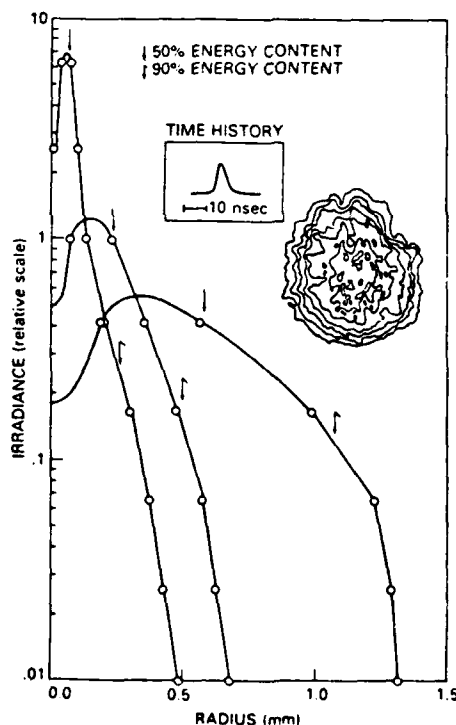

FIG. 1. Azimuthally averaged radial intensity profiles at the target plane. Focal-spot radius is varied by moving the focusing lens. Arrows indicate radii within which 50% or 90% of the energy is contained. Inserts show the temporal behavior of the laser pulse and constant irradiance contours of a 1-mm diameter laser spot.

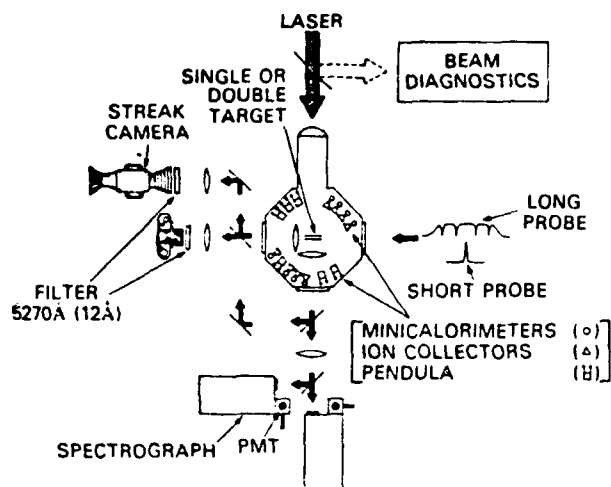[a] Present address: Mission Research Corporation, Alexandria, Virginia.

FIG. 2. Sketch of the experimental setup

Figure 2 shows the experimental arrangement. The target normal is tilted 6° from the laser axis to make it experimentally accessible. Surrounding the target are arrays of plasma calorimeters, *in-situ* calibrated ballistic pendula,[2] and time-of-flight ion collectors which monitor the ablation plasma and target energies, momenta, and velocities, respectively. (In this long pulse regime ion collector traces are narrow and single peaked, making them ideal for time-of-flight measurements.) From the angular distributions of these quantities we infer the ablation pressures, mass ablation rates, and ablation velocities. Although any two of the measured quantities are sufficient to calculate the third, we measure all three with independent diagnostics to verify the consistency and validity of the results. Spatially resolved pictures of the ablation plasma flow are also obtained using tracer elements deposited in the target surface.

Temporally and spatially resolved measurements of the target motion are made using a double-foil technique. This method consists of placing a thin foil (impact foil) behind the laser accelerated target and observing the reaction of the impact foil to its collision with the target (Fig. 3). We observe the two-foil interaction in three ways: (1) from the side with optical shadowgraphy or optical streaking (Fig. 2), (2) from
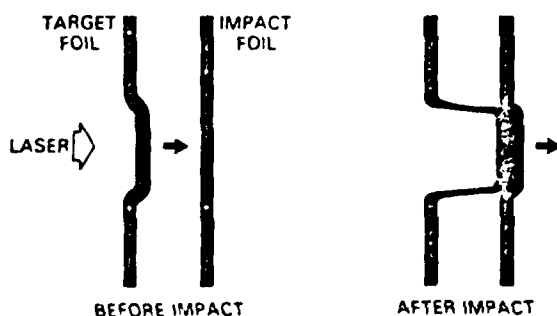
the side using an x-ray backlighter, and (3) from the rear recording light emitted by the impact foil when it collides with the target (Fig. 2). The details of particular double-foil configurations depend on the intent of the specific experiment and will be discussed in later sections.

Temporally resolved temperature at the rear surface of the accelerated target is determined by comparing the absolute visible continuum emission from the target's rear to black body emission.[10] The continuum intensity is measured at two different wavelengths using 3/4-m spectrographs coupled to 1-nsec risetime photomultipliers.

III. TARGET DYNAMICS

In earlier studies of ablative acceleration we inferred the target velocity from the velocity of its debris measured with time-of-flight ion collectors, and from the velocity of its optical shadow.[8] Each of these methods however, has limitations. Ion collectors, for example, measure properties of the target very far from its acceleration region, while optical shadowgraphs can not distinguish the high density part of the target from any low density plasma that may precede it. In the present work we use a double-foil technique[11] that discriminates against such a low density plasma, and permits temporally and spatially resolved diagnosis of the dense part of the target. Double foils may also be used to investigate hypervelocity impact phenomena such as the generation of ultra high pressures[12] or to model double-shell fusion pellets.

With the double-foil method, the target velocity is determined from its flight time to the impact foil, placed a known distance away. The flight time, in turn, is determined by noting the moment at which the impact foil reacts to its collision with the target. Such reaction includes any of the observable phenomena normally associated with collisions—for example, spall or fluff from the rear of the impact foil, movement or deformation of the impact foil, or visible light emission from its rear surface. The target position as a

FIG. 3 Schematic of the double-foil concept. Behavior of the laser accelerated target is inferred from the response of the impact foil to the collision.
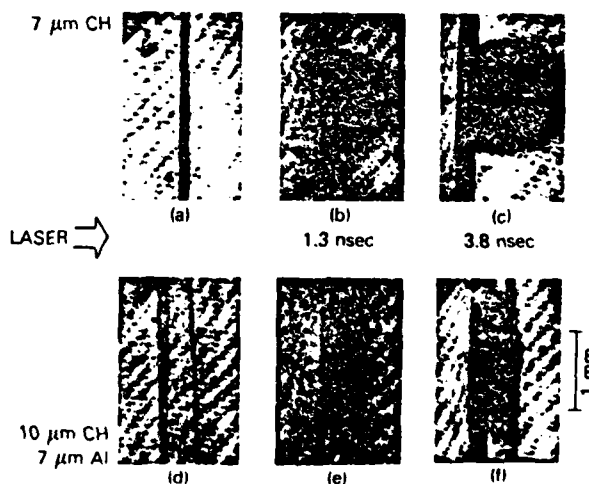
FIG. 4 Optical shadowgraphs of a single (a,b,c) and a double-foil (d,e,f) target irradiated at 5×10^{13} W/cm². The times notes are relative to the peak of the laser pulse. Photographs b, c, and e, f are taken during the same discharge.

function of time is measured by varying the initial target-impact foil spacing, thereby controlling the instant of collision. In this manner we can diagnose the target during as well as after its acceleration phase. Also, the visible light emission from the rear of the impact foil gives spatial resolution along the target surface so that the relationship between velocity and irradiance uniformity may be studied.

The choice of the target and impact-foil material, their dimensions, and the spacings between the two foils depend on the purpose of the experiment. To infer target velocities, for example, it is desirable that the impact foil be thin enough so that the sound-transit-time through it is very short compared to the flight time of the target. In this case, the sound-transit-time may be ignored, and the collision time of the target with the front surface of the impact foil is directly related to the reaction of the impact foil's rear surface.

The ability of the double-foil method to discriminate against a low density plasma preceding the dense part of the target is demonstrated in Fig. 4. Here, we compare shadows cast by a single and a double-foil target that are temporally resolved by multiple-frame shadowgraphy using a 0.5 nsec, 5270-Å laser probe flash. Both types of targets are photographed before, as well as 1.3 nsec, and 3.8 nsec after the peak of the laser pulse. Figures 4(a), (b), and (c) show shadowgraphs of the single target which is a 7-μm thick CH foil. The shadow of this target moves with a velocity of 1.6×10^7 cm/sec and traverses a distance of about 400 μm in 2.5 nsec. Figures 4(d), (e), and (f) show a corresponding sequence for the double foil which is composed of a 10-μm thick CH target and a 7-μm thick aluminum impact foil. Note that although the target shadow has already reached the impact foil in Fig. 4(e), the impact foil itself does not react at this time. In fact, the first indication of the impact foil's reaction occurs in Fig. 4(f)—more than 2.5 nsec after the optical shadow of the accelerated target reached the impact foil. Since the shock-transit-time through the impact foil is less than 1.4 nsec (sound speed in cold Al is 5×10^5 cm/sec), much of this delay is caused by the material in the leading edge of the target shadow exerting insufficient pressure for the impact foil to react. Because the pressure exerted by a moving mass is proportional to its density, we conclude that the leading edge of the accelerated target shadow is composed of low density material. This low density material obscures the dense part of the accelerated target from optical shadow-
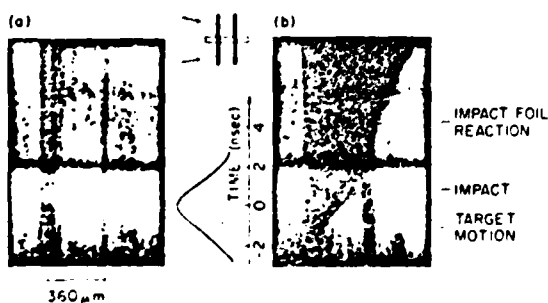
graphy and interferometry diagnostics, but is discriminated against with the double-foil method.

Another way to view the delayed reaction of the impact foil is presented in Fig. 5, which shows the streak record of a double-foil collision backlit by a 10-nsec, 5270-Å laser probe. This one-dimensional, but temporally continuous, shadowgraph shows the low density plasma advancing toward the impact foil, the low density plasma-impact foil collision, and the reaction of the impact foil when the dense part of the accelerated target finally strikes. The sudden reaction time ($\simeq 0.5$ nsec) of the impact foil suggests a localized, dense accelerated target. The time of the dense target-impact foil collision is, therefore, a good marker for the target time-of-flight.

We determine a target velocity by varying the initial target-impact foil separation and accumulating distance traveled versus time-of-travel data for many discharges. Such data for 7-μm thick and 10-μm thick CH targets irradiated at 6×10^{12} W/cm^2 are shown in Fig. 6. For most of these cases, the target-impact foil separation is large enough so that the collision occurs after the ablative acceleration phase is nearly over. Therefore, the data for each target thickness lie on a straight line whose slope is the final target velocity. Velocities obtained in this way agree with predictions based upon measurements of the ablation momentum (pressure), mass ablation rate (Sec. IV) and momentum conservation, and with the predictions of a hydrodynamic code described below. However, they are significantly lower than the low density plasma velocities inferred from the motion of the target's optical shadow in the double-foil streak pictures. Averaged over many discharges, the ratio of the optical shadow velocity to dense target velocity is 2 ± 0.8, with the spread mostly due to discharge-to-discharge variations in the low density plasma velocity. This ratio is consistent with the leading edge of the low density plasma being caused by spall or fluff from the unloading of a shock at the target's rear surface.[13]

Like the target shadow, the impact-foil shadow is also cast by low density material and not by the dense part of the impact foil. Thus, the acceleration of the impact foil or the

FIG 5. Streaked optical shadows of a target colliding with an impact foil: (a)—before discharge, and (b)—after discharge. The target is 7-μm thick CH and the impact foil is 7-μm thick Al.
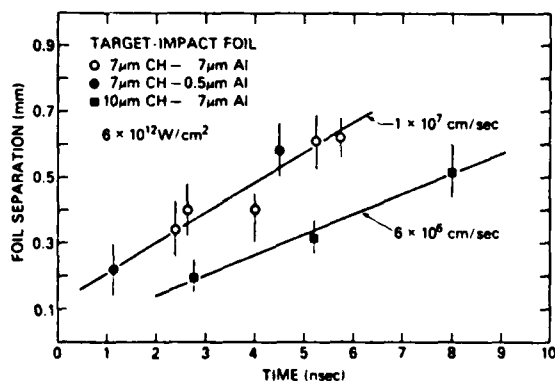

FIG. 6. A graph of target-impact foil separation versus the time (with respect to an arbitrary origin) at which the impact foil reacts to its collision with the target. The slopes of lines drawn through points accumulated over many discharges give the dense target velocities. The laser pulse duration is 4-nsec FWHM.
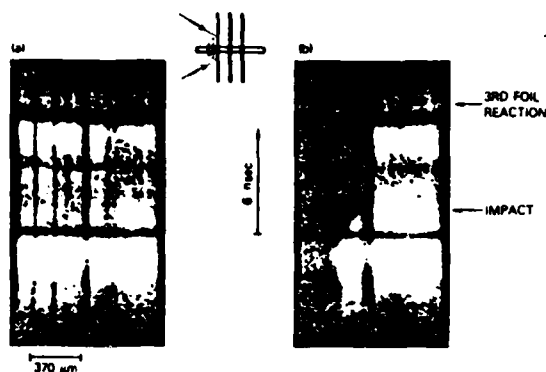
FIG. 7. Triple-foil experiment: A third foil diagnoses the second foil. The laser accelerated target is 3-μm thick C and the two impact foils are 7-μm thick C, respectively.

FIG. 9. Density profiles of a thin and a thick target accelerated to high velocities. The laser is incident from the right; ρ_{ecrit} is the critical electron density. The simulation conditions are: (a) 1.6×10^{13} W/cm² absorbed, 2.6-nsec pulse duration, 6.5-μm thick CH target and (b) 1×10^{13} W/cm² absorbed, 4-nsec pulse duration and 20-μm thick CH target.

pressure history in the collision cannot be gotten from measurements using optical probe light (Fig. 5). This is demonstrated in Fig. 7 which shows that the leading edge of the impact foil shadow exerts insufficient pressure to cause a third foil to react.

Backlighting the double foils with x rays provides a way to directly measure the motion of the dense portion of both foils. An x-ray shadowgraph of a double foil photographed using a ½-nsec duration Al x-ray flash (K shell emission, mostly at 1.6 keV; ½ mil Be filter on camera) as a backlighting source, is shown in Fig. 8.[4] This figure is the x-ray shadowgraph of a 7-μm thick carbon target irradiated with 3.5×10^{12} W/cm², and moving at $3-4 \times 10^6$ cm/sec before its collision with a 7-μm thick carbon impact foil. The shadows visible in Fig. 8 are the unaccelerated foil, the accelerated target, and the impact foil. Bright regions are due to the x-ray flash and x-ray emission from the plasma corona on the target's front surface. We estimate, from x-ray absorption data in cold carbon and the observed path lengths, that the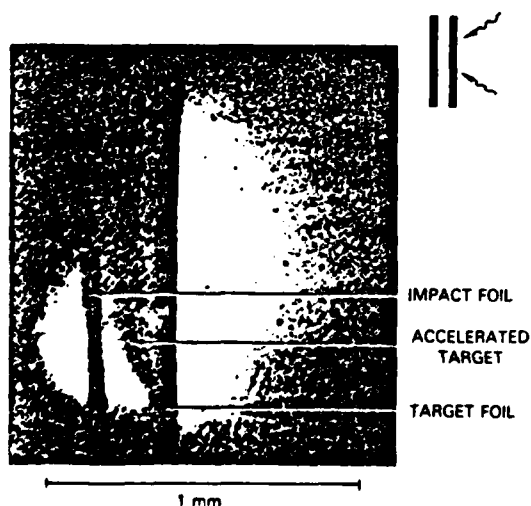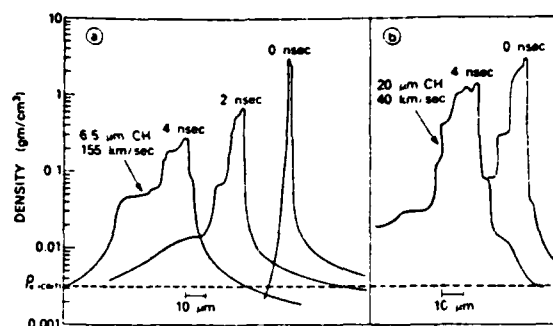 shadows are caused by material that is at least 3% of solid density. Thus, the figure shows that the dense, accelerated target traversed most of the distance to the impact foil—a distance 30 times its thickness—without noticeable breakup. It is evident too that the impact foil does not react appreciably before it is hit by the high density part of the target. These observations support our interpretation of results from the double-foil method. Also, velocities obtained by x-ray backlighting agree with those obtained by the double-foil method: velocities obtained with the two methods, on different shots, are the same to within 35%.

It is also interesting to note that the accelerated target is not "cut out" from the rest of the target foil, but is connected to it with a near solid density bridge. The gap between the accelerated target and the target foil is thus effectively closed so that front surface plasma cannot flow to the impact foil and disturb our measurements. This bridge, in addition, prevents front surface plasma from heating the rear of the target, and thereby spuriously increasing the rear surface temperatures measured in Ref. 10 and later in this paper.

We have computed target velocities and density profiles using a one-dimensional fluid code that has been described elsewhere.[14] This code utilizes a sliding zone Eulerian grid with flux corrected transport (FCT). The physics included in the code are: a single temperature fluid, classical transport physics with Spitzer heat conduction, and the same temporal irradiance history as the experiment. Absorption in our $< 10^{14}$ W/cm² long pulse regime is assumed to be by inverse bremsstrahlung in the underdense region with any remaining energy dumped smoothly into two zones surrounding the critical surface. The only target preheating considered is by shocks. Examples of computed density profiles for thin, fast targets and thick, slow targets are shown in Fig. 9. Both the thick and thin target in the figure are compressed during the acceleration phase. Afterwards they expand somewhat and develop a low density foot that precedes the dense target. Such a low density foot in front of the dense target material is inferred in the experiment. The expansion rate of the dense target is much smaller than its directed velocity. However, the expansion rate and the length of the low density foot are probably underestimated in the calculation because preheat mechanisms other than shock heating are not included.

IMPACT FOIL

ACCELERATED TARGET

TARGET FOIL

1 mm

FIG. 8. The x-ray shadowgraph of a double foil before the target-impact foil collision. The x-ray flash is ½ nsec long and occurs 5 nsec after the peak of the laser pulse. Pinhole smearing and time smearing are about 20 μm each.

In addition to measuring target velocity magnitude, measuring the velocity profile across the target is also important. This is because nonuniformly accelerated pellet shells will not achieve high compression ratios and will thereby degrade the pellet gain. Nonuniform target velocities could arise from any number of sources such as hydrodynamic instabilities, nonuniform targets or nonuniform irradiation. We now address the third issue, namely: Are target velocity profiles and irradiance profiles directly related, or will a mechanism such as thermal conduction in the ablation plasma smooth irradiance nonuniformities? Answers to this question will influence the choice and design of lasers for direct illumination pellet implosions.

To measure target velocity profiles we utilize the visible light which is emitted from the rear surface of the impact foil during its collision with the target. The time of this emission corresponds closely to the time of the dense target-impact foil collision as determined from double-foil streak shadowgraphy (Fig. 10), making the emission a good time marker from which the target velocity may be derived. Now, if a nonuniformly accelerated target collides with an impact foil the regions of the impact foil struck by fast portions of the target will emit first. Conversely, the regions of the impact foil struck by slower portions of the target will emit later. Consequently, target velocity profiles may be determined from differences in emission time across the impact foil's surface.

The relationship between a dense target-impact foil collision and the visible emission from the impact foil's rear surface is graphically illustrated by Figs. 11(a) and 11(b). Figure 11(a) shows the x-ray shadowgraph of an impact foil after it has collided with a nonuniformy accelerated target. Nonuniform acceleration was purposefully induced by a laser pulse whose spatial intensity profile was distorted with a rectangular mask that blocked a portion of the laser beam thus casting a low-intensity shadow across the center of the focal spot. Under these conditions, the directly irradiated
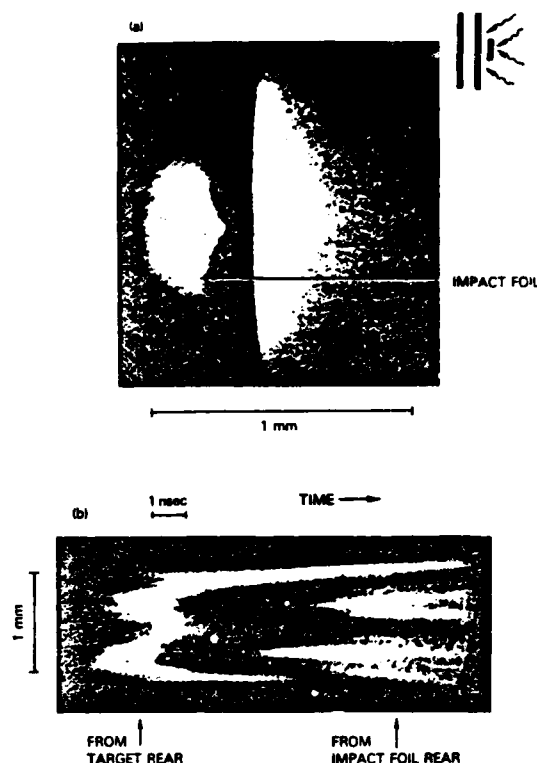
FIG. 11. Two views of the collision between a nonuniformly accelerated target and an impact foil: (a) An x-ray shadowgraph taken after the target and the impact foil collided. The x-ray flash and pinhole smearing conditions are the same as in Fig. 8. (b) Visible emission from the rear of a nonuniformly accelerated target and from the rear of an impact foil struck by that target.

regions of the target accelerate ahead of the shadowed region and subsequently impress their shape on the impact foil. Streaked emission from the rear of an impact foil struck by a nonuniformly accelerated target is shown in Fig. 11(b). In this figure, we used a double-foil configuration in which the impact foil was transparent so that emission from the accelerating target rear and the impact foil rear could be recorded on the same discharge. The temporal history of this emission is as follows: Before the collision, and while the impact foil is transparent, only the emission from the target is seen. This emission emanates initially only from those target regions that are directly irradiated—as seen on the left of Fig. 11(b). As time goes on, however, the emitting region spreads in space causing both the directly irradiated and shaded target regions to appear luminous. Such spread may be caused in part by the expansion of the low density, luminous plasma that precedes the dense part of the target and, perhaps, in part by shock heating of the shaded region of the target. Whatever the mechanism, when the low density portion of the target reaches the impact foil, the foil's optical opacity is increased so that the target emission is no longer visible, and the middle of the streak record appears dark.[15] Afterwards, when the high density portion of the target finally collides with the impact foil, the impact foil's rear begins to emit from two well defined lobes. These luminous lobes corre-
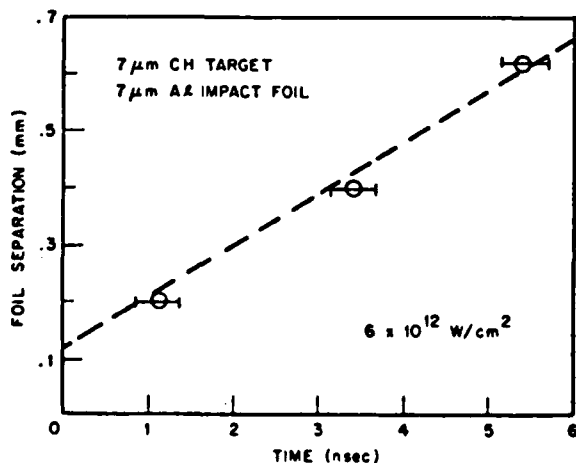

FIG. 10 Foil separation versus collision time determined in two ways: (1) from double-foil streak shadowgraphy (dashed line), and (2) from light emission at the rear of the impact foil (○). Light emission is measured at 10% of the full scale reading of the spectrograph photomultiplier.

spond to the two impact foil bulges in Fig. 11(a). Thus, we have further evidence that emission from the impact-foil rear is sensitive to velocity nonuniformities in the dense portion of the target. Target structure which may be obscured from direct view by a low density plasma is unmasked by the double-foil method.

The speed of the light emission front propagating through aluminum impact foils has been directly measured by using impact foils with a thickness step on their rear surface and noting the time difference between emission from the two sides of the step. We found that the emission front was supersonic (10^6 cm/sec) when the foils collided during the laser pulse, i.e., when the target was still accelerating; but it was close to sonic if the collision occurred after the acceleration. The supersonic velocities are consistent with shock heating causing the rear-surface light emission. The lower, sonic velocities can be explained by assuming that decompression of the target after acceleration cushions the collision impact preventing the formation of a strong shock.

Figure 12(a) shows the velocity profiles of dense targets accelerated to 160 km/sec—a velocity above the lower limit thought to be required for laser fusion.[1] The rear-surface brightness temperature of these targets is measured to be below 10 eV throughout the acceleration [Fig. 12(b)]. Their

speed is consistent with the predictions of our hydrodynamic code. The code, for example, predicts the measured target velocities at an absorbed irradiance of 1.6×10^{13} W/cm^2 (Fig. 9a), while the experiment utilizes an incident irradiance of 2.9×10^{13} W/cm^2 which—with 80% absorption[8]—is equivalent to an absorbed irradiance of 2.3×10^{13} W/cm^2. Focal-spot-edge effects[2,5,8] at the relatively high irradiance and small laser spot size of this measurement (600 μm diameter) probably reduce the effective irradiance below 2.3×10^{13} W/cm^2 and bring it closer to the predicted value.

The fast moving targets in Fig. 12(a) exhibit a velocity nonuniformity $(V_{max} - V_{min})/V_{min}$ of only 15%, even though the peak-to-valley nonuniformities of our laser beam are about 2 to 1 (Fig. 1). This smoothing of laser nonuniformities may be due to the so-called "cloudy day effect"[16] in which laser radiation absorbed near the critical surface is thermally smoothed by the time it is transported to the ablation surface, where most of the pressure is applied to the target. We did, in fact, make measurements on the ablation plasma which qualitatively support such a mechanism. These measurements will be shown at the end of Sec. IV.

We have also conducted quantitative studies of the relationship between laser nonuniformities and target velocity nonuniformities.[3] To simplify the analysis we used slowly
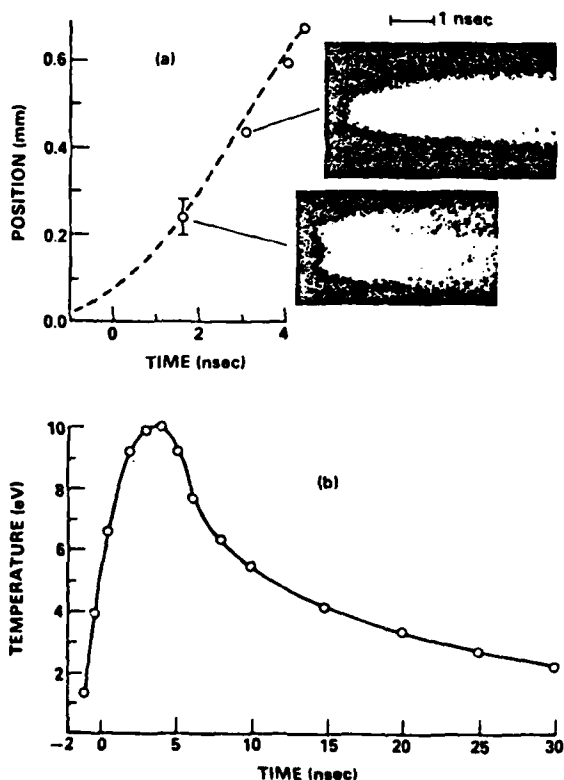

FIG. 12. Velocity profiles and positions (a), and rear surface temperatures (b) of targets accelerated to 160 km/sec. The dashed line is a theoretical fit to the data (·) based on the ablation pressure and mass ablation rate scaling laws described in Sec. IV. The peak of the laser pulse in (b) is at 0 nsec. The targets are 6.5 μm thick CH, the laser pulse length is 2.6 nsec, the laser-spot diameter is 600 μm, and the incident irradiance is 2.9×10^{13} W/cm^2. Velocity profiles are measured with the double-foil method.
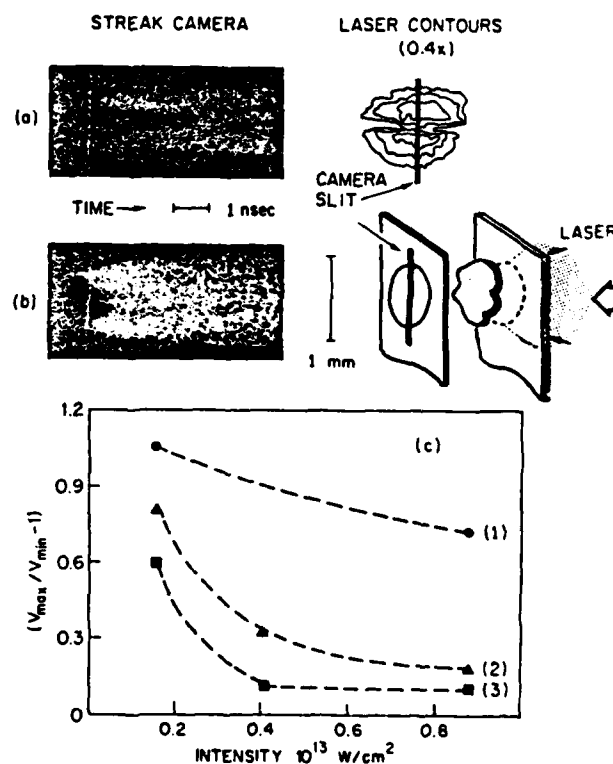
FIG. 13. Velocity nonuniformities decrease with irradiance: (a), (b) Streaked emission from the rear surface of an impact foil struck by a target irradiated with a structured laser profile. The mean irradiances are (a) 4×10^{12} W/cm^2 and (b) 9×10^{12} W/cm^2. Spatial resolution is 20 μm. (c) Target velocity nonuniformities graphed as functions of average irradiance for different dips in the incident beam: (1) $I_{max}/I_{min} \simeq 10$, 220-$\mu$m FWHM dip; (2) $I_{max}/I_{min} \simeq 6$, 140-μm FWHM dip; (3) $I_{max}/I_{min} \simeq 2$, 140-μm FWHM dip. Case (2) has the laser focal-spot contours shown in the figure. Finite risetime of the impact foil emission limits velocity nonuniformity resolution to approximately 5%.

moving foils accelerated to no more than 50 km/sec. Under these conditions, the fraction of mass ablated from these foils is small so the velocity nonuniformities are expected to scale almost linearly with irradiance nonuniformities in the absence of smoothing, i.e., $(V_{max}/V_{min}) \propto \mathscr{P}_{\perp_{max}}/\mathscr{P}_{\perp_{min}} \propto (I_{max}/I_{min})^{0.8}$, where the scaling of pressure with irradiance derived in Sec. IV is used. Velocity nonuniformities below this scaling indicate the presence of a smoothing mechanism.

Some velocity nonuniformity results are shown in Fig. 13. Figures 13(a) and (b) show the emission from impact foils struck by targets irradiated with the spatially structured laser beam shown in the inset at two different average irradiances. Note how the velocity nonuniformities are markedly reduced at the higher irradiance. In Fig. 13(c) velocity nonuniformities for several laser irradiance profiles are plotted. In all cases there is an increase of irradiance profile smoothing with higher average irradiance. At about 10^{13} W/cm^2, 140-μm FWHM dips in intensity are almost completely smoothed out but the 200-μm FWHM dips in intensity are imprinted on the target. Calculations[14] indicate that in this irradiance regime the ablation to critical surface separation increases with irradiance as $I^{0.7}$ and is about 100 μm at 10^{13} W/cm^2. Therefore, these results are qualitatively consistent with a thermal conduction mechanism which smoothes laser nonuniformities when the ablation surface to critical surface distance is comparable to the nonuniformity scalelength. It remains to be seen whether larger wavelength perturbations at somewhat higher irradiances are similarly smoothed out. If they are, then the 1%–3% ablation pressure uniformities required for a high-gain pellet[17] may be achievable with realistic laser systems.

IV. ABLATION PLASMA STUDIES

In this section we present measurements of ablation plasma properties relevant for the target velocity measurements described above. Also, using a tracer technique to spatially resolve the ablation plasma flow, we provide evidence
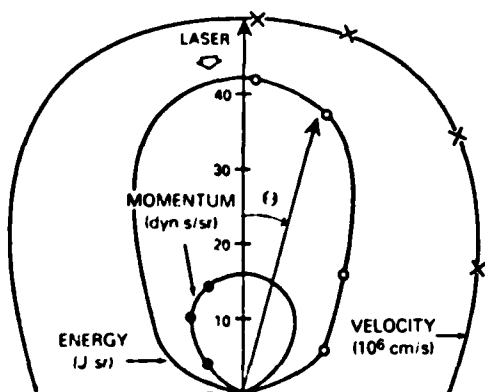

FIG. 14. Distribution of blowoff velocity, energy, and momentum measured with time-of-flight ion collectors, plasma calorimeters, and ballistic pendula respectively. The target is a 1.2-mm diameter CH disk irradiated at 3×10^{13} W/cm^2.

that the observed smoothing of target velocity profiles is indeed caused by smoothing in the ablating plasma.

Both foils and disk targets are chosen for these studies. Each type of target has its own advantage: Wide foils, for example, do not permit ablation plasma to flow around the foil edge and interfere with rear surface measurements. Disk targets, on the other hand, can be irradiated relatively uniformly by using a focal-spot diameter larger than the disk diameter, and, since the laser-target interaction area A is fixed by the finite geometry, average irradiances as well as ablation pressures ($\propto$ momentum/area) and mass ablation rates ($\propto$ mass/area) may be reliably calculated. Also, any energy that escapes the interaction area is easily detected and its effect on the results easily estimated. A small amount of ablation plasma energy has indeed been measured at the rear of disk targets with plasma calorimeters, but its effect is minimal in our experiments. For example, for 300-μm and 600-μm diameter disks less than 20% of the total absorbed (plasma and target) energy is detected at the rear of the disk, while for 1000-μm and 1200-μm diameter disks less than 5% of the absorbed energy flows rearward. At the irradiances employed in these experiments, this excess energy is probably due to the flow of hot thermal plasma around the disk edges. Very energetic suprathermal electrons observed in CO_2 laser experiments[18] and at higher irradiance Nd laser experiments[19] are not the dominant mechanism here, as evidenced by the low level of x-ray emission observed above 20 keV.[20]

When a ballistic pendulum measurement[2] is used, as it is here, special care must be taken that events beyond the focal-spot periphery do not influence the experimental results. Such events, if significant, could not only complicate interpretation of the results but could make them irrelevant to laser fusion, since a fusion pellet surface has no edges. For many diagnostics the finiteness of the laser spot is not a major concern since the phenomenon investigated requires high energies that exist only within the focal spot or the diagnostic has time or space resolution. But a pendulum is time and space integrating, and a small amount of energy can easily heat large amounts of mass to produce a large momentum. Small amounts of such extraneous energy may be provided by thermal conduction through the focal-spot periphery, by plasma flow along the target surface, or by radiation from the plasma plume. The situation is further complicated since these heating mechanisms may vary with laser-spot size, energy, or irradiance. We have observed, in fact, that under some circumstances the momentum of material from beyond the focal-spot region is seven times as large as the momentum from within the focal-spot region.[2] For these reasons we ordinarily use only disk targets with the pendulum measurement.

Angular distributions of the ablation plasma energy $E(\theta)$, momentum $p(\theta)$, and velocity $\bar{u}(\theta)$ for an isolated disk target are shown in Fig. 14; $\bar{u}$ is a mean velocity unfolded from ion-collector traces.[2] Angular distributions from various disk (0.3 to 1.2 mm diameter) and wide foil targets have similar shapes. All detectors are in the plane of incidence and cylindrical symmetry about the target-normal is assumed. From such angular distributions we determine the ablation pressure $\mathscr{P}_\perp = P_\perp / \tau A$, mass ablation rate $\dot{m} = m_a / A\tau$, and

ablation velocity $u_\perp = P_\perp/m_a$ where m_a is the ablated mass, τ is the FWHM pulse duration, and $P_\perp$ is the normal component of the total momentum P obtained by integrating $p(\theta)$ over all solid angles. The letter A in the definition of $\mathscr{P}_\perp$ and $\dot{m}$ represents either the surface area of a disk target or, for a foil target, the focal-spot area containing 90% of the laser energy. In the latter case, the focal-spot diameters are chosen to be large ($\simeq 1$ mm) so that extraneous focal-spot-edge effects are minimized.

Scaling of ablation pressure with absorbed irradiance $\mathscr{P}_\perp \propto I_a^{0.8}$ is shown in Fig. 15(a).[2,5] Momentum (pressure) in the case of disk targets is determined in two independent ways: first directly, using the pendulum array and second, indirectly, using the energy from plasma calorimeters and velocity data from time-of-flight detectors; wide foil results use the latter method only. Agreement between all these independent measurements increases our confidence in the results. The scalings in the absorbed irradiance of the ablation velocity $u_\perp \propto I_a^{0.2}$, and the mass ablation rate $\dot{m} \propto I_a^{0.6}$ are shown in Fig. 15(b).

The momenta of the ablation plasma [Fig. 15(a)] and momenta of the accelerated targets, inferred from the velocity measurements in Sec. III, balance. For example, the target momentum for the cases in Fig. 6 is about 0.7 of the ablation plasma momentum. Similar agreement was obtained on a few irradiations where the target velocities and the ablation plasma momenta were simultaneously measured.
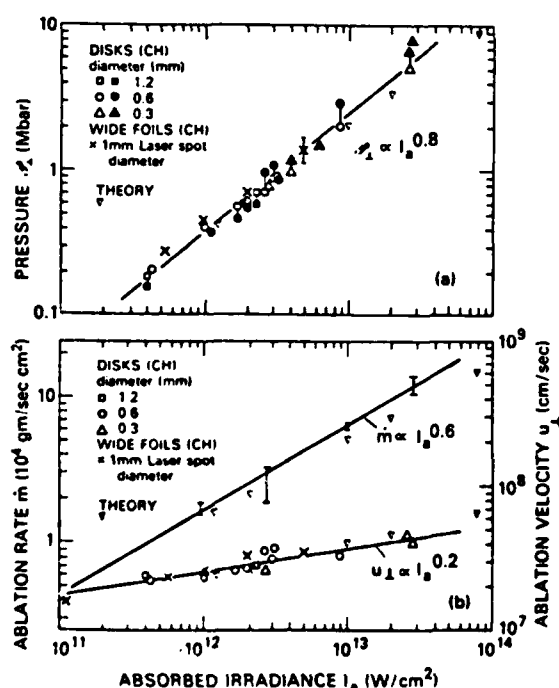
Figure 15 also shows that the measured ablation parameters agree well with like quantities computed with our hydrodynamic code. In this code, the time averaged ablation parameters are calculated by computing the total mass and momentum moving away from the target late enough in the run ($\simeq 14$ nsec) so that little further mass or momentum is added to the plasma. This is done so that the computed quantities are nearly the same as the quantities measured experimentally. The calculated scalings are: $\mathscr{P}_\perp \propto I_a^{0.75}$, $u_\perp \propto I_a^{0.24}$, and $\dot{m} \propto I_a^{0.55}$.

Table I compares our ablation results to other published theories. All of these theories assume a steady or quasisteady ablation plasma flow which is described by conservation of mass, energy, and momentum: but they differ in other details. Some theories (Kidder, Caruso, and Gratton),[21,22] which are in planar geometry, neglect details of the absorption and energy transport to the ablation layer. They also assume that all of the absorbed energy supports the expansion of the ablation plasma, and that the underdense plasma expands with sonic velocity. Some theories assume sonic flow at the critical surface with (Manheimer et al.)[23] and without (Jarboe et al.)[24] thermal conduction, and some (Ahlborn et al.)[25] eliminate the sonic flow hypothesis altogether. Divergent plasma flow from planar targets was included by Puell[26] who treated plasma hydrodynamics in planar geometry using a model similar to Refs. 21 and 22, but considered plasma expansion when calculating absorption of laser light and the temperature at the sonic radius. Scalings of ablation parameters with irradiance in spherical geometry were determined by Nemchinov[27] who neglected thermal transport. Scaling of the mass ablation rate was determined by Gitomer et al.[28] who included thermal transport but assumed that the sonic radius does not vary with irradiance. The effects of inhibited thermal conductivity in spherical geometry (at irradiances higher than ours) upon ablation was considered by Max et al.[29]

Our results agree with all the theories except that of Max et al. which assumes strongly inhibited thermal trans-

FIG 15 Ablation pressure (a), mass ablation rate and ablation velocity (b) versus absorbed laser irradiance for disks and wide foil targets. The data ●, ■, ▲ are inferred using momenta measured with ballistic pendula. The data ○, □, △ are obtained using calorimeter and time-of-flight measurements. The laser pulse duration is 4-nsec FWHM.

TABLE I. Comparison of experiment to theoretical scaling laws. Table entries are the exponents b of $y \propto I_a^b$ where y is an ablation parameter, and I_a the absorbed irradiance. The theories may be found in Refs. 21–29.

Theory	$\mathscr{P}_\perp$	$u_\perp$	$\dot{m}$
Kidder	0.75	0.25	0.50
Caruso	0.75	0.25	0.50
Ahlborn	0.78[a]	0.22[a]	0.56[a]
Jarboe	0.66[b]	0.33[b]	0.33[b]
Manheimer	0.66	0.33	0.33
Puell	0.78	0.22	0.56
Nemchinov	0.78	0.22	0.56
Gitomer			0.56
Max	0.57	0.09	0.48
Experiment	0.8	0.2	0.6

[a] $\eta^{\pm 1/9}$, $\eta^{2/9}$ in Ahlborn's expressions have been treated as constants. η is the absorption fraction.
[b] Jarboe et al. explicitly derive a relation for $u_\perp$ only. To get the other two quantities we used the relations $\mathscr{P}_\perp \propto n_c u_\perp^2$ and $\dot{m} \propto n_c u_\perp$ implied by his theory; n_c is the critical density.
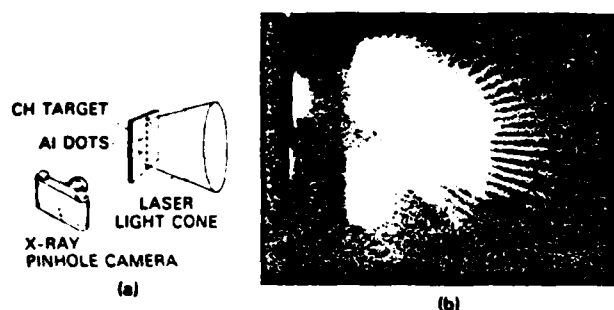
FIG. 16. Experimental setup (a) to spatially resolve plasma flow (b) near the target surface. The five images are from five pinholes in the camera.
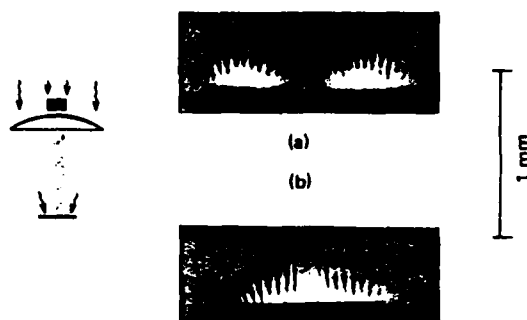

FIG. 17. Ablation plasma flow from thick CH targets irradiated by a structured laser profile. The irradiance conditions are: (a) Mean irradiance of 3×10^{12} W/cm^2, $I_{max}/I_{min} \simeq 8$, 220-μm FWHM dip. (b) Mean irradiance of 6×10^{12} W/cm^2, $I_{max}/I_{min} \simeq 6$ 140-μm FWHM dip. Mean irradiance is changed here by reducing the laser spot diameter.

port, and that of Jarboe *et al.* and Manheimer *et al.* who fix the sonic flow point at critical density and do not let the exhaust density vary with irradiance.

Until now, we have discussed measurements of ablation plasma parameters far from the target surface, i.e., after the parameters reached their asymptotic values. It is, of course, desirable to also know the hydrodynamic development of these quantities as the plasma flows away from the target. In particular, if the results of our experiments are to be extrapolated to spherical geometry, then the difference between plasma flow from our planar targets and spherical pellets must be taken into account. Toward this end, we have developed a tracer technique that lets us spatially resolve the plasma flow from a target surface.[6] Using this method we can also track plasma flow from nonuniformly irradiated targets so that smoothing effects may be studied.

The arrangement for this experiment is shown in Fig. 16(a). An x-ray pinhole camera is placed to view edge-on a polystyrene (CH) target with a row of small Al dots (0.5 μm thick, 25-μm diameter, spaced 50 μm apart) imbedded in it. When the target is irradiated both the aluminum and the polystyrene ablate from its surface. However, since the aluminum is a much stronger emitter of x rays in the spectral band of the pinhole camera (> 1 keV) than polystyrene, the presence of aluminum ions in the plasma flow is identified by the presence of strong x-ray emission. We assume that the perturbation of the flow pattern by the aluminum tracer is small. This assumption is reasonable since for a given electron density n_e in the ablation plasma the fully ionized ion mass density ρ_i for Al and CH targets differ only by 12% $(\rho_i = n_e M/Q$, where Q and M are the ion charge and mass, respectively). Also, the speed of Al and CH target ions, measured with time-of-flight ion collectors, is the same.

Figure 16(b) is a photograph of the plasma flow from a target irradiated by a nonperturbed laser beam. The five images in the figure result from a five pinhole array (5–55 μm) through which the target was photographed. It is evident from Fig. 16(b) that the ablation plasma flow is reminiscent of a steady state fluid flow from a circular orifice. Note that the plasma flow is planar near the target surface, and that distinct regions of the target map into distinct solid angles.

In Sec. III it was shown that the velocity profiles of accelerated targets were, under certain conditions, smoother

than expected given the irradiance nonuniformity. We surmised that these smoother velocity profiles resulted from ablation pressures which were themselves smoothed by lateral heat flow in the ablation plasma. Such smoothing in the ablation plasma is also observed using the tracer technique. Figure 17(a) shows spatially resolved plasma flow from a thick CH target irradiated by a laser beam distorted as in Fig. 11. The average irradiance is 3×10^{12} W/cm^2, the nonuniformity depth I_{max}/I_{min} is about 8, and the nonuniformity width is 220-μm FWHM. Under these conditions no significant ablation smoothing is expected and none is seen here. However, smoothing is expected and seen in Fig. 17(b) where the average irradiance is raised by a factor of 2, the nonuniformity depth is reduced to about 6, and the nonuniformity width is reduced to 140-μm FWHM. Under these conditions, lateral energy flow from the directly irradiated regions into the central shaded region ablates the target surface there and causes distinct streamlines of plasma to emanate from the shaded region. These streamlines are compressed only slightly by the surrounding plasma which indicates that the pressures in the shaded and unshaded regions are comparable, and qualitatively confirms the previous results. Quantitative measurements of plasma conditions in the shaded region are the subject of a future study.

V. CONCLUSION

In this work we used ablatively accelerated planar targets to model the dynamics of large, hollow, ablatively driven fusion pellets. The velocities and velocity profiles of the dense regions of highly accelerated planar targets were measured. Despite two-to-one laser nonuniformities, we did accelerate thin, relatively uniform, and cool targets to 160 km/ sec. We have also measured an increase in irradiance profile smoothing with increasing laser irradiance. This is encouraging for laser fusion. However, the behavior of targets with multimillimeter density and nonuniformity scalelengths that are typical of fusion scenarios is not yet known.

We also made simultaneous measurements of the ablation pressure $\mathscr{P}_a$, ablation rate $\dot{m}$, and ablation velocity u_a.

In these measurements we utilized large laser spots and disk targets so that our results are not sensitive to focal-spot-edge effects. We found that $\mathscr{P}_\perp \propto I_a^{0.8}$, $\dot{m} \propto I_a^{0.6}$, and $u_\perp \propto I_a^{0.2}$ where I_a is the absorbed irradiance. Also, the ablation plasma momenta and the momenta of ablatively accelerated targets balance. These results agree with a planar geometry fluid code that uses classical transport physics.

ACKNOWLEDGMENTS

[1]J. H. Nuckolls, R. O. Bangerter, J. D. Lindl, W. C. Mead, and Y. L. Pan, European Conference on Laser Interaction with Matter, Oxford, England, September 1977.

[2]J. Grun, Naval Research Laboratory Memorandum Report No. 4491 (1981).

[3]S. P. Obenschain, J. Grun, B. H. Ripin, and E. A. McLean, Phys. Rev. Lett. 46, 1402 (1981).

[4]R. R. Whitlock, S. P. Obenschain, J. Grun, J. McMahon, and B. H. Ripin, in Proceedings of the Topical Conference on Symmetry Aspects of Inertial Fusion Implosions, 27–28 May 1981, Naval Research Laboratory, Washington, D. C.

[5]J. Grun, R. Decoste, B. H. Ripin, and J. H. Gardner, Appl. Phys. Lett. 39, 545 (1981).

[6]M. J. Herbst and J. Grun, Phys. Fluids 24, 1917 (1981).

[7]J. M. McMahon, R. P. Burns, T. H. DeRieux, R. A. Hunsicker, and R. H. Lehmberg, IEEE J. Quantum Electron. QE-17, 1629 (1981).

[8]R. Decoste, S. E. Bodner, B. H. Ripin, E. A. McLean, S. P. Obenschain, and C. M. Armstrong, Phys. Rev. Lett. 42, 1673 (1979); B. H. Ripin, R. Decoste, S. P. Obenschain, S. E. Bodner, E. A. McLean, F. C. Young, R. R. Whitlock, C. M. Armstrong, J. Grun, J. A. Stamper, S. H. Gold, D. J. Nagel, R. H. Lehmberg, and J. M. McMahon, Phys. Fluids 23, 1012 (1980); 24, 990 (E) (1981).

[9]B. H. Ripin, NRL Memorandum Report No. 3315, edited by S. E. Bodner (August 1976), Chap. II.

[10]E. A. McLean, S. H. Gold, J. A. Stamper, R. R. Whitlock, H. R. Griem, S. P. Obenschain, B. H. Ripin, S. E. Bodner, M. J. Herbst, S. J. Gitomer, and M. K. Matzen, Phys. Rev. Lett. 45, 1246 (1980).

[11]B. H. Ripin, S. E. Bodner, S. H. Gold, H. R. Griem, J. Grun, M. J. Herbst, R. H. Lehmberg, E. A. McLean, J. M. McMahon, S. P. Obenschain, J. A. Stamper, R. R. Whitlock, and F. C. Young, presented at the CLEOS/ICF 80 Topical Meeting on Inertial Confinement Fusion, 27 February 1980, San Diego, CA.

[12]R. J. Trainor, H. C. Graboske, K. S. Long, and J. W. Shaner, Lawrence Livermore National Laboratory Memorandum Report No. UCRL-52562 (1978); R. J. Harrach and A. Szoke, Lawrence Livermore National Laboratory Report No. UCRL-86798 (1981).

[13]Ya. B. Zel'dovich and Y. P. Raizer, Physics of Shock Waves and High-Temperature Hydrodynamic Phenomena (Academic, New York, 1966).

[14]J. H. Gardner and S. E. Bodner, Phys. Rev. Lett. 47, 1137 (1981).

[15]One of the authors has also observed an increase of opacity in an initially transparent single target irradiated by a laser. S. Gold and E. A. McLean, J. Appl. Phys. 53, 784 (1982).

[16]J. H. Nuckolls, L. Wood, A. Thiessen, and G. Zimmerman, Nature 239, 193 (1972).

[17]S. E. Bodner, J. Fusion Energy 1 (3), 221 (1981).

[18]N. A. Ebrahim, C. Joshi, D. M. Villeneuve, N. H. Burnett, and M. C. Richardson, Phys. Rev. Lett. 43, 1996 (1979).

[19]C. M. Armstrong, B. H. Ripin, F. C. Young, R. Decoste, R. R. Whitlock, and S. E. Bodner, J. Appl. Phys. 50, 5233 (1979).

[20]M. J. Herbst, R. R. Whitlock, and F. C. Young, Phys. Rev. Lett. 47, 91 (1981); 47, 1568 (E) (1981).

[21]R. E. Kidder, Nucl. Fusion 8, 3 (1968).

[22]A. Caruso and R. Gratton, Plasma Phys. 10, 867 (1968).

[23]W. M. Manheimer, D. G. Colombant, and J. H. Gardner, Phys. Fluids 25, 1644 (1982).

[24]T. R. Jarboe, W. B. Kunkel, and A. F. Lietzke, Phys. Fluids 19, 1501 (1976).

[25]B. Ahlborn and M. H. Key, U. of British Columbia Lab. Report No. 73 (1980).

[26]H. Puell, Z. Naturforsch 25a, 1807 (1970).

[27]I. V. Nemchinov, J. Appl. Math. Mech. 31, 320 (1967).

[28]S. J. Gitomer, R. L. Morse, and B. S. Newberger, Phys. Fluids 20, 234 (1977); Scaling of the mass ablation rate may be determined from this paper if r_s (the sonic radius) is assumed constant—S. J. Gitomer (private communication).

[29]C. E. Max, C. F. McKee, and W. C. Mead, Phys. Rev. Lett. 45, 28 (1980).

APPENDIX B

Characteristics of ablation plasma from planar, laser-driven targets

J. Grun, [a] R. Decoste, [b] B. H. Ripin, and J. Gardner

Naval Research Laboratory, Washington D.C. 20375

The momentum, energy, and velocity characteristics of plasma ablating from planar targets irradiated by long Nd-laser pulses (4 ns, $< 10^{14}$ W/cm^2) are measured and the dependence of ablation parameters upon absorbed irradiance is determined. Large laser spots are used in these experiments so that the results are not sensitive to boundary effects.

PACS numbers: 52.50.Jm, 52.70.Nc, 52.30. + r

Considerable effort is underway to study the feasibility of imploding moderate aspect ratio, high-gain fusion pellets. In this concept, long duration laser or ion beam pulses ablate pellet surface material whose rapid evaporation creates a pressure that implodes the pellet walls. This pressure, and the speed of the ablated material or the mass ablation rate, help determine the velocity of the imploding walls, their rate of acceleration, and the hydrodynamic efficiency of the im-

plosion. Accurate measurements of these ablation parameters are, therefore, basic to the calibration of computational codes used to design fusion pellets, and are basic to the search for an irradiance regime consistent with a stable and efficient implosion.[1] Measurements of ablation pressures on planar targets using small-diameter laser spots and theoretical estimates of the effective laser-target interaction area have been previously reported.[2] In this letter we present simultaneous measurements of the ablation pressure, the mass ablation depth ($\propto$ mass ablation rate), and the ablation velocity. We also use large-diameter laser spots and uniformly irradiated disks, so that the results are not sensitive to focal-spot edge effects associated with energy flow through the focal-spot periphery. The laser-target interaction area is ex-

perimentally determined. We utilize redundant measurements and diagnostics to verify the validity and self-consistency of these results.

Configuration of the experiment is similar to one previously described.[3] Polystyrene (CH) targets are irradiated by a 1.05-μm wavelength, 4-ns FWHM duration laser pulse focused through an $f/6$ aspheric lens to an average irradiance $< 10^{14}$ W/cm^2. This pulse length is long enough so that stationary ablation physics dominate the laser plasma interaction.[4] Ablation pressure $\mathcal{P}_\perp \equiv P_\perp/\tau A$, mass ablation depth $d \equiv m_a/\rho A$, and ablation velocity $u_\perp \equiv P_\perp/m_a$ are determined from angular distributions of the ablation plasma energy $E(\theta)$, momentum $P(\theta)$, and velocity $\bar{u}(\theta)$ measured with arrays of plasma calorimeters, ballistic pendula, and time-of-flight ion collectors arranged around the target. (In the long-pulse regime ion collector traces are narrow and single peaked, making them ideal for time-of-flight measurements.) The quantities τ, A, and ρ are the pulse duration, the laser-target interaction area, and the target density, respectively; $P_\perp$ is the normal component of the total momentum P calculated by integrating the momentum distribution $P(\theta)$ or the distribution $2E/\bar{u}$ over all solid angles; m_a is the ablated mass. Although any two of the measured quantities would have been sufficient, we measured all three with independent diagnostics to verify the self-consistency and validity of our results.

The pendula employed here were tested and calibrated *in situ*.[5] In particular, we verified that pendulum recoil is caused by plasma impact only and that the pendulum array balances blowoff plasma and recoiling target momenta (to within 30%). We found, however, that material reflected or sputtered from a pendulum surface affects its absolute calibration. To determine the contribution of material reflection or sputter to the pendulum response and to thereby calibrate it absolutely, we built a double-pendulum device.[5] It consists of a primary pendulum directly facing the blowoff plasma and a secondary pendulum oriented to detect most of the material reflected or sputtered from the primary pendulum but shielded from the blowoff plasma. This *in-situ* calibration showed that the pendula in these experiments are 2.4 ± 0.6 more sensitive then their bench calibration would indicate.

To model the surface of large spherical pellets we utilize wide foil targets irradiated by large, 1-mm diam laser spots. The targets are sufficiently thick, so that their motion has little effect on the measurements. In some cases we also use uniformly irradiated disks.[6] These disks have two advantages over foil targets: first, the laser-target interaction area A that enters into calculations of absorbed irradiance, ablation pressure, and mass ablation depth is experimentally determined; second, any energy that escapes the interaction area is easily measured with plasma calorimeters so that its effect on the results can be estimated. A small loss of ablation plasma energy to the rear of disk targets does in fact occur, but this has minimal effect on the ablation parameters. For example, for 300- and 600-μm diam disks less than 20% of the total absorbed energy reached the rear disk surface, while for 1000- and 1200-μm diam disks less than 5% of the absorbed energy reached the rear disk surface. At our irra-

diances, the energy observed behind the target is probably due to the flow of hot thermal plasma around the disk edges. Very energetic suprathermal electrons[7] are not the dominant mechanism as evidenced by the low level x-ray emission observed above 20 keV.[8]

We note that the angular distributions of energy, velocity, and momentum from various diameter (0.3–1.2 mm) disks and wide foils irradiated by various diameter laser spots (0.3–2 mm) are similar. The momentum angular distribution, for example, is characterized by a half-cone angle $\cos^{-1}(P_\perp/P) = 40°$ for both the disk and wide foil cases.

Figure 1(a) shows the scaling of ablation pressure with absorbed irradiance to be $\mathcal{P}_\perp \propto I_a^{0.8}$ for disks and wide foil targets. Momentum in the case of disk targets is determined in two independent ways: first directly, using the pendulum array (dark markers) and second indirectly, using energy and velocity data (open markers); wide foil results (X) use the latter method only. Agreement between the two methods increases our confidence in the results. The scalings with absorbed irradiance of the ablation velocity $u_\perp \propto I_a^{0.2}$ and the mass ablation depth $d \propto I_a^{0.6}$ are shown in Fig. 1(b).

We also verified that these pressures, determined from asymptotic measurements, are the same (within 30%) as the ablation pressures deduced from measurements of target acceleration.[5]

The measured ablation parameters agree well with like quantities calculated using a one-dimensional (planar geometry), single-temperature hydrodynamic code (Fig. 1). This code is a sliding-zone Eulerian FCT code that requires no artificial viscosities, utilizes classical thermal transport
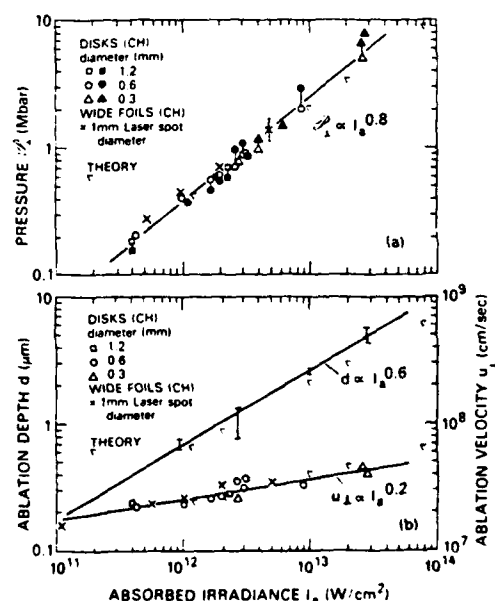
FIG. 1. (a) Ablation pressure vs absorbed laser irradiance for disks and wide foil targets. The data denoted by ■, ●, and ▲ are inferred using momenta measured with ballistic pendula. The data □, ○, and △ are obtained using calorimeter and time-of-flight measurements. The symbol ▽ denotes theoretical results. (b) Mass ablation depth d and normal ablation velocity $u_\perp$ vs absorbed irradiance I_a.

physics with no *ad-hoc* inhibition, and uses the same irradiance profile as the experiment. Absorption is by inverse bremsstrahlung in the underdense region with any remaining laser energy dumped smoothly into two zones surrounding the critical surface. To make a direct comparison with our data, we calculate the momentum and mass of all plasma moving toward the laser after these quantities reach their asymptotic values (14 ns after the laser pulse peak), and determine the temporally averaged ablation parameters $\mathscr{P}_\perp, d, u_\perp$ in the same manner as the experiment. (Peak calculated pressures which occur near the ablation surface are only 20% higher than the temporally averaged calculated pressures.) The good agreement between measured and calculated ablation parameters supports the view that basic conservation laws without any transport inhibition govern laser-target interaction physics in this irradiance and laser-pulse length regime.

Since the flow characteristics of ablation plasma from planar targets are set by its nozzlelike expansion from the target surface, plasmas from planar targets are not truly one dimensional. The good agreement between our experiment and a one-dimensional, planar geometry code may be explained, however, if the final nature of the ablation parameters is determined near the target surface, when the plasma flow is still planar. This picture is born out by the code which shows that most of the ablation plasma acceleration occurs between the ablation surface and a few times the distance from the ablation surface to the critical surface. This ablation surface to critical surface separation is about $100 \mu m$ at 1×10^{13} W/cm^2 (and less at lower irradiance), which is smaller than the laser-spot diameters or the disk diameters in the experiment. One-dimensional, spherical calculations with a large ratio of pellet radius (0.5 cm) to ablation to critical-surface distance gave irradiance scaling laws similar to those in planar geometry.

Studies using planar targets are subject to criticism that phenomena at the focal-spot periphery distort effects ascribed to the spot as a whole, so that the results do not extrapolate to spherical geometry pellets. Such phenomena may include energy leakage laterally across the focal-spot edge, which alters the irradiance distribution, and extraneous plasma from target areas outside the focal spot, which contributes to the measured results. To check for these effects we placed planar targets in the near field of the focusing lens and varied the spot size by aperturing the laser beam while monitoring the ablation velocity. Because of laser energy limitations, this experiment used an average irradiance of 1×10^{12} W/cm^2. But even at this low irradiance, the ablation velocity does vary with spot size (Fig. 2). The variation is small, however, if the laser spot diameter is sufficiently large ($\gtrsim 1$ mm). That is why experiments on foils reported here utilize large laser spots, even though this lowers the maximum irradiance achievable with our laser. It is also clear that controlling irradiance by changing the focal-spot size, as is often done, may lead to misleading results.

Two parameters which may change the effective spot size are the spatial profile of the incident irradiance and the lateral heat flow through the focal spot periphery. Since the number of ions at a particular velocity depends on absorbed
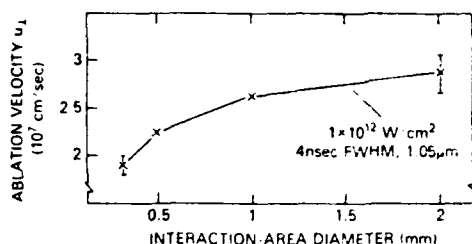

FIG. 2. Ablation velocity $u_\perp$ vs interaction-area diameter for wide foil targets. (Interaction area is defined as the area that contains 90% of the incident laser energy.)

irradiance, both these phenomena may contribute to the velocity variation in Fig. 2. Lateral heat flow especially could shift energy from a higher to a lower portion of the effective irradiance profile and increase the fraction of low velocity ions. Large spot sizes, with a relatively uniform and flat-topped illumination, have a smaller fraction of absorbed energy escaping through their edges and, therefore, behave somewhat independently of spot-size diameter.

In summary, we studied the ablation characteristics of plasma from planar, laser-driven targets. We found that ablation pressure, ablation velocity, and mass ablation depth scale as the 0.8, 0.2, and 0.6 power of the absorbed irradiance. Our results agree well with a one-dimensional hydrodynamic code that uses classical transport physics. Pressures of 10 Mbar exist at about 5×10^{13} W/cm^2. Hydrodynamically efficient compression of moderate aspect ratio pellets at this or slightly higher irradiance may thus be possible. We also found that due to edge-effects ablation velocity varies with laser-spot size, but the variations are small for sufficiently large spots.

[1] S. E. Bodner, J. Fusion Energy (to be published).
[2] B. Arad, S. Eliezer, Y. Gazit, H. M. Loebenstein, A. Zigler, H. Zmora, and S. Zweigenbaum, J. Appl. Phys. 50, 6817 (1979).
[3] B. H. Ripin, R. Decoste, S. P. Obenschain, S. E. Bodner, E. A. McLean, F. C. Young, R. R. Whitlock, C. M. Armstrong, J. Grun, J. A. Stamper, S. H. Gold, D. J. Nagel, R. H. Lehmberg, and J. M. McMahon. Phys. Fluids 23, 1012 (1980).
[4] M. K. Matzen and R. L. Morse, Phys. Fluids 22, 654 (1979).
[5] J. Grun, NRL Memo 4491, 1981 (unpublished).
[6] Intensity variations are ± 50%.
[7] N. A. Ebrahim, C. Joshi, D. M. Villeneuve, N. H. Burnett, and M. C. Richardson, Phys. Rev. Lett. 43, 1995 (1979).
[8] F. Young, private communication.

APPENDIX C

Flash x radiography of laser-accelerated targets

R. R. Whitlock, S. P. Obenschain, and J. Grun[a]
U. S. Naval Research Laboratory, Washington, D. C. 20375

Flash x radiography of ablatively accelerated planar foils has provided quantitative measurements and qualitative observations regarding several parameters of critical interest to direct illumination laser fusion. A 1.05-μ, 3.3-ns driver beam was focused onto carbon foils in a large (0.7–1-mm diameter) spot to reduce edge effects. From images produced by a backlighting x-ray flash, we have measured overall coupling efficiency, smoothing of laser nonuniformities, target velocity, and ablation pressure. The high velocity targets maintain a localized, high density (> 3% of solid). In contrast to other workers' recent measurement of pressure from x-ray imaging, our x-radiographic results, including pressure, are in general agreement with earlier NRL studies. Our results have also provided further insights into double foil interactions and planar target preheat measurements.

PACS numbers: 52.50.Jm, 52.25.Ps, 52.25.Fi

Direct illumination of spherical pellet shells by laser light in a moderate intensity regime somewhat above 10^{14} W/cm^2 may permit inertial confinement fusion to be achieved.[1] To that end, studies at NRL[2-11] have been directed to the physics of the laser-pellet interaction and of the efficient acceleration of pellet shells to fusionlike velocities.[1] To experimentally model spherical pellets early in the implosion phase, we use planar targets and large focal spots. These experiments have shown that the moderate intensity, direct illumination approach scales favorably in several areas of physics which have been identified as critical elements for laser fusion,[2] and that, therefore, further extension of these experimental studies to a regime closer to reactor conditions is warranted. In the present work, we used a flash x-ray probe to temporally resolve the position of the dense region of accelerated foils; from this, we quantitatively measured the ablation pressure, the target velocity, and the uniformity of target velocity. We also gained further insights into double foil interactions and target preheat measurements.

In earlier work,[7-9] visible probes, operating within limitations imposed by absorption and refraction, have been used to image ablatively accelerated targets. Flash x radiography[12,13] is applied here to planar target geometry to extend the probing photon energy by about 10^1 beyond the visible, thereby gaining simultaneous access to the front and rear, as well as the dense middle, of accelerated, high velocity targets. The experimental setup is diagrammed in Fig. 1. A pinhole camera using photographic film recorded the image of an x-ray source, an aluminum plasma produced by a 20-J, 0.6-ns laser pulse.[11] The object to be radiographed was placed between the source and the pinhole; source x rays absorbed by the object result in a shadow image of the object on the film. The objects radiographed were planar foil targets of pyrolytic graphite having areal densities in the range of 1.0–1.5 mg/cm^2. The backlighting x-ray flash was short enough that, for these targets, the travel distance during the flash (i.e., the velocity smearing) was comparable to the pinhole camera resolution (about $20\,\mu$ for a 10-μ pinhole, magnification 1.4), thus enabling good image contrast to be

achieved. The carbon (C) foils were accelerated by NRL's Pharos II laser operating at $1.05\,\mu$ with 3.3-ns ($\pm$ 10%) driver pulses focused to 0.7–1.0-mm diameter. The x-ray source was approximately half that diameter. For some shots, a double foil target[4,5,8,10] was used, in which an impact foil, located behind the irradiated first foil (see Fig. 1), serves as a diagnostic of the motion of the first foil.

The source must be properly placed and timed to flash when the accelerated foil target moves into the view axis. A complication arises since the foil is also an x-ray emitter; therefore, we chose to radiograph the accelerated foil after it had ceased to emit, i.e., at a time 4–5 ns after the peak of the main (driver) pulse. An x radiograph of a C foil irradiated at 6.5×10^{12} W/cm^2 is shown in Fig. 2(a). The backlighting source's emission is imaged on the left and the foil's emission is imaged on the right. Furthest to the right, x rays emitted by the C blowoff plasma are imaged. Since the C foil is wider than the laser's focus, only the central, irradiated portion of the foil is accelerated, leaving the rest of the foil behind. The shadow of this stationary margin may be seen in the image of
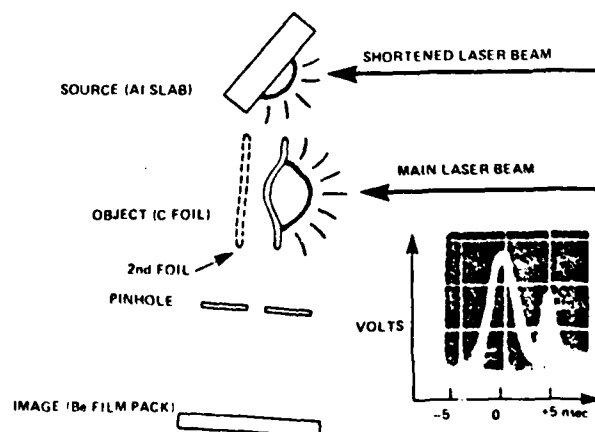
FIG. 1. Setup for flash x radiography (not to scale; angles are correctly drawn). Two 1.05-μ laser beams were focused through an $f/6$ lens onto separate targets. An absorption radiograph of the backlit object was recorded on x-ray film by a pinhole camera. Single or double carbon foils were employed as objects. Inset scope trace shows temporal shape of the main laser beam (peak at $t = 0$) and delay of the backlighter's laser pulse (5 ns).

[a] Also of Mission Research Corporation, Alexandria, VA

FIG. 2. (a) Flash x radiograph of a single, 1.3-mg/cm^2, carbon foil moving at 3×10^6 cm/s: 1. C plasma emission, 2. Al source emission, 3. shadow of unaccelerated C foil, 4. shadow of accelerated C foil. (b) Intensity contour profile of the main laser beam's focal spot. The middle contour level is drawn in thicker lines for comparison with (a). Incident irradiance was 6.5×10^{12} W/cm^2, with 90% of the laser energy in a 0.7-mm-diam spot. The peaks of the two laser pulses were 4.9 ns apart. Shot 81-10636.

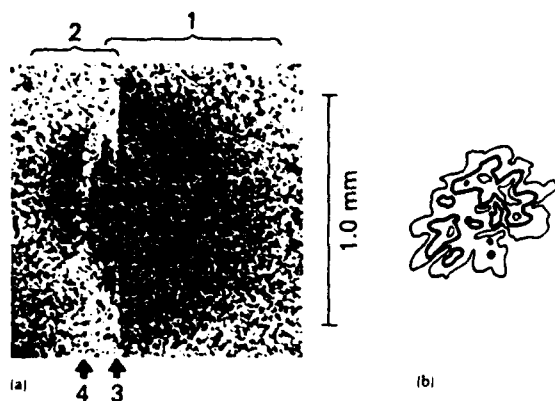the foil's own emission, i.e., as a self-radiograph [see Fig. 2(a)]. Since the accelerated portion of the C foil moves several foil thicknesses while radiating, some of the self-emission occurs to the left of the stationary foil's shadow. After the driver laser pulse shuts off, the accelerated portion ceases to radiate but continues to fly to the rear (left). The flash x-ray source was positioned just to the left of the stationary foil's shadow, but extended several hundred microns further to the left than the self-emission. Within this several hundred microns, the shadow of the moving foil is clearly seen and appears connected to the stationary margin. Several interesting measurements can be made from this representative image.

Using the stationary foil's shadow as a fiducial of the original position and taking the accelerated foil's shadow as the final position, an average velocity $v = s/\tau_d$ may be computed, with τ_d the delay of the x-ray flash. The result is 3×10^6 cm/s for this shot, for an energy density of 5×10^5 J/g on the axis of the driver laser. The energy in the accelerated foil was $E_t = (1/2)A\rho_a v^2$, where A is the area and ρ_a is the areal density. The initial 1.3 mg/cm^2 may be taken as ρ_a, since other measurements[4,5] indicate that less than 20% of the thickness would ablate by the time of observation. This leads to an estimate of total kinetic energy in the target of $E_t = (1/2)mv^2 = 1.5$ J. The incident laser energy F_L was 76. J, from which the coupling efficiency, one of the critical elements,[2] was $\eta = E_t/E_L \times 100 = 2\%$; higher values are achieved when a larger fraction of the target is ablated.[3] This efficiency combines laser absorption and hydrodynamic acceleration processes.

Ablation pressure may also be obtained from these data, using $P = \rho_a v/\tau_L$, where τ_L is the full width at half-maximum of the main laser. This leads to a pressure estimate of 1.4 Mbar, at an incident irradiance of 6.5×10^{12} W/cm^2. This is in good agreement with pressures inferred from measurements on ablation plasma,[4] which showed a value of 1.7 ± 0.3 Mbar at an absorbed irradiance of 6.5×10^{12}. The pressure and velocities obtained using the double foil tech-

nique[5] are in similar agreement with the value obtained here.

However, our pressure results do not agree with the recently reported[14] 1.0 Mbar (at increased irradiance, 3.6×10^{13} W/cm^2) which was found to be 5–10 × lower than cited measurements on ablation plasma.[14] In that work, a smaller spot size ($200 \times 300 \mu$m^2), a shorter driver pulse (0.8 ns), and a longer probe pulse (0.8 ns) were employed. At our 3-ns pulse length, lateral energy flow within the blowoff[8] extends as far as 140μ at about 1×10^{13} W/cm^2; therefore, we have used focal spot diameters several times this length to avoid a reduction in pressure due to lateral flow of energy to regions outside the focal spot. Also the longer pulse lengths achieve a more predominately steady state ablative acceleration. However, the actual source of the discrepancy noted in Ref. 14 remains unresolved.

A further measurement of the image in Fig. 2 shows that the on-axis thickness of the shadow of the moving foil is about 35–70 μ. Pinhole resolution (20 μ), velocity smearing (about 20–30 μ), and geometric factors including parallax, foil rotation, and foil curvature, make the 70 μ an upper bound for the axial extent of this highly absorbing foil. It is estimated from the x-ray attenuation of un-ionized C that the observed absorption images (measured to be mostly 1.6-keV photons, taking a 1/4-mm photon path) represent, as a lower bound, a density of about 3% of solid. Shorter path lengths, higher photon energies, and increased ionization would raise this estimate. Since the x-ray range at 1.6 keV is only 8 μ, there were at most a few solid bodies, if any, of this size or larger outside the shadow region of the accelerated foil; the high-density region was therefore localized to within the shadow.

The observation of a connecting structure of the shadow [Fig. 2(a)] strengthens the validity of both the double foil technique and the measurements of low preheat obtained for thin, planar targets.[6] One might intuitively expect that an accelerated disc would part from the unilluminated foil, leaving a break, through which plasma could flow and heat the rear of the foil. Double foil collisions would then be influenced by such spurious preheat. Previous investigation using optical[6] and double foil[5] techniques showed no evidence of such a plasma flow (see Fig. 1 in Ref. 6). The connecting structure observed in Fig. 2(a) evidently isolates the cool, rear surface from a hot plasma flow from the laser side. Thus, the x radiographs explain how low rear surface temperatures[6] of below 8 eV are maintained.

Looking at the finer details in Fig. 2(a), there is an evident waviness to both front and rear sides of the accelerated foil's shadow. However, neither the source emission nor C foils, of the type used, have nonuniformities of the amplitude and wavelength needed to explain the waviness.[11] On the other hand, irradiance nonuniformities are known to exist and to influence target motion. The laser's focal spot distribution was taken on the same shot and shows illumination nonuniformities of about 3:1, with a spatial wavelength of about 75–100 μ. The waviness in Fig. 2(a), which may be quantified as about 25% of the distance travelled, represents a lateral profile of nonuniformities in the target's velocity. The relationship between velocity nonuniformities and irradiance nonuniformities has been investigated previously and

430   Appl. Phys. Lett., Vol. 41, No. 5, 1 September 1982

Whitlock, Obenschain, and Grun   430

APPENDIX D

```
      PROGRAM LASER
C
C     THIS PROGRAM WRITTEN BY W. MICHAEL BOLLEN, MISSION
C     RESEARCH CORPORATION FOR THE LASER PHYSICS BRANCH AT
C     THE NAVAL RESEARCH LABORATORY.
C
C     ================COMMON BLOCK========================
C
      INTEGER CHAR,CMND
      COMMON/CLASER/IADE(72),NCHAR,CHAR,CMND,N1,N2,N3,N4,IGOT,
     & VAR(30,7),VARR(10)
     & /CENG/EDL(91),EDP(91),EFL(91),EFP(91),IL(20)
     & /CVEL/VB(91),VF(91),RMF(91),RMB(91)
C     ================================================
      OPEN (UNIT=1,FILE='LASERR.DAT')
      READ(1)VAR,VARR,IL
      CLOSE(UNIT=1)
      VARR(3)=-1
100   WRITE(5,110)
110   FORMAT(' '$)
C     READS A STRING
      CALL ADEIN(IGOT,IADE)
      NCHAR=1
      CALL NXTCHR
150   FORMAT(X,3I20)
      IF(CHAR.GE.65 .AND. CHAR .LE.90)GO TO 400
310   FORMAT(' UNINTELLIGABLE INPUT -- TRY AGAIN.')
      GO TO 100
C
C     DECODE COMMAND
C
400   CMND=CHAR-64
      CALL NXTCHR
      N1=0
      N2=0
      N3=0
      N4=0
      IF(NCHAR.GT.IGOT+1)GO TO 500
      CALL NUMBR(N1)
      IF(CHAR.NE.44)GO TO 500
      CALL NXTCHR
      CALL NUMBR(N2)
      IF(CHAR.NE.44)GO TO 500
      CALL NXTCHR
      CALL NUMBR(N3)
      IF(CHAR.NE.44)GO TO 500
      CALL NXTCHR
      CALL NUMBR(N4)
```

```
500     CALL EXCUTE
        IF(IGOT.EQ.-99)GO TO 600
        GO TO 100
600     CONTINUE
        OPEN(UNIT=1,FILE='LASERR.DAT')
        WRITE(1)VAR,VARR,IL
        WRITE(5,610)
610     FORMAT(X,'PROGRAM LASER TERMINATED')
        CLOSE(UNIT=1)
        STOP
        END
        SUBROUTINE NXTCHR
C
C       GET NEXT CHARACTER FROM INPUT STRING (IGNORING SPACES)
C
C       ===================COMMON BLOCK======================
C
        INTEGER CHAR,CMND
        COMMON/CLASER/IADE(72),NCHAR,CHAR,CMND,N1,N2,N3,N4,IGOT,
       & VAR(30,7),VARR(10)
C
C       ======================================================
10      CHAR=IADE(NCHAR)
        NCHAR=NCHAR+1
        IF(CHAR.EQ.32) GO TO 10
        RETURN
        END
        SUBROUTINE NUMBR(NUM)
C
C       GET A NUMBER FROM THE INPUT STRING IF THERE IS ONE
C       IF THERE IS NO NUMBER RETURN WITH NUM=0
C
C       ===================COMMON BLOCK======================
C
        INTEGER CHAR,CMND
        COMMON/CLASER/IADE(72),NCHAR,CHAR,CMND,N1,N2,N3,N4,IGOT,
       & VAR(30,7),VARR(10)
C
C       ======================================================
        NUM=0
        ISIGN=1
C
C       CHECK FOR NUMBER SIGN
C
        IF(CHAR.NE.45)GO TO 10
        ISIGN=-1
        CHAR=IADE(NCHAR)
        NCHAR=NCHAR+1
```

```
C
C       EXIT IF NEXT CHAR NOT NUMBER OR IF OUT OF CHARS
C
10      IF(CHAR.LT.48.OR.CHAR.GT.57)GO TO 20
        IF(NCHAR.GT.IGOT+1)GO TO 20
C
C       ADD A NEW DIGIT
C
        NUM=NUM*10+(CHAR-48)
        CHAR=IADE(NCHAR)
        NCHAR=NCHAR+1
        GO TO 10
20      NUM=ISIGN*NUM
        IF(CHAR.EQ.32)CALL NXTCHR
        RETURN
        END
        SUBROUTINE ADEIN(NCHAR,IARRAY)
        DIMENSION IARRAY(72)
        READ(5,10)IARRAY
10      FORMAT(72R1)
C
C       THIS READ AND DECODE IS PARTICULAR TO THE DEC-10
C       IN ORDER TO USE ON THE 11/10 OR THE 11/03 IT MUST
C       BE MODIFIED. THE INPUT ARRAY ELEMENT MUST BE MASKED
C       SUCH THAT THE RIGHT MOST BITS CONTAIN THE ASCII CODE
C       AND THE REST OF THE WORD IS FILLED WITH ZEROS.
C
C
C       FIND THE END OF THE LINE
C
        DO 200 J=1,72
        IF(IARRAY(73-J).NE."40)GO TO 40
200     CONTINUE
        J=73
40      NCHAR=73-J
        RETURN
        END
        SUBROUTINE EXCUTE
C
C       EXECUTE A COMMAND
C
C       =================COMMON BLOCK=====================
C
        INTEGER CHAR,CMND
        COMMON/CLASER/IADE(72),NCHAR,CHAR,CMND,N1,N2,N3,N4,IGOT,
     &  VAR(30,7),VARR(10)
     &  /CENG/EBL(91),EDP(91),EFL(91),EFP(91),IL(20)
     &  /CVEL/VB(91),VF(91),RMF(91),RMB(91)
```

```
C
C      =========================================================
1      GO TO (100,200,300,400,500,600,700,800,900,1000,1100,1200,
      &1300,1400,1500,1600,1700,1800,1900,2000,2100,2200,2300,
      &2400,2500,2600),CMND
C
C      A
C
100    WRITE(5,101)CMND,N1,N2,N3,N4
101    FORMAT(X,5I5)
       GO TO 6000
C
C      B
C
200    GO TO 5000
C
C      CHANGE
C
300    CONTINUE
       IF(N1.LE.0)GO TO 5000
       IF(N1.GT.30)GO TO 5000
       IF(N2.GT.0)GO TO 305
       GO TO 309
305    ITEMP=N2
       GO TO 335
309    CONTINUE
       WRITE(5,310)
310    FORMAT(' THE PRESENT VALUES ARE:')
       WRITE(5,1210)
       WRITE(5,320)
320    FORMAT(2X,'#',5X,'(1)',5X,'(2)',8X,'(3)',7X,'(4)',8X,
      &  '(5)',5X,'(6)')
       WRITE(5,1220) (VAR(N1,J), J=1,7)
       WRITE(5,330)
330    FORMAT(' WHAT VALUE DO YOU WISH TO CHANGE?',$)
       READ(5,*)ITEMP
335    N2=ITEMP+1
       WRITE(5,340)
340    FORMAT(' WHAT IS THE NEW VALUE?',$)
       IF(N2.EQ.2)GO TO 397
       READ(5,*)VAR(N1,N2)
345    WRITE(5,350)VAR(N1,1)
350    FORMAT(X,'TO CHANGE MORE VALUES FOR DET#',F3.0,
      &  'ENTER VAR #(IF NOT ENTER 0):'$)
       READ(5,*)ITEMP
       IF(ITEMP.EQ.0)GO TO 390
       N2=ITEMP+1
       GO TO 335
```

```
390   WRITE(5,395)
395   FORMAT(' THE NEW VALUES ARE:')
      WRITE(5,1210)
      WRITE(5,1220) (VAR(N1,J),J=1,7)
      GO TO 6000
397   READ(5,398)VAR(N1,2)
398   FORMAT(R5)
      GO TO 345
C
C     D
C
400   CONTINUE
      GO TO 5000
C
C     E
C
500   CONTINUE
      CALL ENERGY
      GO TO 6000
C
C     F
C
600   CONTINUE
      GU TO 5000
C
C     G
C
700   CONTINUE
      GO TO 5000
C
C     H
C
800   CONTINUE
      GO TO 5000
C
C     I
C
900   CONTINUE
      GO TO 5000
C
C     J
C
1000  CONTINUE
      GO TO 5000
C
C     K
C
1100  CONTINUE
```

```
      GO TO 5000
C
C     LIST
C
1200  CONTINUE
      IF(N1.LT.0)GO TO 1270
      WRITE(5,1210)
1210  FORMAT(X,/,'   DET#'X'TYPE'2X'ANG(TH)'2X'ANG(PHI)'9X'R',
     &  8X'CAL'7X'GAIN')
      IF(N1.GT.0)GO TO 1255
      DO 1250 I=1,30
      WRITE(5,1220) (VAR(I,J), J=1,7)
1220  FORMAT(X,F5.2,X,N5,F8.2,2X,F8.2,5X,F5.2,5X,2(F10.3,X))
1250  CONTINUE
      GO TO 1260
1255  WRITE(5,1220) (VAR(N1,J),J=1,7)
1260  GO TO 6000
1270  IF(N1.LT.-1)GO TO 1280
      IF(N2.GT.0 .AND. N2.LE.10)GO TO 1276
      WRITE(5,1271)VARR(1)
1271  FORMAT(' (1)-INCIDENT LASER ENERGY (J) ',F10.3)
      WRITE(5,1272)VARR(2)
1272  FORMAT(' (2)-TARGET ANGLE (DEG) ',F10.3)
      WRITE(5,1273)VARR(3)
1273  FORMAT(' (3)-SHOT #',F10.3)
      DO 1279 I=4,10
      WRITE(5,1278)I,VARR(I)
1278  FORMAT(' ('I2')',F10.3)
1279  CONTINUE
      GO TO 6000
1276  I=N2
      WRITE(5,1278)N2,VARR(N2)
1277  FORMAT(' VARR('I2') = ',F10.3)
      GO TO 6000
1280  CONTINUE
      DO 1281 I=1,20
      IF(IL(I).EQ.0)GO TO 1281
      WRITE(5,1282)I,IL(I)
1282  FORMAT(X,'PART DET#'I2' SAME AS LIGHT DET#'I2)
1281  CONTINUE
      GO TO 6000
C
C     M
C
1300  CONTINUE
      GO TO 5000
C
C     N
```

```
C
1400  CONTINUE
      GO TO 5000
C
C     O
C
1500  CONTINUE
      GO TO 5000
C
C     P
C
1600  CONTINUE
      GO TO 5000
C
C     Q
C
1700  CONTINUE
      GO TO 5000
C
C     R
C
1800  CONTINUE
      GO TO 5000
C
C     S
C
1900  CONTINUE
      GO TO 5000
C
C     TERMINATE PROGRAM
C
2000  CONTINUE
      IGOT=-99
      GO TO 5000
C
C     U
C
2100  CONTINUE
      GO TO 5000
C
C     V
C
2200  CONTINUE
      CALL VEL
      GO TO 5000
C
C     W
C
```

```fortran
2300  CONTINUE
      GO TO 5000
C
C     X
C
2400  CONTINUE
      GO TO 5000
C
C     Y
C
2500  CONTINUE
      GO TO 5000
C
C     Z
C
2600  CONTINUE
      GO TO 5000
5000  WRITE(5,5010)
5010  FORMAT(' INVALID COMMAND')
5020  GO TO 6000
6000  CONTINUE
6010  RETURN
      END
```

```fortran
      SUBROUTINE ENERGY
C
C     THIS SUBROUTINE HANDLES ENERGY CALCULATION
C     BASED ON INPUT CALORIMETRIC VALUES FROM CALORIMETERS
C
C     =================COMMON BLOCK=========================
C
      INTEGER CHAR,CMND
      COMMON/CLASER/IADL(72),NCHAR,CHAR,CMND,N1,N2,N3,N4,IGOT,
     & VAR(30,7),VARR(10)
     & /CENG/EBL(91),EBP(91),EFL(91),EFP(91),IL(20)
      EQUIVALENCE (EABS,VARR(1)),(ERN,VARR(3))
C
C     =========================================================
5     WRITE(5,10)
10    FORMAT(' WHAT IS THE SHOT # ? '$)
      READ(5,*)ERN
      IF(ERN.GT.0)GO TO 20
      WRITE(5,11)
11    FORMAT(' THE SHOT # MUST BE GREATER THAN ZERO.')
      GO TO 5
20    CONTINUE
      WRITE(5,100)
100   FORMAT(' WHAT IS THE INCIDENT LASER ENERGY (J)? '$)
      READ(5,*)EABS
      WRITE(5,90)
90    FORMAT(X,'WHAT IS THE TARGET ANGLE (DEG)?'$)
      READ(5,*)VARR(2)
      OPEN(UNIT=1,FILE='TEMP.TMP')
      WRITE(5,110)
110   FORMAT(' WE WILL DO FORWARD ANGLES FIRST.')
      CALL ECAL(EFL,EFP,1)
      WRITE(5,120)
120   FORMAT(' NOW WE WILL DO THE BACKWARD ANGLES.')
      CALL ECAL(EBL,EBP,2)
      CLOSE(UNIT=1)
      CALL ETOT(EFL,TEFL)
      CALL ETOT(EFP,TEFP)
      CALL ETOT(EBL,TEBL)
      CALL ETOT(EBP,TEBP)
      FPED=TEBP/(TEBP+TEFP)
      PEP=(TEBP+TEFP)/EABS
      WRITE(5,130)
130   FORMAT(X,'ENERGY IN LIGHT "FORWARD" EVERY 5 DEG.')
      WRITE(5,201)(EFL(I),I=1,91,5)
      WRITE(5,131)
131   FORMAT(X,'ENERGY IN PARTICLES "FORWARD" EVERY 5 DEG.')
      WRITE(5,201)(EFP(I),I=1,91,5)
```

```
      WRITE(5,132)
132   FORMAT(X,'ENERGY IN LIGHT "BACK" EVERY 5 DEG.')
      WRITE(5,201)(EBL(I),I=1,91,5)
      WRITE(5,133)
133   FORMAT(X,'ENERGY IN PARTICLES "BACK" EVERY 5 DEG.')
      WRITE(5,201)(EBP(I),I=1,91,5)
201   FORMAT(X,6F10.3)
      WRITE(5,200)TEFL,TEFP,TEBL,TEBP,FPEB,PEP
200   FORMAT(' TOTAL FORWARD ENERGY IN LIGHT=',F10.5,' JOULES',/,
     &            ' TOTAL FORWARD ENERGY IN PARTICLES=',F10.5,' JOULES',/,
     &            ' TOTAL BACKWARD ENERGY IN LIGHT=',F10.5,' JOULES',/,
     &            ' TOTAL BACKWARD ENERGY IN PARTICLES=',F10.5,' JOULES',/,
     &            ' FRACTION OF PARTICLE ENERGY BACKWARDS=',F10.5,
     &      /,        ' TOTAL PARTICLE ENERGY/ENERGY ABSORBED=',F10.5)
      WRITE(5,305)ERN,VARR(2)
      WRITE(5,303)
302   FORMAT(XI3XF6.3XF9.3XR5,F8.2,2X,F8.2,5X,F5.2,5X,2(F10.3,1X))
303   FORMAT(X,/,'   DET#'X'INPUT'X'CONV INP'X'TYPE'2X'ANG(TH)'2X,
     &'ANG(PHI)'9X'R'5X'CAL'7X'GAIN'/,8X'V'6X'J'15X'DEG'6X'DEG'9X'CM'
     &9X'J/CM2')
      OPEN(UNIT=1,FILE='TEMP.TMP')
      DO 300 I=1,20
      READ(1,301)TJ,TJ2
      IF(TJ.EQ.0.)GO TO 300
      WRITE(5,302)I,TJ,TJ2,(VAR(I,J),J=2,7)
300   CONTINUE
      DO 400 I=1,20
      READ(1,301)TJ,TJ2
      IF(TJ.EQ.0.)GO TO 400
      WRITE(5,302)I,TJ,TJ2,(VAR(I,J),J=2,7)
400   CONTINUE
      CLOSE(UNIT=1)
301   FORMAT(2F12.5)
305   FORMAT(/,35X' THE SHOT # IS:'F5.0/,30X ,'THE TARGET ANGLE IS:',
     &F6.1,/)
      RETURN
      END
```

```fortran
C     >>>>>>>>>>>>>>>>>>>>>>>>>>>>>>>>>>>>>>>>>>>>>>>>>>>>>>>>>>
      SUBROUTINE ECAL (EL,EP,ITY )
      DIMENSION EL(1),EP(1),ES(20,2)
      DO 1 I=1,20
      ES(I,1)=0.
1     ES(I,2)=0.
C     WRITE(5,401)(ES(J,1),ES(J,2),J=1,20)
      INUM=91
C     INUM IS THE NUMBER OF INT POINTS
      WRITE(5,100)
100   FORMAT(' HOW MANY LIGHT DETECTOR INPUTS?'$)
      READ(5,*)IE
      IF(IE.LT.0)GO TO 150
      CALL EX(EL,IE,ITY,ES,0 )
C     WRITE(5,401)(ES(J,1),ES(J,2),J=1,20)
150   WRITE(5,200)
200   FORMAT(' HOW MANY PARTICLE DETECTOR INPUTS?'$)
      READ(5,*)IE
C     WRITE(5,201)IE
201   FORMAT(X,'IE=',I5)
      IF(IE.LT.0)GO TO 350
      CALL EX(EP,IE,ITY,ES,-1 )
C     WRITE(5,401)(ES(J,1),ES(J,2),J=1,20)
350   DO 400 I=1,20
      WRITE(1,401)ES(I,1),ES(I,2)
C     WRITE(5,401)ES(I,1),ES(I,2)
401   FORMAT(2F12.5)
400   CONTINUE
      RETURN
      END
C     >>>>>>>>>>>>>>>>>>>>>>>>>>>>>>>>>>>>>>>>>>>>>>>>>>>>>>>>>>
      SUBROUTINE EX(E,IE,ITY,ES,FLAG)
C     ===============COMMON BLOCK========================
C
      INTEGER CHAR,CMND
      COMMON/CLASER/IADE(72),NCHAR,CHAR,CMND,N1,N2,N3,N4,IGOT,
     1 VAR(39,7),VAPR(10)
     &        /CENG/EDL(91),EBP(91),EFL(91),EFP(91),IL(20)
C
C     =====================  =========================
C
      DIMENSION E(1),ES(20,2),ETEMP(10),DET(10)
C     FOR SOME REASON CAN'T IMPLICITLY DIM ES
C     THE ABOVE DIMENSIONS LIMIT # INPUT PARTICLES TO 10
C     WRITE(5,10)IE
10    FORMAT(X,'IE=',I5)
```

```fortran
      DO 100 J=1,IE
      WRITE(5,150)
150   FORMAT(' ENTER (DET#,ENERGY(V)) ',$)
      READ(5,*)IDET,ETEMP(J)
C     WRITE(5,155)IDET,ETEMP(J)
155   FORMAT(X,I5,F12.3)
      IF(IDET.LE.0)GO TO 500
      IF(IDET.GT.30)GO TO 500
      DET(J)=IDET
      ES(IDET,1)=ETEMP(J)
C     WRITE(5,155)J,ES(IDET,1)
100   CONTINUE
C
C     CONVERT TO REAL UNITS AND GET ANGLE OF DETECTOR
C
C     WRITE(5,120)FLAG
120   FORMAT(X,'FLAG=',I5)
      IF(FLAG.LT.0)GO TO 300
      DO 200 J=1,IE
      IDET=DET(J)
      ETEMP(J)=ETEMP(J)*VAR(IDET,6)*VAR(IDET,5)**2/VAR(IDET,7)
      ES(IDET,2)=ETEMP(J)
200   DET(J)=VAR(IDET,3) VARR(2)
      GO TO 350
300   DO 250 J=1,IE
      IDET=DET(J)
      IDET2=IL(IDET)
      ETEMP(J)=(ETEMP(J)/VAR(IDET,7)-ES(IDET2,1)/VAR(IDET2,7))*
     &  VAR(IDET,6)*VAR(IDET,5)**2
      ES(IDET,2)=ETEMP(J)
250   DET(J)=VAR(IDET,3) VARR(2)
C     WRITE(5,251)
251   FORMAT(X,'HI')
350   CONTINUE
C
C     INTERPOLATE
C
C     ADD E=0 AT 90 DEG AS A POINT
      IE=IE+1
      ETEMP(IE)=0.0
      IF(ITY.EQ.1)DET(IE)=90
      IF(ITY.EQ.2)DET(IE)=270.
      NDEG=3
      IF(IE.LE.NDEG)NDEG=IE-1
      CALL RINT(ETEMP,IE,DET,E,ITY,NDEG)
500   RETURN
      END
C     ,)))))))))))))))))))))))))))))))))))))))))))))))))))))))
```

```
      SUBROUTINE ETOT(E,TOT)
      DIMENSION E(1)
C     THIS PROGRAM USES THE INTERPOLATED VALUES OF E
C     TO CALCULATE TOTAL ENERGY ASSUMING PHI SYMETRY AND
C     SYMETRY ABOUT THE LINE NORMAL TO THE TARET
      PI=3.141592654
      XANG=PI/130
C     I.E. XANG=1 DEGREE
      RI=0.0
C
C     INTEGRATE BY TRAPIZOIDAL RULE
C
      TOT=E(91)/2.0
      DO 100 I=2,90
      RI=RI+XANG
100   TOT=TOT+SIN(RI)*E(I)
C
C     NOW MULTIPLY TIMES STEP SIZE
C
      TOT=TOT*XANG
      TOT=2.0*PI*TOT
C     USE HAS BEEN MADE OF THE FACT THAT SIN(0)=0 AND
C     SIN(90)=1.0
      RETURN
      END
```

```
      SUBROUTINE VEL
C
C     THIS SUBROUTINE DOES THE VELOCITY CALCULATIONS
C
C     ==================COMMON BLOCK=====================
C
      INTEGER CHAR,CMND
      COMMON/CLASER/IADE(72),NCHAR,CHAR,CMND,N1,N2,N3,N4,IGOT,
     & VAR(30,7),VARR(10)
     & /CENG/EBL(91),EBP(91),EFL(91),EFP(91),IL(20)
     &          /CVEL/VB(91),VF(91),RMF(91),RMB(91)
      EQUIVALENCE (EADS,VARR(1))
      DIMENSION RPF(91),RPB(91)
C
C     ==========================================================
C
C     VF IS AN ARRAY CONTAINING THE FORWARD VELOCITY
C     VB IS AN ARRAY CONTAINING THE BACKWARD VELOCITY
C     RMF IS AN ARRAY CONTAINING THE FORWARD MASS
C     RMB IS AN ARRAY CONTAINING THE BACKWARD MASS
C     TRMF IS THE TOTAL FORWARD MASS
C     TRMB IS THE TOTAL BACKWARD MASS
C     ALL ARRAYS HAVE SEQ THETA VALUES SPACED 1 DEG
C     STARTING AT 0 (90) AND GOING TO 90 (270)
C
      IF(VARR(3).GT.0)GO TO  10
      WRITE(5,9)
9     FORMAT (' YOU MUST COMPUTE ENERGY FIRST!!')
      GO TO 500
10    WRITE(5,11)VARR(3)
11    FORMAT(' WE ARE DOING EXPERIMENTAL SHOT #',F6.0)
      WRITE(5,90)VARR(2)
90    FORMAT(' THE TARGET ANGLE IS'F7.2' DEGREES')
      WRITE(5,110)
110   FORMAT(' WE WILL DO FORWARD ANGLES FIRST.')
      CALL VCAL(VF,1)
      CALL MCAL(RMF,VF,EFL,EFP,1,RPF)
      WRITE(5,120)
120   FORMAT(' NOW WE WILL DO THE BACKWARD ANGLES.')
      CALL VCAL(VB,2)
      CALL MCAL(RMB,VB,EBL,EBP,2,RPB)
      CALL MTOT(RMF,TRMF,1)
      CALL MTOT(RMB,TRMB,2)
      CALL VP(RMF,VF,TRMF,VPF,1)
      CALL VP(RMB,VB,TRMB,VPB,2)
      CALL TMM(RMF,TRMF,TMMF,1)
      CALL TMM(RMB,TRMB,TMMB,2)
      CALL PTOT(RPF,TRPF,TRPPF,1)
```

```
      CALL PTOT(RPB,TRPB,TRPPB,2)
      WRITE(5,201)
      WRITE(5,300)(VF(I),I=1,91,5)
      WRITE(5,202)
      WRITE(5,300)(RMF(I),I=1,91,5)
      WRITE(5,203)
      WRITE(5,300)(RPF(I),I=1,91,5)
      WRITE(5,204)
      WRITE(5,300)(VB(I),I=1,91,5)
      WRITE(5,205)
      WRITE(5,300)(RMB(I),I=1,91,5)
      WRITE(5,206)
      WRITE(5,300)(RPB(I),I=1,91,5)
 300  FORMAT(X,8F10.3)
 201  FORMAT(X,' "FORWARD" VELOCITY EVERY 5 DEG:')
 202  FORMAT(/,' "FORWARD" MASS EVERY 5 DEG:')
 203  FORMAT(/,' "FORWARD" MOMENTUM EVERY 5 DEG:')
 204  FORMAT(/,' "BACKWARD" VELOCITY EVERY 5 DEG:')
 205  FORMAT(/,' "BACKWARD" MASS EVERY 5 DEG:')
 206  FORMAT(/,'"BACKWARD" MOMENTUM EVERY 5 DEG:')
      THHB=THHB+180.
      WRITE(5,400)VPF,VPB,TRMF,TRMB,THHF,THHB,TRPF,TRPPF,TRPB,TRPPB
 400  FORMAT(X,'FORWARD PARALLEL VELOCITY=',F10.5,'E-7 CM/S',/,
     &             X,'BACKWARD PARALLEL VELOCITY=',F10.5,'E-7 CM/S',/,
     &             X,'TOTAL MASS IN FORWARD ANGLES=',F12.5,'E-7 G',/,
     &             X,'TOTAL MASS IN BACKWARD ANGLES=',F12.5,'E-7 G',/,
     &             X,'M=0.5 TOTAL MASS (FORWARD) AT',F12.5,' DEG',/,
     &             X,'M=0.5 TOTAL MASS (BACKWARD) AT',F12.5,' DEG',/,
     &             X,'TOTAL FORWARD MOMENTUM=',F12.5,' DYNE-SEC',/,
     &             X,'TOTAL PARALLEL FORWARD MOMENTUM=',F12.5,' DYNE-SEC',/,
     &             X,'TOTAL BACK MOMENTUM=',F12.5,' DYNE-SEC',/,
     &             X,'TOTAL BACK PARALLEL MOMENTUM=',F12.5,' DYNE SEC')
 500  RETURN
      END
```

```
C      )))))))))))))))))))))))))))))))))))))))))))))))))))))))))))))
       SUBROUTINE VCAL (V,ITY )
       DIMENSION V(1)
       INUM=91
C      INUM IS THE NUMBER OF INT POINTS
       WRITE(5,100)
100    FORMAT(' HOW MANY VELOCITY INPUTS?'$)
       READ(5,*)IE
       IF(IE.LT.0)GO TO 350
       CALL VEX(V,IE,ITY)
350    RETURN
       END
C      )))))))))))))))))))))))))))))))))))))))))))))))))))))))))))))
       SUBROUTINE VEX(V,IE,ITY)
C      ==============COMMON BLOCK======================
C
       INTEGER CHAR,CMND
       COMMON/CLASER/IADE(72),NCHAR,CHAR,CMND,N1,N2,N3,N4,IGDT,
      & VAR(30,7),VARR(10)
C
C      ==========================================================
C
       DIMENSION V(1),ETEMP(10),DET(10)
C      THE ABOVE DIMENSIONS LIMIT # INPUT PARTICLES TO 10
       DO 100 J=1,IE
       WRITE(5,150)
150    FORMAT(' ENTER (DET#,VELOCITY) '$)
       READ(5,*)IDET,ETEMP(J)
       IDET=IDET+20
       IF(IDET.LE.20)GO TO 500
       IF(IDET.GT.30)GO TO 500
       DET(J)=FLOAT(IDET)
100    CONTINUE
C
C      CONVERT TO REAL UNITS AND GET ANGLE OF DETECTOR
C
       DO 200 J=1,IE
       IDET=DET(J)
       ETEMP(J)=ETEMP(J)*VAR(IDET,6)*VAR(IDET,7)
200    DET(J)=VAR(IDET,3)-VARR(2)
C
C      INTERPOLATE
C
       NDEG=2
       CALL RINT(ETEMP,IE,DET,V,ITY,NDEG )
500    RETURN
```

```
      END
C     )))))))))))))))))))))))))))))))))))))))))))))))))))))))))))
      SUBROUTINE MTOT(RM,TOT,ITY)
      DIMENSION RM(1)
C
C     THIS CALCULATES THE TOTAL MASS (EITHER FORWARD ITY=1
C     OR BACKWARD-ITY=2)
C
      PI=3.141592654
      XANG=PI/180
C     I.E. XANG=1 DEGREE
      RI=0.0
C
C     INTEGRATE BY TRAPIZOIDAL RULE
C
      TOT=RM(91)/2.0
      DO 100 I=2,90
      RI=RI+XANG
100   TOT=TOT+SIN(RI)*RM(I)
C
C     NOW MULTIPLY TIMES STEP SIZE
C
      TOT=TOT*XANG
      TOT=2.0*PI*TOT
C     USE HAS BEEN MADE OF THE FACT THAT SIN(0)=0 AND
C     SIN(90)=1.0
      RETURN
      END
C)))))))))))))))))))))))))))))))))))))))))))))))))))))))))))))))
      SUBROUTINE THH(RM,TRM,THH,ITY)
C
C     THIS FINDS THE ANGLE AT WHICH HALF OF THE TOTAL MASS IS
C     ACCOUNTED FOR
C
      DIMENSION RM(1)
      PI=3.141592654
      XANG=PI/180.
      HTRM=0.5*TRM
      TOT=0.0
      I=1
C     SIN(0)=0
      RI=0.
10    I=I+1
      RI=RI+XANG
      TOT=TOT+SIN(RI)*RM(I)*XANG*2.0*PI
      IF(TOT.GE.HTRM)GO TO 100
      IF(I.LE.90)GO TO 10
      I=I+1
```

```
100   THH=FLOAT(I-1)
      RETURN
      END
```

```
C))))))))))))))))))))))))))))))))))))))))))))))))))))))))))))))
      SUBROUTINE MCAL(RM,V,EL,EP,ITY,RP)
      DIMENSION RM(1),V(1),EL(1),EP(1),RP(1)
      DO 100 I=1,91
      IF(V(I).EQ.0.)GO TO 100
      TEMP=2.0*(EP(I))/V(I)
      RP(I)=TEMP
      RM(I)=TEMP/V(I)
100   CONTINUE
C     WRITE(5,200)(RM(J),J=1,91,5)
200   FORMAT(X,5F12.5)
      RETURN
      END
```

```
C       )))))))))))))))))))))))))))))))))))))))))))))))))))
        SUBROUTINE VP(RM,V,TRM,TOT,ITY)
        DIMENSION RM(1),V(1)
        PI=3.14159265A
        XANG=PI/180.
C       I.E. XANG=1 DEGREE
        RI=0.0
C
C       INTEGRATE BY TRAPIZOIDAL RULE
C
        TOT=0.0
        DO 100 I=2,90
        RI=RI+XANG
100     TOT=TOT+SIN(RI)*COS(RI)*RM(I)*V(I)
C
C       NOW MULTIPLY TIMES STEP SIZE
C
        TOT=TOT*XANG
        TOT=2.0*PI*TOT
        T(1)=TOT/TRM
C       USE HAS BEEN MADE OF THE FACT THAT SIN(0)=0 AND
C       SIN(90)=1.0
C       USE HAS BEEN MADE OF COS(90)=0.0
        RETURN
        END
```

```
C      ))))))))))))))))))))))))))))))))))))))))))))))))))))
       SUBROUTINE PTOT(RP,TOT,TOTP,ITY)
       DIMENSION RP(1)
C
C      THIS CALCULATES THE TOTAL MOM (EITHER FORWARD ITY=1
C      OR BACKWARD-ITY=2) BOTH TOT AND TOT PARALLEL.
C
       PI=3.141592654
       XANG=PI/180
C      I.E. XANG=1 DEGREE
       RI=0.0
C
C      INTEGRATE BY TRAPIZOIDAL RULE
C
       TOTP=0.0
       TOT=RP(91)/2.0
       DO 100 I=2,90
       RI=RI+XANG
       TEMP=SIN(RI)*RP(I)
       TOTP=TOTP+COS(RI)*TEMP
100    TOT=TOT+TEMP
C
C      NOW MULTIPLY TIMES STEP SIZE
C
       TOT=TOT*XANG
       TOTP=TOTP*XANG
       TOT=2.0*PI*TOT
       TOTP=TOTP*2.0*PI
C      USE HAS BEEN MADE OF THE FACT THAT SIN(0)=0 AND
C      SIN(90)=1.0
       RETURN
       END
```

```fortran
      SUBROUTINE RINT(ETEMP,IE,ANG,E,ITY,NDEG)
      DIMENSION ETEMP(1),ANG(1),E(1),A(10),B1(10),B2(10)
C     ETEMP IS YARRAY
C     ANG IS THE X ARRAY
C     IE IS THE NO OF PTS
C     E IS THE OUTPUT INTERPOLATED Y ARRAY
C     ITY TELLS IF FORWARD OR BACK
      DO 1 J=1,10
      A(J)=0.0
      B1(J)=0.0
1     B2(J)=0.0
      CALL COEF(A,B1,B2,ETEMP,ANG,NDEG+1,IE)
C     WRITE(5,10)(A(I),B1(I),B2(I),I=1,10)
10    FORMAT(X,3F10.3)
      IF(ITY.EQ.1)ANGLE=-1
      IF(ITY.EQ.2)ANGLE=179
      DO 300 J=1,91
      ANGLE=ANGLE+1
      FO=1.0
      FNEW=ANGLE-B1(2)
      I=1
      RINIT=A(I)*FO+A(I+1)*FNEW
100   IF(I.GE.NDEG)GO TO 200
      I=I+1
      FHOLD=FNEW
      FNEW=ANGLE*FNEW-B1(I+1)*FNEW-B2(I+1)*FO
      FO=FHOLD
      RINIT=A(I+1)*FNEW+RINTT
      GO TO 100
200   E(J)=RINTT
300   CONTINUE
C     NEG VEL AND ENERGIES ARE NON PHYSICAL SET=0.
      DO 500 I=1,91
500   IF(E(I).LT.0.)E(I)=0.0
      RETURN
      END
C     )))))))))))))))))))))))))))))))))))))))))))))))))))))))))))))
      SUBROUTINE COEF(A,B1,B2,Y,X,M,N)
C     M IS THE NUMBER OF TERMS=NDEG+1
C     N IS THE NUMBER OF INPUT POINTS
C
      DIMENSION A(1),B1(1),B2(1),Y(1),X(1),FOLD(10),FNEW(10)
C     THIS COMPUTES THE INTERPOLATING COEF A,B1,B2
      YFPROD=0.0
      XFPROD=0.0
      OLDPRD=FLOAT(N)
      DO 100 I=1,N
      XFPROD=XFPROD+X(I)
```

```fortran
100    YFPROD=YFPROD+Y(I)
       A(1)=YFPROD/FLOAT(N)
       B1(2)=XFPROD/FLOAT(N)
C      F1=1
C      CALCULATE F2
       DO 200 I=1,N
       FOLD(I)=1.0
200    FNEW(I)=X(I)-B1(2)
C      CALCULATE A(I),B1(I),B2(I)
       K=2
210    IF(K.GT.M)GO TO 1000
       XFPROD=0.0
       YFPROD=0.0
       FFPROD=0.0
C      COMPUTE INNER PRODUCTS
       DO 400 I=1,N
       YFPROD=YFPROD+Y(I)*FNEW(I)
       POLYSQ=FNEW(I)*FNEW(I)
       FFPROD=FFPROD+POLYSQ
400    XFPROD=XFPROD+X(I)*POLYSQ
       A(K)=YFPROD/FFPROD
       IF(K.EQ.M)GO TO 1000
C
C      CALCULATE COEF FO K+1TH ORTANG POLY
C
       B1(K+1)=XFPROD/FFPROD
       B2(K+1)=FFPROD/OLDPRD
       DO 500 I=1,N
       FHOLD=FNEW(I)
       FNEW(I)=(X(I)-B1(K+1))*FNEW(I)-B2(K+1)*FOLD(I)
500    FOLD(I)=FHOLD
300    OLDPRD=FFPROD
       K=K+1
       GO TO 210
1000   RETURN
       END
```

APPENDIX E

Fluid flow of ablated plasma from planar targets

M. J. Herbst and J. Grun[a]

Naval Research Laboratory, Washington, D.C. 20375

Using a novel diagnostic technique, the streamlines of the flow of plasma from a laser-irradiated target are observed for the first time. Implications for far-field ion measurements and similarity to a simple fluid flow are noted.

Although laser fusion will use spherical pellets, many laser-matter interaction experiments are performed on flat targets. If the results of planar experiments are to be scaled to spherical geometry, the effect on plasma profiles of differences in material flow from the target must be taken into account. The one-dimensional spherically divergent flow from a uniformly irradiated pellet affects plasma profiles at distances from the target which scale with the pellet radius. While it has long been recognized that the more complex multidimensional flow from a finite focal spot on a planar target must diverge at distances from the target surface which scale with the focal spot radius,[1] the first published results of multidimensional calculations which show the fluid flow pattern are only to appear soon.[2] In the present work, a new diagnostic technique allows the first *experimental* identification of the fluid flow lines from a planar target.

As shown in Fig. 1, foil targets are irradiated in the near field of an $f/6$ lens at a 6° angle of incidence by 100–500 J of Nd laser ($\lambda_0 = 1.054$-μm) radiation. With an incident pulse length of 3.5 nsec, and an irradiated spot diameter d_{90} (90 % energy content) of 1.4 mm, average irradiances within d_{90} are 1.5–8 TW cm^2. The focal-intensity distribution, as determined by equivalent focal-plane cameras, is relatively flat-topped, with approximately 2:1 intensity modulation across the central region. A camera with an array of pinholes is used to obtain time-integrated images of x-ray emission at 90° to the target normal. The 15-μm beryllium filters used on the camera allow imaging of photons with energy $h\nu \gtrsim 1$ keV.

A linear array of aluminum spots, 25 μm in diameter and 10 μm thick, are embedded as tracer material in 300 μm thick polystyrene (CH) target foils, which are then aligned so that the spots fall along a diameter of the laser-irradiated region. Since aluminum line emission is more intense than the CH continuum emission in the spectral band of the pinhole camera, streamlines of material flowing from the aluminum spots are identifiable by the tracks of strong x-ray emission [see Fig. 2(a)]. The perturbation of the flow pattern due to the addition of a second material should be minimal because: (1) the fully ionized mass densities for Al and CH differ by only 12 % at a given electron density in the blowoff plasma, and (2) the average velocity of ablated ions as determined by Faraday cups is the same for the two materials.

The observed flow pattern resembles that of the irro-

tational flow of a nonviscous compressible fluid from a circular orifice.[3] Near the target surface, the observed streamlines curve away from the target normal at a rate which is greatest for streamlines whose source points at the target surface are nearest the edge of the fluid source. Beyond $Z \simeq r_0$, where Z is the distance from the target surface and r_0 is the fluid source radius, the curvature is negligible and material flows outward in a straight path. The dearth of published multidimensional code results showing the fluid flow pattern leads us to make an interesting comparison between the data and the aforementioned potential flow. The latter, at least for low Mach numbers (nearly incompressible flow) and nearly paraxial streamlines, is well approximated by the solution to Laplace's equation subject to the boundary conditions at the source [see Fig. 2(b)]. To quantify the comparison, we consider the streamline angles θ relative to the target normal, which depend upon Z and upon the source position r of the streamline in the target plane. Fixing $Z = r_0/3$, where r_0 is the orifice radius for the Laplacian flow and the observed fluid source radius for the x-ray data, the dependences of θ upon r/r_0 are displayed in Fig. 2(c); the similarity of the two cases is striking. Of course, the model chosen does not accurately represent the case of the laser-ablated target, where fluid emerges at low velocity from the solid surface and is subsequently accelerated to sonic or supersonic speeds (where the flow is highly compressible). Nevertheless, the resemblance of the data to the Laplacian does suggest that some form of steady jet flow is present. Here, jet flow is meant to denote the fluid expansion, as opposed to the collisionless expansion of material from a circular orifice.

The fluid nature of the flow is not surprising, since the plasma radius $r_0 \simeq 850$ μm is much greater than the ion-ion collision mean-free-path ($\simeq 1$ μm at 0.1 critical density with $T \simeq 400$ eV as determined from x-ray spectra). One would also expect *steady* flow, since the laser pulse-length (3.5 nsec FWHM) is greater than the sound transit time ($\simeq 2$ nsec) across r_0. Experimental evidence that the flow is steady, at least for a large fraction of the duration of x-ray emission, is obtained from streak photography of images of $3/2\,\omega$ emission from the $n_c/4$ surface.[4] The position along the laser axis of this surface appears stationary for the duration of the $3/2\omega_0$ emission, a period of up to 3 nsec near the time of peak laser intensity.

The fluid flow affects the far-field particle diagnostics such as ion collectors or plasma calorimeters; we believe that these effects have not been previously noted.
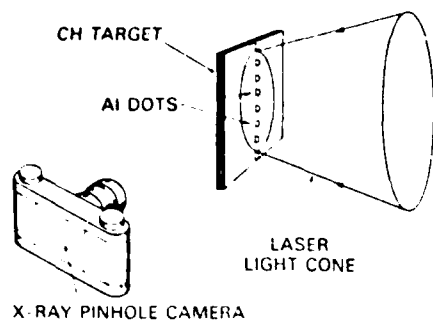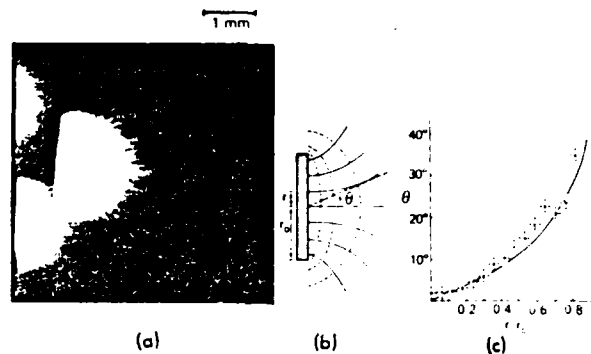
FIG. 1. Schematic illustration of experimental apparatus.

FIG. 2. Comparison of observed flow and simple fluid model. (a) Three x-ray images corresponding to pinhole diameters of 13, 28, and 54 µm, with laser incident from right. (b) Pattern of Laplacian flow from circular orifice. Dotted lines are constant velocity-potential surfaces and solid lines are fluid streamlines. (c) Dependence of streamline angle θ at $Z = r_0/3$ upon source position r in the target plane. Solid curve is for Laplacian flow pattern from (b), and points (x) with error bars are data from x-ray images such as (a).

First, the angular distribution of ablated mass observed by these diagnostics may be solely determined by the flow. Due to the shape of the jet near the target surface, a fluid velocity direction is imparted to each fluid element. As the density decreases away from the target, the flow eventually becomes collisionless, and the material drifting in the direction set by the jet expands due to random thermal motion. Since directed ablation velocities are generally significantly greater than ion thermal velocities, the thermal expansion will not greatly increase the angular range of material flow set by the jet. Indeed, charge collector and plasma calorimeter measurements indicate that half of the ablated mass appears in a cone about the target normal with a 40° half-angle[5]; this is consistent with the angular spread observed in the x-ray images, as well as with that given by the simple model of Fig. 2(b).

Ion detectors are further affected because the jet, except for any smearing due to thermal expansion after the flow becomes collisionless, maps regions of target surface into space. Since each point on the target surface feeds mass into a specific solid angle, a single ion detector far from the target samples only a portion of the irradiated region. To measure the parameters averaged over the focal spot, then, one should use an array of detectors at a range of angles. The error that may result if too few detectors are used depends upon the uniformity of the laser illumination at the target, the ratio of the directed ablation velocity to the plasma thermal velocity, and the solid angle subtended by the detectors used.

In conclusion, a new diagnostic technique allows the first experimental observation of the streamlines of material flow from the surface of a laser-irradiated target. Knowledge of the flow is required if the results of planar experiments are to be properly scaled to the spherical laser fusion problem. Implications of the fluid nature of the flow on far-field ion diagnostics in planar experiments are noted, as is a resemblance of the observed flow pattern to a very simple fluid flow. Future studies will include parametric variation of laser intensity and spot size, to assess the possible

effects on the shape of this flow. Detailed comparisons should then be possible with the results of multidimensional hydrodynamics calculations, which are more appropriate to the problem than the simple model presented here. In the present study, streamlines were identified by introducing localized sources at the target surface; it should be noted that the same phenomenon may be observed if localized sources arise due to unintentional effects, such as filamentation of the incident laser beam.[6]

The authors acknowledge valuable discussions with R. R. Whitlock, S. P. Obenschain, R. H. Lehmberg, B. H. Ripin, and C. K. Manka as well as the expert technical assistance of M. Fink, N. Nocerino, L. Seymour, and E. Turbyfill.

This work was supported by the U.S. Department of Energy and the Office of Naval Research.

[1] G. J. Pert, Plasma Phys. 16, 1019 (1974) and references contained therein.
[2] M. K. Matzen, R. L. McCrory, R. L. Morse, and C. P. Verdon (private communication).
[3] L. D. Landau and E. M. Lifshitz, Fluid Mechanics (Pergamon, London, 1959), Chaps. I and XII.
[4] M. J. Herbst, J. A. Stamper, R. R. Whitlock, R. H. Lehmberg, and B. H. Ripin, Phys. Rev. Lett. 46, 328 (1981).
[5] J. Grun, R. Decoste, B. H. Ripin, and J. Gardner, Appl. Phys. Lett. (to be published).
[6] M. J. Herbst, R. R. Whitlock, and F. C. Young, Phys. Rev. Lett. 47, 91 (1981).

APPENDIX F

Spot spectroscopy: Local spectroscopic measurements within laser-produced plasmas

M. J. Herbst, P. G. Burkhalter, J. Grun,[a] R. R. Whitlock, and M. Fink[b]

Naval Research Laboratory, Washington, D.C. 20375

(Received 8 March 1982; accepted for publication 7 May 1982)

Use of a locally embedded tracer in laser-irradiated solid targets yields a localized source of diagnostic x-ray line radiation in the blowoff plasma. This technique potentially eliminates problems of chord integration over regions of varying density and temperature in an inhomogeneous plasma, and reduces complications due to plasma opacity effects in the interpretation of spectra. Spectra obtained in an experimental test of this new technique are of a quality superior to those obtained from standard laser-produced plasmas, and should provide the best tests to date of spectroscopic models for these plasma conditions.

PACS numbers: 52.50.Jm, 52.25.Ps

INTRODUCTION

Density and temperature profiles are directly related to energy absorption and transport processes in plasmas produced by laser irradiation of solid targets. Therefore, measurements of these plasma parameters play a central role in experiments addressing the physics relevant to laser-driven nuclear fusion.[1] At the densities and temperatures of interest, x-ray spectroscopy provides one viable method for performing these measurements.[2,3]

There are two major drawbacks to the use of standard spectroscopic techniques in these plasmas. First, the measurements are integrated along a diagnostic line of sight through an inhomogeneous plasma. Second, effects of plasma opacity on the radiation exiting the plasma are non-negligible at the higher densities of interest.[4,5] One could use straightforward inversion techniques to obtain spatially resolved emissivities from the chord-integrated data if the plasmas were optically thin and axisymmetric,[3] but the additional complication of spatially varying opacity makes inversion much more difficult. More typically, one predicts the plasma profile using a hydrodynamics computer code and compares the experimentally observed spectrum with those calculated for chord integrations across the inhomogeneous plasma.[6,7] One is dependent in that case upon the correctness of the hydrodynamics model as well as the atomic physics model; one would obviously prefer to make direct determinations of density and temperature, independently of the hydrodynamics.

In the present work, a new spectroscopic method is described which circumvents the problem of plasma inhomogeneity and reduces the effects of plasma opacity. Spot spectroscopy, the new technique, differs from standard spectroscopic techniques in that the source of diagnostic radiation is locally embedded into the solid target before laser irradiation. As recently demonstrated,[8] the tracer material which is ablated by the laser can be confined collisionally in the hydrodynamic flow from the target; this yields a source of diagnostic lines which is localized within the blowoff plasma. In Sec. I, we explain the target fabrication procedure and describe a method for *in situ* measurement of the spectrograph magnification. Data obtained with the new technique are compared with standard spectroscopic data in Sec. II, which also contains a discussion of caveats and remaining questions. Finally, we assess the new technique in Sec. III.

I. EXPERIMENTAL TECHNIQUES

A. Target fabrication

For the proof-of-principle experiment, we choose polystyrene targets with embedded aluminum tracers. The tracer is so chosen because collisional radiative equilibrium (CRE) computer models suggest the utility of aluminum lines for measurement of temperatures and densities of interest.[9] The polystyrene is chosen because it is a common and easily fabricated target material. Also, its lower atomic number Z increases the ratio of the aluminum tracer emission to the surrounding plasma emission and reduces the opacity of the surrounding plasma to the tracer emission.

A two-step process is used to fabricate these targets. The first step is the evaporation of the tracer material onto a soaped-glass substrate using the standard technique of vacuum evaporation from a hot filament source. The thin film of TEEPOL 610 detergent[10] on the glass prevents the aluminum from adhering better to the glass than it will to the polystyrene. To achieve local deposition of the aluminum, bimetal masks into which the desired patterns have been chemically etched are magnetically clamped in intimate contact with the glass substrate; for the present experiment, these patterns are circular spots of various diameters. In the second step of the process, polystyrene dissolved in butyl acetate is cast over the aluminum-coated glass substrate. When dry, the composite is lifted and the aluminum is embedded in the

1418   Rev. Sci. Instrum. 53(9), Sept. 1982   0034-6748 82 091418-05$01.30   © 1982 American Institute of Physics   1418

polystyrene; the surface of the tracer is flush with that of the plastic.

B. The proof-of-principle experiment

Except for the presence of the tracer in the target, the experimental arrangement for the new technique is much the same as for standard x-ray spectroscopy. As shown in Fig. 1, the targets are irradiated with 50–250J of Nd laser radiation (1.054 μm wavelength) in a 4–5-ns pulse. We choose to operate at two focal conditions for this experiment. First, at the best focus of our $f/6$ input lens, we use focal diameters (90% laser energy content) near 100 μm, and spatially averaged irradiances up to 5 $\times$ 10^{14} W/cm^2. Because larger focal diameters are required to minimize edge effects in planar experiments, targets are also placed in the quasinear field of the focusing lens; intensities between 10^{12} and 10^{13} W/cm^2 are obtained with focal diameters of 800–1000 μm.

The aluminum line radiation in the 5–8 Å spectral region is detected using an x-ray crystal spectrograph with a viewing axis parallel to the target surface. Spectral dispersion is achieved through use of a PET crystal, and spatial resolution in the direction on the film which is orthogonal to the spectral dispersion is accomplished with an entrance slit. As shown in Fig. 1, the slit is oriented to yield spatial resolution in the direction along the laser axis; resolution in the other two spatial dimensions results from the knowledge of the position of the localized tracer within the focal spot. The slit is located 4–5 mm from the target, which represents a tradeoff between light collection efficiency and slit survivability; even at this distance, the 25-μm-thick nickel slit substrate is occasionally destroyed by target debris during a laser shot. Another compromise must often be made between spatial resolution and detectability of relevant spectral lines. To improve spatial resolution along the laser axis, one must reduce the slit width, sacrificing spectral intensity; to recover the spectral intensity, one may choose to increase the implanted spot diameter, reducing spatial resolution in the other two dimensions. For the purposes of this study, slit widths between 4 and 30 μm and tracer spot diameters between 40 and 250 μm are used. The spectra are recorded on Kodak No-Screen film, for which a film model[11] based upon an absolute calibration[12] is available. A beryllium filter of nominally 15 μm thickness protects the film from visible exposure.

C. *In situ* measurements of spectrograph magnification

In principle, one may use the measured slit-to-film and slit-to-source distances to calculate the magnification of the spectrograph. However, given the uncertainties with which the exact paths of diffracted rays of various wavelengths can be measured, we prefer a direct *in situ* measurement of the spectrograph magnification.

To measure the magnification *in situ*, we devised a
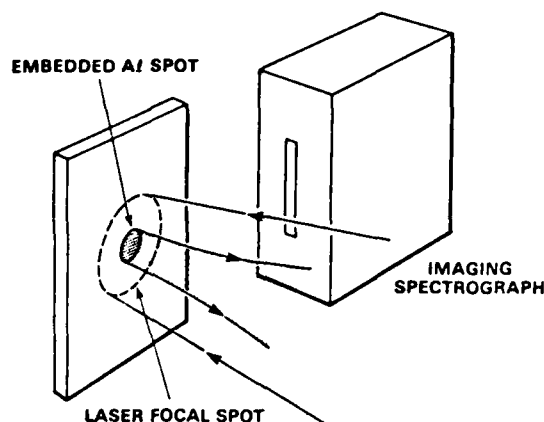
special double target. An aluminum foil is placed in the usual target position, mounted to a glass substrate to prevent target bowing. A few hundred microns in front of the Al foil, toward the laser, a foil of copper backed by glass is mounted. The foils are aligned so that part of the incident laser beam strikes the edge of the Cu foil, producing Cu line emission, while the rest misses the Cu and propagates the additional distance to the Al surface. The spectrograph image then contains Cu and Al lines, but the Al lines extend beyond the end of the Cu lines by a distance $L' = ML$ corresponding to the distance L between the two target foils multiplied by the spectrograph magnification M. As L may be accurately measured under a microscope, M is experimentally determined by the measurement of L'.

One potential complication with this procedure arises unless the spectrograph axis is closely aligned with the target surface; if it is not, the observed separation between the Cu and Al may be lessened due to geometrical foreshortening. To assure that this is not a problem, we add a flag to the target, a 2-mm-wide and 125-μm-thick glass strip on the side between the irradiated target and the spectrograph slit. This flag is offset toward the laser from the Cu surface and is mounted with its broad face parallel to the Cu and Al target surfaces. Given its location, it casts a shadow on the spectrograph; this shadow is observed on the spectrum as a gap in the Al and Cu spectral lines. By comparing the dimension of this gap with the thickness of the flag, the angle at which the flag and, therefore, the targets are viewed can be determined; any angular misalignment causes an increase in the shadow dimension which depends on the known flag width.

II. RESULTS AND DISCUSSION ·

A. Results of experiment and comparison of techniques

To allow a comparison to be made between spot spectroscopy and standard spectroscopic techniques, we use
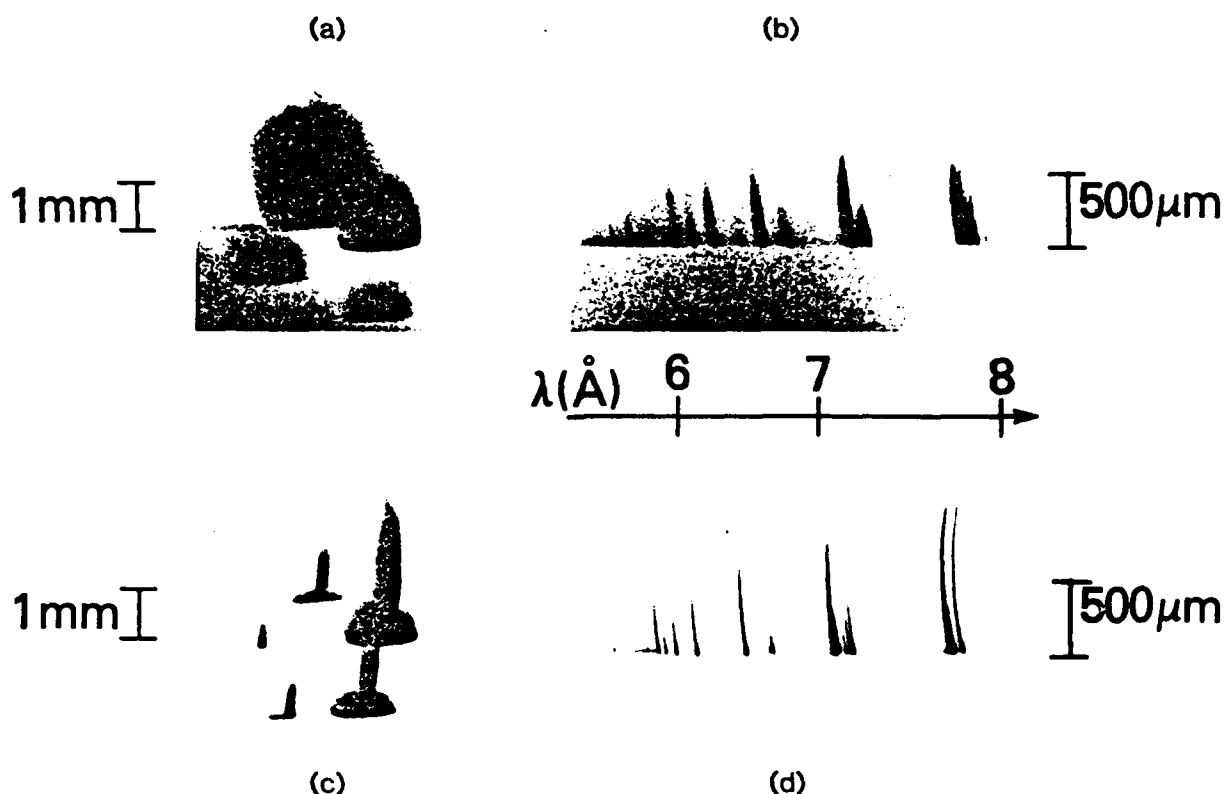
(a)   (b)

(c)   (d)

FIG. 2. Qualitative comparison between data obtained with an Al foil target and da .. acquired using a CH plastic target locally embedded with Al. The vertical axis for (a) through (d) corresponds to the laser axis, with the laser incident from above and the target surface at bottom. (a) is obtained with Kodak 3490 film, and (b) through (d) are on Kodak No-Screen Film. (a) x-ray pinhole camera images, obtained with an array of pinholes (5–55 μm diameter), for an Al foil target. Laser intensity $I_0 \simeq 3 \times 10^{12}$ W/cm^2, due to 100 J focused to 1100-μm-diam spot (90% energy content). (b) Spectrum obtained for Al foil target at $I_0 \simeq 8 \times 10^{12}$ W/cm^2, with 110 J focused to 600-μm-diam spot. (c) Pinhole images as in (a), but for a CH target embedded with 180-μm-diam Al spot. 225 J of laser energy focused to 900-μm-diam spot yields $I_0 \simeq 8 \times 10^{12}$ W/cm^2. (d) Spectrum from same shot as (c).

both simple Al foil targets and CH targets with embedded Al spots. A pinhole camera filtered to detect photons with energy $h\nu \gtrsim 1$ keV looks at the blowoff plasma along the same axis but from a position diametrically opposite the spectrograph.

Typical images of an aluminum foil plasma, obtained with a pentagonal array of pinholes with diameters between 5 and 55 μm, are shown in Fig. 2(a). An x-ray spectrum obtained with an aluminum foil target can be seen in Fig. 2(b), although for somewhat different conditions than apply for Fig. 2(a). The horizontal edge at the bottom of the spectrum is the target surface, from which regions of strong line emission extend over distances of several hundred microns.

The x-ray pinhole images and spectrum for a CH target with embedded Al can be seen in Figs. 2(c) and 2(d), respectively; this data is analogous to that shown in Figs. 2(a) and 2(b) for an aluminum foil target. Note that Figs. 2(c) and 2(d) are obtained on the same data shot, but that the conditions of this shot do not exactly correspond with those of either Fig. 2(a) or 2(b). The comparison between the techniques, therefore, is qualitative rather than quantitative.

Inspection of the pinhole camera images reveals that, indeed, the source volume for the Al x-ray emission can

be significantly reduced through the use of a CH target with an embedded Al spot. As expected on the basis of Ref. 8, a collisionally confined channel of aluminum flow from the embedded tracer can be identified as the track of stronger x-ray emissivity in the images of Fig. 2(c). This is a much smaller source volume than the aluminum foil plasma in Fig. 2(a) [the 20% difference in laser focal spot diameter between Figs. 2(a) and 2(c) is not a major factor in this reduction]. Even larger reductions in source size are observed when smaller embedded spots are used. To date, we have embedded spots as small as 25 μm in diameter,[8] a limit imposed by the availability of masks for tracer evaporation. In principle, the ultimate limit is set by the ability of the plasma to collisionally confine the tracer; as ion–ion mean free paths are estimated to be less than 1 μm even at electron densities down to 10% of critical density for the incident laser, there is considerable room for further source reduction.

A dramatic improvement in spectral resolution results from the reduction in source volume. With an Al foil target, as in Fig. 2(b), the spectral widths of the lines near the target surface are quite broad; the widths exceed those expected for other broadening mechanisms, and reflect source broadening due to the large Al plasma extent transverse to the laser axis. In contrast, line widths

near the target surface are much narrower, as in Fig. 2(d), when a CH target with embedded Al is used. Several sets of lines which appear to the naked eye to be totally unresolved in Fig. 2(b) are clearly isolated in Fig. 2(d). These data are obtained with the larger focal spot; a similar effect is observed at the smaller focal spot.

Two other important results of the reduced source volume are that the effects of plasma inhomogeneity can be virtually eliminated and that the effect of plasma opacity can be greatly reduced. Without embedded tracers, one might try to minimize inhomogeneity and opacity effects by reducing the size of the plasma to be studied. For laser-produced plasmas, this would be accomplished by minimizing the laser focal diameter. One could not expect, however, to approach the small plasma sizes which seem possible with embedded tracers. Even if one could localize the laser energy to micron scales, lateral transport of energy by plasma processes would tend to broaden the spectroscopic source, increasing the effect of plasma opacity. Additionally, this source would still have problems due to its inhomogeneity; one would still be sampling regions of widely different density and/or temperature. With the plasma resulting from an embedded tracer, one can hope to obtain not only very small source-plasma diameter, minimizing opacity effects, but also a nearly homogeneous source, since the embedded spot diameter can be made much smaller than the irradiated focal diameter. The reduction in opacity, of course, is realized only if the tracer is embedded in a target material with lower opacity than the tracer at the wavelengths of interest.

Given that the source volume for emission is much smaller with the embedded Al tracer than for an Al foil, one might have anticipated greater problems with detectability of the spectrum than were actually encountered. In Fig. 2(d), the spectral lines are detectable several hundred microns from the target surface, just as far as they are in the spectrum shown for the pure Al target (though under somewhat different conditions) in Fig. 2(b). In fact, even continuum emission is detectable near the target surface in Fig. 2(d); this continuum is not observable when plastic targets without the embedded spots are irradiated, indicating that the source of the continuum is the Al tracer material. For the stronger lines in the spectrum, such as the heliumlike and hydrogenlike resonance lines ($1s^2 \, {}^1S_0-1s2p\,{}^1P_1$ and $1s-2p$, respectively) and the helium-like intercombination line ($1s^2 \, {}^1S_0-1s2p\,{}^3P_1$), exposures near the target surface tend to saturate the film except on shots where smaller embedded spots (40 μm diameter) and narrower slits (4 μm wide) are used. Weaker spectral lines such as the higher Rydberg members are lost in this limit. Spot spectroscopy does appear to be practicable, then, at least with laser energies comparable to ours.

B. Caveats and remaining questions

Spot spectroscopy has advantages over standard spectroscopic techniques in laser produced plasmas; however, there are a few caveats to be mentioned. First, source localization requires a collisional plasma. This restriction may prevent use of the technique at much higher laser intensities or at much longer laser wavelengths, where higher plasma temperatures and the generation of suprathermal ions produce longer ion-ion mean free paths, destroying the confinement of the embedded tracer. Of course, spot spectroscopy is not limited to laser-produced plasmas; any method such as ion-beam irradiation or electrical discharge which creates collisional plasma from an initially solid target may be used to generate the spectroscopic source.

A second caveat concerns the ability of the technique to serve as a plasma diagnostic. If we are to regard the plasma flowing from the embedded tracer as a local spectroscopic probe for density and temperature measurements, then we want to be certain that conditions in the tracer plasma correspond to those in the surrounding plasma. Certainly, the visualizations of the hydrodynamic flow pattern, as shown in Ref. 8, strongly suggest that there is *pressure* equilibrium between Al tracers and CH plasmas. In the future we will determine by comparison with other diagnostics when there is also density and temperature equilibration.

Even if equilibration is shown for the present data, spectroscopic models show that each tracer element may be used only within limited ranges of density and temperature[9]; to diagnose a wide range of parameters, one must use a variety of tracer materials.[13] The required equilibration must be demonstrated for each of these diagnostic elements.

Another issue is the effect of time integration upon the data. Much as with chord integration, time integration can complicate interpretation of the spectra if plasma parameters are varying during the x-ray emission. In the present experiments, we believe that the laser pulse is varying sufficiently slowly so that the plasma profiles are nearly in a steady state during the x-ray emission. Experimental evidence[14] for this is provided by streak photography of imaged $\frac{1}{2}\,\omega_0$ emission (where ω_0 is the incident laser frequency), which indicates that the location of the $n_c/4$ surface, and, therefore, all higher density surfaces, is nearly steady for a few nanoseconds around the peak of the laser pulse (when the x-ray emission is observed to occur[15]). Even though we believe time-integration effects to be minimal for our case, one can hope to obtain time resolution with spot spectroscopy in one of two ways. First, one may replace the film with an x-ray streak camera to obtain a time history on a single shot, though one cannot simultaneously obtain the complete spectrum of wavelengths λ for all positions z relative to the target surface. An alternative method is to deposit a tracer of lesser thickness at a prescribed depth beneath the surface of the target (this involves a more difficult, though realizable, target fabrication procedure). By varying the depth d and thickness t of the tracer, one controls the time interval during which tracer emission occurs. On a single shot, then, one obtains information for all λ and z, but at only a single time; t and d are varied on a shot-to-shot basis to generate a time history.

III. CONCLUSIONS

The advantages of the new technique are clear for measurements of density and temperature profiles in plasmas created by Nd-laser interaction with solid targets. Localization of the source of line radiation allows spectroscopic measurements to be made with three dimensions of spatial resolution. Since this alleviates the problem of chord integration over regions of widely varying density and temperature, one generally will not need to account for the profile along which one is integrating in order to obtain agreement with spectroscopic models.[5] Therefore, the new technique also provides improved checks of spectroscopic models. As added bonuses: (1) the reduced source broadening improves spectral resolution in the data obtained, and (2) the interpretational problems raised by opacity effects in the plasma are much reduced, especially if the surrounding target material has much lower Z than the tracer.

The present work represents a significant step toward obtaining improved measurements of density and temperature in laser-produced plasmas. Detailed analysis of the present data, including extensive comparisons with spectroscopic models, is the subject of a future work. Further experiments are also required to fully answer all of the questions raised in Sec. IIB.

IV. ACKNOWLEDGMENTS

Valuable discussions are acknowledged with Dr. D. Duston, Dr. D. Matthews, Dr. B. H. Ripin, and Dr. H. Griem. The expert technical assistance of N. Nocerino,

[a] Mission Research Corporation, Alexandria, Virginia 22312.
[b] Sachs Freeman Associates, Bowie, Maryland 20715.
[1] J. Nuckolls, L. Wood, A. Thiessen, and G. Zimmerman, Nature 239, 139 (1972).
[2] W. Lochte-Holtgreven, in *Plasma Diagnostics*, edited by W. Lochte-Holtgreven (Wiley Interscience, New York, 1968), pp. 190 ff.
[3] H. R. Griem, *Plasma Spectroscopy* (McGraw-Hill, New York, 1964).
[4] D. Duston and J. Davis, Phys. Rev. 21 A, 932 (1980).
[5] J. P. Apruzese, P. C. Kepple, K. G. Whitney, J. Davis, and D. Duston, Phys. Rev. 24 A, 1001 (1981).
[6] D. Duston, J. Davis, and P. C. Kepple, Phys. Rev. 24 A, 1505 (1981).
[7] K. G. Whitney and P. C. Kepple, J. Quant. Spectrosc. Radiat. Transfer 27, 281 (1982).
[8] M. J. Herbst and J. Grun, Phys. Fluids 24, 1917 (1981).
[9] D. Duston and J. Davis, Phys. Rev. 21 A, 1664 (1980).
[10] Manufactured by Shell Oil Co. Reference to a company or product name does not imply approval or recommendation of the product by the U.S. Naval Research Laboratory or its contractors to the exclusion of others that may be suitable.
[11] D. B. Brown, J. W. Criss, and L. S. Birks, J. Appl. Phys. 47, 3722 (1976).
[12] C. M. Dozier, D. B. Brown, L. S. Birks, P. B. Lyons, and R. F. Benjamin, J. Appl. Phys. 47, 3732 (1976).
[13] V. A. Boiko, S. A. Pikuz, and A. Ya Faenov, J. Phys. B 12, 1889 (1979).
[14] M. J. Herbst, J. A. Stamper, R. H. Lehmberg, R. R. Whitlock, F. C. Young, J. Grun, and B. H. Ripin, to appear in *Proceedings of the 1981 Topical Conference on Symmetry Aspects of Inertial Fusion Implosions*, edited by S. Bodner, NRL.
[15] B. H. Ripin, R. Decoste, S. P. Obenschain, S. E. Bodner, E. A. McLean, F. C. Young, R. R. Whitlock, C. M. Armstrong, J. Grun, J. A. Stamper, S. H. Gold, D. J. Nagel, R. H. Lehmberg, and J. M. McMahon, Phys. Fluids 23, 1012 (1980); and 24, 990 (1981).

APPENDIX G

```
TLIST
1  ASCII   PROG    768
2  BINARY  PROG  73728
3  ASCII   PROG  73728
4  NEW            1024
5  BINARY  DATA   1024
6  BINARY  DATA   1024
7  ASCII   PROG  10240
8  BINARY  PROG  26880
9  LAST            768
```

```
FIND1
OLD

LIST
100 INIT
110 REM -- 7612 / 4907 UTILITY PROGRAM LOADER
120 REM
130 FIND 2
140 CALL "BOLD"
150 END
```

FILE 2 IS THE BINARY VERSION OF FILE 3

```
FIND3
OLD

LIST
1 INIT
2 ON SRQ THEN 7760
3 GO TO 100
4 REM                  [ Set up a shot ]
5 GO TO 760
8 REM                  [ Acquire shot data from 7612's ]
9 GO TO 1890
12 REM                 [ Quick graph of all channels ]
13 GO TO 6970
16 REM                 [ Graph the current waveform ]
17 GO TO 5490
20 REM                 [ List comment file ]
21 GO TO 2630
24 REM                 [ Differentiate waveform ]
25 GO TO 4210
29 GO TO 4650
32 REM                 [ Pulse analysis from min/max ]
33 GO TO 3560
36 REM                 [ Recall waveform from disk ]
37 GO TO 2190
40 REM                 [ Directory of disk ]
41 GO TO 1810
44 REM                 [Arm all channels ]
45 GO TO 7790
48 REM                 [ store or restore 7612D mainframe settings]
49 GO TO 7850
60 REM                 [ Create general comment file ]
61 GO TO 1370
```

```
54 REM              [ Integrate waveform ]
65 GO TO 4110
68 REM              [ Apply taper to waveform ]
69 GO TO 4390
72 REM              [ Pulse analysis from histogram ]
73 GO TO 3680
76 REM              [ Select segment of waveform ]
77 GO TO 3090
80 REM              [ subroutine to analize charge collector traces ]
81 GO TO 9000
100 REM    '''''''''''''''''''''''''''''''''''''''''''''''''''''''''''''
110 REM    ''                                                         ''
120 REM    ''        Custom 7612 utility software          V1.0       ''
130 REM    ''                                                         ''
140 REM    ''    Heavily modified WP1310 software with additions to   ''
150 REM    ''    support three 7612D's, and the 4907 file manager.    ''
160 REM    ''    Some routines have been removed.                     ''
170 REM    ''                                                      ''   ''
180 REM    ''    Mike Wadzita  Tektronix, Inc.   Rockville, Md.       ''
190 REM    ''                                                         ''
200 REM    '''''''''''''''''''''''''''''''''''''''''''''''''''''''''''''
210 DIM A$(500),I$(75),X$(6000),Z$(60),D$(600)
220 DIM F(9),Q(20,2),Z1(6)
230 G$=""
240 J$=CHR(13)
250 REM CHANGE TO ORIGINAL PROGRAM.THIS SAVES CHANNEL NAMES IN FILE
260 REM NUMBER 5.STATEMENTS CHANGED OR NEW ARE:
270 REM 250-252,411,AND 951,852.
280 REMZ$="CHARGECUPACHARGECUPBCHARGECUPCCHARGECUPDCHARGECUPECHARGECUPF"
290 FIND 5
300 READ @33:Z$
310 I$=""
320 I$=I$&""
330 A1=0
340 B1=0
```

```
350 C1=0
360 D1=0
370 F=0
380 F(9)=1
390 Q=-1
400 Z1=10
410 REM
420 REM  -- Initialize the 4907 --
430 REM
440 PRINT "LI    STARTUP PROCEDURE↵↵"
450 PRINT "Be sure the 4907 & ALL 7612's are powered on at this point"
460 PRINT "Insert the data disk in the 4907 and close drive door,"
470 PRINT "Make sure tape is not write protected"
480 PRINT "then press <RETURN>";
490 INPUT X$
500 CALL "time",X$
510 IF X$<>"" THEN 560
520 PRINT "Enter the date & time as --> DD-MMM-YY HH:MM:SS"
530 PRINT "↵--------- -------- AAAAAAAAAAAAAAAAAAAA";
540 INPUT X$
550 CALL "SETTIM",X$
560 CALL "DSTAT",0,X$
570 Y$=SEG(X$,129,1)
580 IF Y$<>"0" THEN 610
590 PRINT "↵Disk is being mounted . . . "
600 CALL "MOUNT",0,X$
610 I1=POS(X$,"FREE",1)
620 Y$=SEG(X$,I1-9,9)
630 I2=VAL(Y$)
640 PRINT "↵There are ";I2;" free bytes available"
650 PRINT "↵Storage requirements are"
660 PRINT "↵    Comment file          -    2032 bytes"
670 PRINT "↵    256 point waveform     -    2540 bytes"
680 PRINT "↵    512 point waveform     -    4826 bytes"
690 PRINT "↵    1024 point waveform    -    9652 bytes"
```

```
700 PRINT "J                2048 point waveform -        18796 bytes"
710 PRINT "JSystem initialization complete"
720 END
730 REM
740 REM -- Set up the shot
750 REM
760 PRINT "LI     CHANNEL ASSIGNMENTSJ"
770 J=0
780 FOR I=1 TO 6
790 Y$=SEG(Z$,10*I-9,21(I))
800 IF Y$<>"" THEN 820
810 Y$="<disabled>"
820 X$=CHR(65+J)
830 PRINT "JDigitizer ";INT((I+1)/2);" Channel ";X$;" --> ";Y$
840 IF NOT(J) THEN 860
850 PRINT
860 J=NOT(J)
870 NEXT I
880 PRINT "JJChange any of these? ";
890 INPUT X$
900 X$=SEG(X$,1,1)
910 IF X$="y" THEN 950
920 FIND 5
930 WRITE @33:Z$
940 GO TO 1170
950 PRINT "J  Enter the new name for the channel"
960 PRINT "J    or 'OFF' to disable the channel"
970 PRINT "J    or <RETURN> to keep the given name"
980 J=0
990 PRINT "IJ"
1000 FOR I=1 TO 6
1010 PRINT "IIJ --> --------RRRRRRRR";
1020 INPUT X$
1030 IF X$="" THEN 1090
1040 IF X$<>"OFF" THEN 1060
```

```
1050 X$=""
1060 I1=LEN(X$)
1070 Z$=REP(X$,10*I-9,I1)
1080 Z1(I)=I1
1090 IF NOT(J) THEN 1110
1100 PRINT
1110 J=NOT(J)
1120 NEXT I
1130 GO TO 760
1140 REM
1150 REM  -- Prompt for comment files & shot information --
1160 REM
1170 PRINT "⌐Do you wish to create a general comment file? ";
1180 INPUT X$
1190 X$=SEG(X$,1,1)
1200 IF X$="N" THEN 1220
1210 GOSUB 1370
1220 PRINT "⌐What is the shot number? ";
1230 INPUT S9
1240 S$=STR(S9)
1250 S$="SHOT"&S$
1260 S$=REP("",5,1)
1270 PRINT "⌐Any comments specific to this shot? ";
1280 INPUT X$
1290 X$=SEG(X$,1,1)
1300 IF X$="N" THEN 1320
1310 GOSUB 1630
1320 PRINT "⌐Setup complete"
1330 RETURN
1340 REM
1350 REM  -- Subroutine to create GENERAL comment file
1360 REM
1370 CALL "TIME",X$
1380 X$=REP("",10,9)
1390 X$=REP("",3,1)
```

```
1400 X$=REP("",6,1)
1410 X$=REP("CMT",1,0)
1420 U$=X$&"."
1430 PRINT "JThe file '";X$;"' will be created for comments."
1440 PRINT "JEnter an additional 4 character identifier for this"
1450 PRINT "comment file -->    ----HHHH";
1460 INPUT Y$
1470 X$=U$&Y$
1480 CALL "FILE",0,X$,Y$
1490 IF Y$="" THEN 1550
1500 PRINT "JFile '";X$;"' already exists . . . overwrite? ";
1510 INPUT Y$
1520 Y$=SEG(Y$,1,1)
1530 IF Y$="N" THEN 1440
1540 KILL X$
1550 GOSUB 1728
1560 PAGE
1570 GOSUB 2490
1580 CLOSE 2
1590 RETURN
1600 REM
1610 REM -- Subroutine to create SHOT comment file
1620 REM
1630 PRINT "LThe file ";S$;"/COMMENTS will be created"
1640 X$=S$&"/COMMENTS"
1650 GOSUB 1720
1660 GOSUB 2490
1670 CLOSE 2
1680 RETURN
1690 REM
1700 REM -- Subroutine to initialize random file X$
1710 REM
1720 CREATE X$,"B";25,75
1730 OPEN X$;2,"F",Y$
1740 FOR I=1 TO 25
```

```
1750 WRITE #2,I:I$
1760 NEXT I
1770 RETURN
1780 REM
1790 REM  -- Directory of disk --
1800 REM
1810 PRINT "LJI     DIRECTORY OF DISKJJ"
1820 DIRECTORY 0,"@SCRATCHLIB#"
1830 RETURN
1840 REM
1850 REM  -- Subroutine to store waveform & header information
1860 REM
1870 REM  U=digitizer number   C$=digitizer channel
1880 REM
1890 Q$=S$&"#"
1900 CALL "FILE",0,Q$,X$
1910 I1=POS(X$,"COMMENTS",1)
1920 I2=POS(X$,"/",I1)
1930 IF I2=0 THEN 1970
1940 PRINT "J";S$;" has already been acquired"
1950 PRINT "JPlease use function key 1 to define another shot number"
1960 RETURN
1970 PRINT "LI     Acquiring shot data from 7612's JJ"
1980 Q$=S$&"/"
1990 I8=0
2000 FOR I9=1 TO 6
2010 IF Z1(I9)=0 THEN 2120
2020 C$=CHR(65+I8)
2030 U=INT((I9+1)/2)
2040 GOSUB 4950
2050 X$=SEG(Z$,10*I9-9,Z1(I9))
2060 Y$=Q$&X$
2070 CREATE Y$,"BS";I9*A1+200,0
2080 OPEN Y$;1,"F",X$
2090 PRINT "JStoring Digitizer ";U;" Channel ";C$;" in file ";Y$
```

```
2100 WRITE #1:U,C$,A$,A1,A2,A3,A4,A5,H$,U$,A,B1,B
2110 CLOSE 1
2120 I8=NOT(I8)
2130 NEXT I9
2140 PRINT "⌐Shot data has been stored"
2150 RETURN
2160 REM
2170 REM -- Recall a waveform from disk
2180 REM
2190 PRINT "⌐⌐ AVAILABLE SHOT DATA FILES⌐⌐"
2200 CALL "FILE",0,"SHOT*#",X$
2210 I1=1
2220 I2=POS(X$,"SHOT",I1)
2230 IF I2=0 THEN 2310
2240 Y$=SEG(X$,I2,21)
2250 I3=POS(Y$,J$,1)
2260 IF I3=0 THEN 2280
2270 Y$=SEG(Y$,1,I3-1)
2280 PRINT Y$
2290 I1=I2+1
2300 GO TO 2220
2310 PRINT "⌐Which file do you wish to recall? ";
2320 INPUT X$
2330 CALL "file",0,X$,Y$
2340 IF Y$<>"" THEN 2370
2350 PRINT "⌐File ";X$;" not found"
2360 GO TO 2310
2370 OPEN X$,"G";1,"R",Y$
2380 PRINT "⌐Reading waveform into memory . . ."
2390 READ #1:U,C$,A$,A1,A2,A3,A4,A5,H$,U$
2400 DELETE A,B
2410 DIM A(A1)
2420 READ #1:A,B1
2430 DIM B(B1,2)
2440 READ #1:B
```

```
2450 CLOSE
2460 L$=X$
2470 PRINT "↓Complete"
2480 RETURN
2490 REM -- Subroutine to input comments
2500 K$=""
2510 PRINT "↓Enter up to 25 lines of comments↓"
2520 I=1
2530 PRINT USING "2D,2A,S":I," "
2540 INPUT X$
2550 IF X$="" THEN 2590
2560 WRITE #2,I:X$
2570 I=I+1
2580 IF I<=25 THEN 2530
2590 RETURN
2600 REM
2610 REM -- Subroutine to print comment file
2620 REM
2630 CALL "FILE",0,"CMT*.*",X$
2640 PRINT "↓↓↓         AVAILABLE COMMENT FILES↓↓"
2650 I1=1
2660 I2=POS(X$,"/",I1)+1
2670 IF I2=1 THEN 2750
2680 Y$=SEG(X$,I2,15)
2690 I3=POS(Y$,J$,1)
2700 IF I3=0 THEN 2720
2710 Y$=SEG(Y$,1,I3-1)
2720 PRINT Y$
2730 I1=I2
2740 GO TO 2660
2750 CALL "FILE",0,"*/COMMENTS",X$
2760 I1=1
2770 I2=POS(X$,"/",I1)+1
2780 IF I2=1 THEN 2860
2790 Y$=SEG(X$,I2,21)
```

```
2800 I3=POS(Y$,J$,1)
2810 IF I3=0 THEN 2830
2820 Y$=SEG(Y$,1,I3-1)
2830 PRINT Y$
2840 I1=I2+11
2850 GO TO 2770
2860 PRINT "JEnter the name of the file you wish to list -->";
2870 INPUT X$
2880 CALL "FILE",0,X$,Y$
2890 IF Y$<>"" THEN 2920
2900 PRINT "JFile ";X$;" not found"
2910 GO TO 2750
2920 OPEN X$;2, "R",Y$
2930 PRINT "LI    ";X$;"J"
2940 E9=0
2950 I1=1
2960 ON EOF (2) THEN 3040
2970 READ #2,I1:X$
2980 IF E9 THEN 3020
2990 PRINT X$
3000 I1=I1+1
3010 GO TO 2970
3020 CLOSE 2
3030 RETURN
3040 E9=1
3050 RETURN
3060 REM
3070 REM  -- Subroutine to select segment of waveform
3080 REM
3090 IF A1>0 THEN 3120
3100 PRINT "Sorry --- No data acquired.  Press key 2 or 9 first."
3110 GO TO 3490
3120 IF F(4)=0 THEN 3160
3130 X=INT(Q(K,2)/2048)
3140 J=Q(K,2)-X*2048
```

```
3150 GO TO 3300
3160 PRINT "J        RECORD PROFILE FOR CHANNEL ";C$;" DATA"
3170 PRINT "JSTART SAMPLE","SAMPLING INTERVAL"
3180 FOR I=1 TO B1
3190 PRINT B(I,1),B(I,2)
3200 NEXT I
3210 PRINT A1-1,"LAST SAMPLE"
3220 PRINT "JEnter starting sample desired ";G$;
3230 INPUT X
3240 X=INT(X)
3250 IF X<0 OR X>A1-1 THEN 3220
3260 PRINT "JNow enter ending sample desired (";X;"--";A1-1;")";G$;
3270 INPUT J
3280 J=INT(J)
3290 IF J<=X OR J>A1-1 THEN 3260
3300 FOR I=1 TO B1
3310 IF X<B(I,1) THEN 3340
3320 A3=B(I,2)
3330 NEXT I
3340 DELETE B
3350 DIM B(J-X+1)
3360 FOR I=1 TO J-X+1
3370 B(I)=A(I+X)
3380 NEXT I
3390 DELETE A
3400 A1=J-X+1
3410 DIM A(A1)
3420 A=B
3430 DELETE B
3440 B1=1
3450 DIM B(B1,2)
3460 B(1,1)=0
3470 B(1,2)=A3
3480 A2=0
3490 VIEWPORT 15,120,10,90
```

```
3500 PRINT "L ","SELECTED SEGMENT"
3510 GOSUB 5470
3520 RETURN
3530 REM
3540 REM -- Pulse parameters from min and max
3550 REM
3560 IF A1>1 THEN 3590
3570 PRINT "Sorry --- No data acquired. Press key 2 or 9 first."
3580 GO TO 3730
3590 VIEWPORT 15,120,50,90
3600 GOSUB 5500
3610 CALL "MIN",A,M1,M3
3620 CALL "MAX",A,M5,M3
3630 GOSUB 6490
3640 RETURN
3650 REM
3660 REM -- Pulse parameters from histogram
3670 REM
3680 IF A1>1 THEN 3710
3690 PRINT "Sorry --- No data acquired. Press key 2 or 9 first."
3700 GO TO 4230
3710 VIEWPORT 15,90,50,90
3720 GOSUB 5500
3730 DELETE H
3740 DIM H(256)
3750 CALL "MIN",A,M1,M3
3760 CALL "MAX",A,M5,M3
3770 X=255/(M5-M1)
3780 REM Build histogram
3790 H=0
3800 FOR I=1 TO A1
3810 J=(A(I)-M1)*X+1
3820 H(J)=H(J)+1
3830 NEXT I
3840 VIEWPORT 95,130,50,90
```

```
3850 CALL "MAX",H,M2,M4
3860 WINDOW 0,M2,M3,M4
3870 MOVE H(1),M1
3880 FOR I=2 TO 256
3890 DRAW H(I),(I-1)/X+M1
3900 NEXT I
3910 REM Find mean, and negate first half
3920 I=(SUM(A)/A1-M1)*X+1
3930 MOVE 0,(I-1)/X+M1
3940 PRINT "------------";
3950 FOR J=1 TO I
3960 H(J)=-H(J)
3970 NEXT J
3980 REM Now MIN(H)==> 0%; & MAX(H)==>100%
3990 CALL "MIN",H,I,I
4000 CALL "MAX",H,J,J
4010 DELETE H
4020 M1=(I-1)/X+M1
4030 M5=(J-1)/X+M1
4040 VIEWPORT 15,90,50,90
4050 WINDOW 1,A1,M3,M4
4060 GOSUB 6490
4070 RETURN
4080 REM
4090 REM -- Integrate the waveform
4100 REM
4110 GOSUB 6290
4120 IF F0=0 THEN 4170
4130 CALL "INT",A,A
4140 A=A/A3
4150 VIEWPORT 15,128,10,90
4160 GOSUB 5470
4170 RETURN
4180 REM
4190 REM -- Differentiate the waveform
```

```
4200 REM
4210 GOSUB 6290
4220 IF F0=0 THEN 4350
4230 IF F(4)=0 THEN 4260
4240 X=Q(K,2)
4250 GO TO 4290
4260 PRINT "JDo you wish 2-point or 3-point differentiation (2/3) ?";G$;
4270 INPUT X
4280 X=INT(X)
4290 IF X<>2 AND X<>3 THEN 4260
4300 A$=SEG("DIF2DIF3",(X-2)*4+1,4)
4310 CALL A$,A,A
4320 A=A*A3
4330 VIEWPORT 15,120,10,80
4340 GOSUB 5470
4350 RETURN
4360 REM
4370 REM -- Apply x% cosine taper
4380 REM
4390 GOSUB 6290
4400 IF F0=0 THEN 4820
4410 GOSUB 6410
4420 IF F0=0 THEN 4820
4430 IF F(4)=0 THEN 4460
4440 X=Q(K,2)
4450 GO TO 4480
4460 PRINT "JEnter desired percentage of taper (0--50) ";G$;
4470 INPUT X
4480 IF X<0 OR X>50 THEN 4460
4490 X=X/100
4500 CALL "TAPER",A,X
4510 VIEWPORT 15,120,10,80
4520 F(9)=0
4530 RETURN
4540 REM
```

```
4550 REM -- Do FFT on waveform
4560 REM
4570 F(9)=17
4580 GOSUB 6070
4590 IF F0=0 THEN 5050
4600 REM -- now we can FFT
4610 CALL "FFT",A
4620 DELETE B,E
4630 DIM B(A1/2+1),E(A1/2+1)
4640 CALL "POLAR",A,B,E
4650 DELETE A,E
4660 DIM A(A1/2+1)
4670 A1=A1/2+1
4680 A=B
4690 DELETE E
4700 H$="Hz"
4710 U$="db"&U$
4720 A=LGT(A)
4730 A=20*A
4740 A2=0
4750 A3=1/(2*A3)/A1
4760 DIM B(1,2)
4770 B(1,1)=0
4780 B(1,2)=A3
4790 VIEWPORT 15,120,10,90
4800 GOSUB 5470
4810 F(9)=0
4820 RETURN
4830 REM
4840 REM -- Query User Routine
4850 REM
4860 PRINT B$;G$;
4870 INPUT A$
4880 A$=SEG(A$,1,1)
4890 X=0
```

```
4900 IF A$="N" THEN 4930
4910 IF A$<>"Y" THEN 4860
4920 X=1
4930 RETURN
4940 REM
4950 REM -- Subroutine to read record from channel C$
4960 REM
4970 IF A1=0 THEN 5070
4980 DELETE C,D
4990 C1=0
5000 IF A1>1024 THEN 5060
5010 DIM C(A1),D(B1,2)
5020 C1=A1
5030 C=A
5040 D1=B1
5050 D=B
5060 DELETE A,B
5070 PRINT @U,8:"TMBS ";C$;";REC?"
5080 INPUT @U,8:A2,A1
5090 IF A2=1 THEN 5190
5100 IF F(4)=0 THEN 5130
5110 X=Q(K,2)
5120 GO TO 5160
5130 PRINT "JEnter record number desired (1--";A2;")";"G$;
5140 INPUT X
5150 X=INT(X)
5160 IF X<1 OR X>A2 THEN 5130
5170 A2=X
5180 PRINT @U,8:"READ ";C$;",";A2-1
5190 DIM A(A1)
5200 WBYTE @64+U,96:
5210 RBYTE X,I1,I2,A,I,X
5220 J=SUM(A)+I1+I2+I
5230 IF J-256*INT(J/256)=0 THEN 5250
5240 PRINT "JChecksum error";I;J-256*INT(J/256)
```

```
5250 PRINT @U,0:"NBPT?"
5260 INPUT @U,0:B1
5270 DIM B(B1,2)
5280 PRINT @U,0:"SBPT?"
5290 INPUT @U,0:B
5300 A2=0
5310 A3=B(1,2)
5320 A4=0
5330 A5=1
5340 H$="S"
5350 U$="U"
5360 IF C$="B" THEN 5390
5370 PRINT @U,0:"USLI?"
5380 GO TO 5400
5390 PRINT @U,0:"USR1?"
5400 INPUT @U,0:A$
5410 A$=SEG(A$,6,LEN(A$))
5420 X=VAL(A$)/32
5430 A=A-128
5440 A=A*X
5450 RETURN
5460 REM
5470 REM -- Graph the waveform
5480 REM
5490 VIEWPORT 15,120,10,80
5500 PAGE
5510 W1=0
5520 J=A1
5530 GOSUB 5950
5540 W2=T
5550 CALL  "MIN",A,W3,X
5560 CALL  "MAX",A,W4,X
5570 REM -- Round W3 down to 2 digits
5580 IF W3=0 THEN 5610
5590 X=INT(LGT(ABS(W3)))
```

```
5600 W3=INT(W3/10↑(X-1))*10↑(X-1)
5610 REM
5620 W4=(W4-W3)/8
5630 X=INT(LGT(W4))
5640 W4=(INT(W4/10↑X)+1)*10↑X
5650 W4=W3+9*W4
5660 WINDOW 1,A1,W3,W4
5670 AXIS A1/10,(W4-W3)/9,1,W3
5680 X=INT(LGT(W2-W1))
5690 FOR J=0 TO A1 STEP A1/10
5700 GOSUB 5950
5710 MOVE J,W3
5720 PRINT USING """BBJ""",2D.2D";(T+A2)/10↑X
5730 NEXT J
5740 MOVE A1/2,W3
5750 PRINT "JBBB";
5760 IF X=0 THEN 5780
5770 PRINT 10↑X;
5780 PRINT "  ";H$;" ";A1;" Samples";
5790 REM -- Print vertical labels
5800 X=INT(LGT(W4-W3))
5810 FOR I=W3/10↑X TO W4/10↑X STEP (W4-W3)/10↑X/8
5820 MOVE W1,I*10↑X
5830 PRINT USING """BBBBBBBB""",6D.D,S";I;
5840 NEXT I
5850 MOVE W1,W4
5860 PRINT "BBBBBBKK";
5870 IF X=0 THEN 5890
5880 PRINT 10↑X;
5890 PRINT "  ";U$;
5900 WINDOW 1,A1,W3,W4
5910 CALL "DISP",A
5920 PRINT "IJJI        ";L$
5930 RETURN
5940 REM
```

```
5950 REM -- Subroutine to convert index J to time T
5960 REM
5970 T=0
5980 I=2
5990 IF B1=1 THEN 6040
6000 FOR I=2 TO B1
6010 IF B(I,1)>J THEN 6040
6020 T=T+(B(I,1)-B(I-1,1))*B(I-1,2)
6030 NEXT I
6040 T=T+(J-B(I-1,1))*B(I-1,2)
6050 RETURN
6060 REM
6070 REM -- Check for 1 segment record with power of two length
6080 REM
6090 F0=0
6100 IF A1>0 THEN 6130
6110 PRINT "JSorry --- No data acquired.  Press key 2 or 9 first."
6120 GO TO 6270
6130 X=LOG(A1)/LOG(2)
6140 IF X=INT(X) THEN 6170
6150 PRINT "JSorry --- Record must be a power of two."
6160 GO TO 6270
6170 IF B1=1 THEN 6200
6180 PRINT "JSorry --- Record must have uniform sampling rate."
6190 GO TO 6270
6200 IF A1(=512+(F(9)=17)*512 THEN 6230
6210 PRINT "JSorry --- Waveform length limited to ";512+(F(9)=17)*512
6220 GO TO 6270
6230 IF F(9)=1 THEN 6260
6240 PRINT "JSorry --- 405*R08 require for this function."
6250 GO TO 6270
6260 F0=1
6270 RETURN
6280 REM
6290 REM -- Check for 1 segment record
```

```
6300 REM
6310 F0=0
6320 IF A1>0 THEN 6350
6330 PRINT "JSorry --- No data acquied.  Press key 2 or 9 first."
6340 GO TO 6390
6350 IF B1=1 THEN 6380
6360 PRINT "JSorry --- Record must have uniform sampling rate."
6370 GO TO 6390
6380 F0=1
6390 RETURN
6400 REM
6410 REM  -- Check for R08
6420 REM
6430 X=1
6440 IF F(8)=1 THEN 6470
6450 PRINT "JSorry --- 405xR08 required for this function."
6460 X=0
6470 RETURN
6480 REM
6490 REM  -- Do pulse parameters
6500 REM
6510 M6=M5-M1
6520 M2=M6*0.1+M1
6530 M3=M6*0.5+M1
6540 M4=M6*0.9+M1
6550 MOVE 1,M1
6560 GOSUB 6900
6570 MOVE 1,M2
6580 GOSUB 6900
6590 MOVE 1,M3
6600 GOSUB 6900
6610 MOVE 1,M4
6620 GOSUB 6900
6630 MOVE 1,M5
6640 GOSUB 6900
```

```
6650 CALL "CROSS",A,M2,J,1
6660 GOSUB 5950
6670 T1=T
6680 CALL "CROSS",A,M3,J,1
6690 GOSUB 5950
6700 T2=T
6710 CALL "CROSS",A,M4,J,1
6720 GOSUB 5950
6730 T3=T
6740 CALL "CROSS",A,M4,J,2
6750 GOSUB 5950
6760 T4=T
6770 CALL "CROSS",A,M3,J,2
6780 GOSUB 5950
6790 T5=T
6800 CALL "CROSS",A,M2,J,2
6810 GOSUB 5950
6820 T6=T
6830 PRINT @32,21:0,40
6840 PRINT "Rise time      ";T3-T1,"Slew rate     ";(M2-M1)*0.8/(T3-T1)
6850 PRINT "Fall time      ";T6-T4,"Slew rate     ";(M2-M1)*0.8/(T6-T4)
6860 PRINT "Pulse width    ";T5-T2
6870 PRINT "MAXIMUM  ";M5
6880 PRINT "MINIMUM  ";M1
6890 GO TO 3640
6900 FOR I=1 TO 21+(F(9)=6)*8
6910 PRINT " -";
6920 NEXT I
6930 RETURN
6940 REM
6950 REM  -- Subroutine to plot multiple waveforms on same screen
6960 REM
6970 Y$=S$&"#"
6980 Q$=S$&"/COMMENTS"
6990 CALL "FILE",0,Y$,X$
```

```
7000 PRINT "LI                    ";S$;
7010 U1=1
7020 U2=0
7030 I1=1
7040 I2=POS(X$,S$,I1)
7050 Y$=SEG(X$,I2,21)
7060 IF I2=0 THEN 7540
7070 I3=POS(Y$,J$,1)
7080 IF I3=0 THEN 7140
7090 Y$=SEG(Y$,1,I3-1)
7100 I1=I2+1
7110 REM
7120 REM -- Read a waveform from disk
7130 REM
7140 IF Y$=Q$ THEN 7040
7150 OPEN Y$;1,"R",Q$
7160 READ #1:U,C$,A$,A1,A2,A3,A4,A5,H$,V$
7170 DELETE A,B
7180 DIM A(A1)
7190 READ #1:A,B1
7200 DIM B(B1,2)
7210 READ #1:B
7220 CLOSE
7230 CALL "MIN",A,W3,X
7240 CALL "MAX",A,W4,X
7250 IF W3=0 THEN 7290
7260 X=INT(LGT(ABS(W3)))
7270 W3=INT(W3/10↑(X-1))*10↑(X-1)
7280 W4=(W4-W3)/9
7290 X=INT(LGT(W4))
7300 W4=(INT(W4/10↑X)+1)*10↑X
7310 W4=W3+8*W4
7320 V3=32*(4-INT((U1+1)/2))-28
7330 U4=10+70*U2
7340 VIEWPORT U4,U4+50,V3,V3+28
```

```
7350 PRINT @32,21:U4+14,U3-4
7360 L$=Y$
7370 Y$=REP("=",1,LEN(S$)+1)
7380 PRINT Y$;
7390 WINDOW 1,A1,W3,W4
7400 AXIS A1/10,(W4-W3)/8,1,W3
7410 CALL "DISP",A
7420 PRINT @32,21:U4-10,U3+25
7430 PRINT USING "2D.2D,S":(W4-W3)/8
7440 PRINT "HHHJ";U$;"/D";
7441 I=VAL(A$)
7442 I=ABS(I)
7443 J=POS(A$,".",1)
7444 A$=SEG(A$,J+1,4)
7445 J=POS(A$,".",1)
7446 A$=SEG(A$,1,J-1)
7447 PRINT @32,21:U4+2,U3+22
7448 PRINT USING "2D.3D,3A,S":I,A$
7449 PRINT @32,21:U4-10,U3+15
7450 PRINT "HHHJ";A$;"/D";
7460 E9=A1*A3/10
7470 GOSUB 7580
7480 PRINT @32,21:U4-10,U3+6
7490 PRINT USING "4D.D,S":E2*E3
7500 PRINT "HHHJ";A$;"S/D"
7510 U1=U1+1
7520 U2=NOT(U2)
7530 GO TO 7040
7540 RETURN
7550 REM
7560 REM -- Subroutine to convert number to engineering notation
7570 REM
7580 IF E9<>0 THEN 7630
7590 E2=0
7600 E3=0
7610 A$=" "
```

```
7620 RETURN
7630 E1=ABS(INT(LGT(E9)))
7640 A$=SEG("mmmuuunnn",E1,1)
7650 E2=E9*10↑E1
7660 E1=E1-6*(E1>6)
7670 E1=E1-3*(E1>3)
7680 E3=10↑(3-E1)
7690 RETURN
7700 REM
7710 REM  -- Subroutine to handle service requests (SRQ's)
7720 REM
7730 REM     Non-programable plugins are assumed
7740 REM     All three digitizers must be powered on
7750 REM
7760 POLL H1,H2;1,0;2,0;3,0
7770 PRINT "_SRQ From Device ";H1;" Status byte = ";H2
7780 RETURN
7790 REM ARM ALL CHANNELS
7800 PRINT @1,0:"ARM A,B"
7810 PRINT @2,0:"ARM A,B"
7820 PRINT @3,0:"ARM A,B"
7830 PRINT "Specified channels are now armed and ready for the shot..."
7940 RETURN
7850 REM THIS MODIFICATION OF THE ORIGINAL PROGRAM
7860 REM STORES THE MAINFRAME SETTINGS OF THE 7612D ON FILE 6.
7870 REM IT SETS THE 7612D MAINFRAME USING FILE 6 DATA.
7880 REM NEW LINES ARE: 48,49,8050-8320,210
7890 PRINT "LTO STORE 7612D MAINFRAME SETTINGS PRESS <S>"
7900 PRINT "JTO RESTORE 7612D MAINFRAME SETTINGS PRESS <R>"
7910 INPUT D$
7920 IF D$="S" THEN 7950
7930 IF D$="R" THEN 8050
7940 GO TO 7890
7950 FIND 6
7960 PRINT "LI*** STORING MAINFRAME SETTINGS ***"
```

```
7970 FOR A6=1 TO 3
7980 REM A6=MAINFRAME ADDRESS
7990 PRINT @A6,0:"SET?"
8000 INPUT @A6,0:D$
8010 WRITE @33:D$
8020 NEXT A6
8030 CLOSE
8040 GO TO 8120
8050 PRINT "LI**** RESTORING MAINFRAME SETTINGS ****"
8060 FIND 6
8070 FOR A6=1 TO 3
8080 READ @33:D$
8090 PRINT @A6,0:"TMBS A;CBPT;TMBS B;CBPT;"
8100 PRINT @A6,0:D$
8110 NEXT A6
8120 PRINT "IJGG                  **** DONE ****"
8130 RETURN
9000 FIND 8
9010 CALL "BAPPEN",10000
9020 GOSUB 10000
9030 END
10000 REM ****ANALYSIS OVERLAY GOES HERE******
```

FIND5
READ@33:2$

2$
Coo12o24p4Goo33o22p7Eoo1Bo55p5Goo33o22p7Koo28o1Bpf

FIND6
READ@33:D$

D$
CLK INT;BTA OFF;WRI OFF;RQS ON;REM OFF;TMBS A;REC 1,512;SBPT 0,1E-8;MODE
PRE,56;LTC LEFT;SRC EXT;SLO POS;HFR OFF;CPL AC;LEV 20;TMBS B;REC 1,256;
SBPT 0,1E-1;MODE PRE,56;LTC LEFT;SRC EXT;SLO POS;HFR OFF;CPL AC;LEV 20;

```
FIND?
OLD

LIST
10000 PRINT "LJJJ          *** ENERGY REDUCTION   ***"
10010 PRINT " LJJ              INPUT OPTION                 :"
10020 PRINT " LJJJ        REDUCE A SINGLE CHANNEL <S>       "
10030 PRINT " LJJREDUCE ALL CHANNELS FROM A SHOT <M>"
10040 PRINT " LJ LIST CONTENT OF ENERGY FILE <L>"
10050 INPUT D$
10060 IF D$="S" THEN 10100
10070 IF D$="L" THEN 10910
10080 IF D$="M" THEN 10120
10090 GO TO 10000
10100 GOSUB 10140
10110 GO TO 10000
10120 GOSUB 11530
10130 GO TO 10000
10140 REM ------ single channel reduction
10150 PRINT "LJJG THIS REDUCTION SCHEME ASSUMES A FILE OF THE FORM:"
10160 PRINT "JI AXM12345p6"
10170 PRINT "J WHERE        A is the detector designation"
10180 PRINT "J        X stands for the letter L or P or B where:"
10190 PRINT "J        L is a light calorimeter (with glass) "
10200 PRINT "J        P is a particle calorimeter (no glass) "
10210 PRINT "J        B is P and L hooked up in parralel (subtr.)"
10220 PRINT "J        M means minus (if applicable)"
10230 PRINT "J        12 is the angular location of detector"
10240 PRINT "J            with respect to the laser beam (deg)"
10250 PRINT "J        345p6 is 345.6 the calibration factor(J/sru)"
10260 PRINT "JJ PRESS <RETURN> TO GO ON"
10270 INPUT D$
```

```
10280  IF D$="" THEN 10300
10290  GO TO 10150
10300  REM ------- get the trace and graph it
10310  GOSUB 2090
10320  VIEWPORT 15,120,50,90
10330  GOSUB 5420
10340  WINDOW 1,A1,W3,W4
10350  CALL "MIN",A,M1,M3
10360  CALL "MAX",A,M5,M3
10370  MOVE 1,M1
10380  GOSUB 6820
10390  MOVE 1,M5
10400  GOSUB 6820
10410  M6=M5-M1
10420  PRINT @32,21:0,48
10430  PRINT "PULSE HEIGHT (volts)  ";M6
10440  REM ------ find detector location from channel name
10450  M1=POS(L$,"/",1)
10460  L$=REP(".",M1+9,1)
10470  D$=SEG(L$,M1+6,5)
10480  REM------ M3 is the calibration factor of the detector
10490  M3=VAL(D$)
10500  D$=SEG(L$,M1+3,3)
10510  M5=VAL(D$)
10520  D$=SEG(D$,1,1)
10530  IF D$="M" THEN 10550
10540  GO TO 10560
10550  M5=-M5
10560  REM-------- M5 is the angular detector location
10570  Y$=SEG(L$,M1+2,1)
10580  REM
10590  PRINT  "DETECTOR ANGLE(deg)   ";M5
10600  PRINT  "CALIBRATION FACT.(J/sr) ";M3
10610  PRINT  "ENERGY(J/sr)    ";M6*M3
10620  PRINT  "DETECTOR TYPE    ";Y$
```

```
10630 PRINT @32,21:0,40
10640 PRINT "I
10650 PRINT "I J
10660 PRINT "I
10670 PRINT "I
10680 PRINT "I
10690 REM
10700 REM
10710 INPUT D$
10720 IF D$="S" THEN 10820
10730 IF D$="B" THEN 10760
10740 IF D$="M" THEN 10780
10750 IF D$="I" THEN 10800
10760 GOSUB 11240
10770 GO TO 10330
10780 GOSUB 11340
10790 GO TO 10370
10800 RETURN
10810 PAGE
10820 I=POS(X$,"/",1)
10830 X$=REP("ENERGY",I+1,10)
10840 CALL "FILE",0,X$,D$
10850 IF D$<>"" THEN 10870
10860 CREATE X$,"UM";256,0
10870 OPEN X$;1,"U",D$
10880 WRITE #1:M5,M3,M6,M6*M3,Y$,"from digitizer"
10890 CLOSE 1
10900 RETURN
10910 REM
10920 REM----- list the content of file containing reduced energies
10930 PAGE
10940 DIRECTORY 0,"@SCRATCHLIB/*/ENERGY"
10950 PRINT "Which SHOT do you want to recall ?"
10960 INPUT D$
10970 D$="SHOT"&D$
```

Screen output text (from PRINT statements):

```
PICK ONE OPTION GG
STORE THIS RESULT      <S>
REMOVE BASELINE DRIFT<B> :
REDUCE MANUALLY       <M> :
IGNORE AND RETURN     <I>"
```
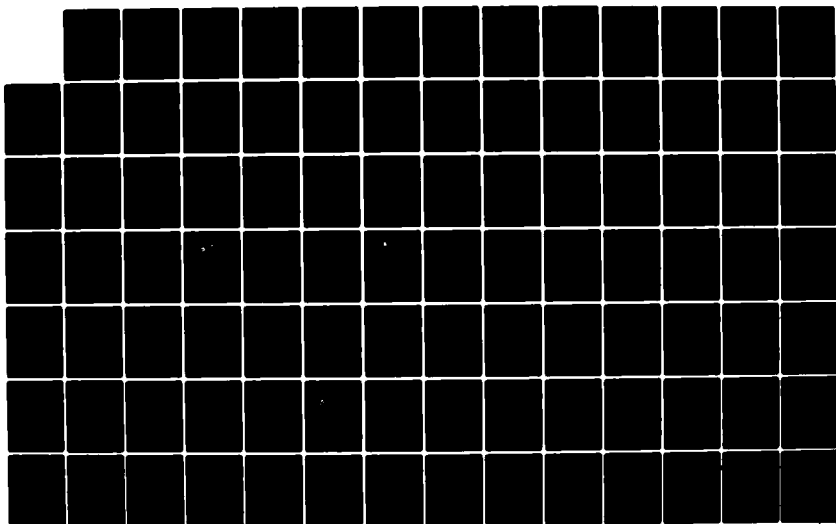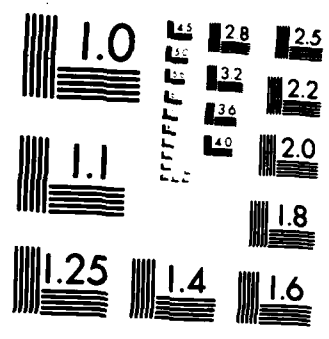
MICROCOPY RESOLUTION TEST CHART

NATIONAL BUREAU OF STANDARDS 1963 A

```
10980 D$=D$&"/ENERGY"
10990 DIM A7(4,40)
11000 OPEN D$;1,"R",D$
11010 CALL "REWIND",1
11020 ON EOF (1) THEN 11190
11030 PRINT "LJANGLE(deg)    CAL(J/srV)    VOLTAGE    ENERGY(J/sr)    TYPEJ"
11040 FOR J=1 TO 40
11050 FOR I=1 TO 4
11060 READ #1:A7(I,J)
11070 NEXT I
11080 READ #1:Y$
11090 READ #1:D$
11100 PRINT USING 11110:A7(1,J),A7(2,J),A7(3,J),A7(4,J),Y$,D$
11110 IMAGE 3D.1D,8X,4D.1D,7X,3D.3D,5X,4D.1D,9X,A,3X,15A
11120 NEXT J
11130 PRINT "THERE IS MORE DATA IN THE FILE--ALTER LINES 10990,11040 ."
11140 PRINT "JJpress <RETURN> to go on"
11150 INPUT D$
11160 CLOSE 1
11170 GO TO 10000
11180 REM
11190 PRINT "JJTHIS FILE CONTAINS  ";J-1;" DATA POINT(S)"
11200 PRINT "JJPRESS <RETURN> TO GO ON"
11210 INPUT D$
11220 CLOSE 1
11230 GO TO 10000
11240 REM ----- subroutine to subtract baseline drift
11250 PRINT "IG                      input LEFT then RIGHT baseline pt."
11260 POINTER M5,M3,D$
11270 PRINT "G"
11280 POINTER M1,M6,D$
11290 PRINT "G"
11300 FOR I=1 TO A1
11310 A(I)=A(I)-I*((M6-M3)/(M1-M5))
11320 NEXT I
```

```
11330 RETURN
11340 REM
11350 REM
11360 REM ----- manual definition of MAX and MIN points
11370 PAGE
11380 PRINT "Juse joystick to define the MIN and MAX points."
11390 PRINT "JJJJdefine the MIN point FIRST;"
11400 PRINT "JJthen define the MAX point"
11410 PRINT "JJJJPRESS <RETURN> TO CONTINUE"
11420 INPUT D$
11430 PAGE
11440 REM ----- graph the trace
11450 VIEWPORT 15,120,50,98
11460 GOSUB 5420
11470 WINDOW 1,A1,W3,W4
11480 POINTER M3,M1,D$
11490 PRINT "G"
11500 POINTER M3,M5,D$
11510 PRINT "G"
11520 RETURN
11530 REM ----- subroutine to reduce all channels of a shot
11540 PAGE
11550 DIRECTORY 0,"SHOT*/??????P?"
11560 PRINT "JGJpick the SHOT NUMBER to be reduced"
11570 INPUT D$
11580 PRINT "GJJprint the unit designations. ex. ABDEF... (no spaces)"
11590 INPUT W$
11600 W5=LEN(W$)
11610 T$="SHOT"&D$
11620 T$=T$&"/"
11630 FOR W6=1 TO W5
11640 X$=SEG(W$,W6,1)
11650 X$=T$&X$
11660 X$=X$&"??????P?"
11670 DELETE Y$
```

```
11680 DIM Y$(600)
11690 GOSUB 2250
11700 I=LEN(X$)
11710 X$=SEG(X$,1,I-9)
11720 J=POS(Y$,X$,1)
11730 L$=SEG(Y$,J,I)
11740 DELETE Y$
11750 X$=L$
11760 GOSUB 10320
11770 NEXT W6
11780 RETURN
```

FILE 8 IS THE BINARY VERSION OF FILE 7

APPENDIX H

```
50 REM THIS PROGRAM CALCULATES THE ENERGY CONTENT OF A FOCAL SPOT
52 REM
60 INIT
100 REMARK GENERATE 4 CYCLE SEMILOG SHEET
110 PAGE
120 VIEWPORT 3,66,10,100
130 WINDOW 0,70,-0.05,4
140 AXIS 10,0,0,0
150 FOR I=2 TO 70 STEP 2
160 MOVE I,0
170 RDRAW 0,4
180 NEXT I
190 I=1
200 J=1
210 I=I+J
220 IF I>10000 THEN 280
230 AXIS 0,0,0,LGT(I)
240 IF I=10 OR I=100 OR I=1000 THEN 260
250 GO TO 210
260 J=I
270 GO TO 210
280 REMARK END OF 4 CYCLE SEMILOG GENERATION
285 REM
290 REM SCALING OF VERTICAL AXIS
295 REM
300 REM DEFINE MIRROR TRANSMISSION BELOW
318 R1=0.4
315 REM
320 HOME
330 PRINT " "," ","GGG          ";"SHOT NUMBER IS ";
331 INPUT D$
340 PRINT USING 345:R1
345 IMAGE//45X,"TRANSM/PASS R1R2 = ",1D.2D
360 R2=R1
```

```
370 MOVE 0,LGT(1/R2)
380 FOR I=1 TO 25
390 RDRAW 1,0
400 RMOVE 2,0
410 NEXT I
420 R2=R2*R1
430 IF LGT(1/R2)>4 THEN 450
440 GO TO 370
450 REM END VERTICAL SCALING
460 REM
470 REM USER RESCALES HORIZONTAL AXIS
487 FOR I=1 TO 2
488 MOVE 54,-0.05
489 PRINT "JJ";
490 PRINT "RADIUS(UM)","GGG"
500 NEXT I
510 MOVE 68,-0.05
520 PRINT "J";
530 INPUT R
540 WINDOW 0,R,-0.05,4
550 FOR J=1 TO 6
560 MOVE R/7*R*J,-0.05
561 A9=1/7*R*J
562 A$=STR(A9)
563 A$=SEG(A$,1,5)
564 RMOVE -R/20,0
570 PRINT "J";
575 PRINT A$
580 NEXT J
590 REM END OF HORIZONTAL SCALING
595 REM
600 REM DATA ENTRY
610 HOME
620 PRINT USING 621:"SPOT DATA","(I=IN,L=LAST)"
621 IMAGE ////,50X,9A,/,50X,13A
```

```
650 DIM P(301),E(301)
651 P=0
652 E=0
660 FOR J=1 TO 301 STEP 10
670 POINTER P(J),E(J),C$
680 IF J<>1 THEN 690
685 MOVE P(J),E(J)
686 DRAW P(J),E(J)
687 GO TO 700
690 MOVE P(J-10),E(J-10)
695 DRAW P(J),E(J)
696 IF C$="L" THEN 701
700 NEXT J
701 HOME
702 FOR I=1 TO J STEP 10
703 IF I=1 THEN 710
704 GO TO 715
705 IMAGE 8(/),50X,4D.1D
710 PRINT USING 705:P(I)
711 GO TO 720
715 PRINT USING 716:P(I)
716 IMAGE 50X,4D.1D
720 NEXT I
730 REM END DATA ENTRY
740 REM
750 REM INTERPOLATE BETWEEN ENTERED POINTS
760 FOR I=1 TO J-10 STEP 10
765 IF P(I+10)=P(I) THEN 820
770 T=ABS((E(I+10)-E(I))/(P(I+10)-P(I)))
775 X=ABS(P(I+10)-P(I))
780 IF E(I+10)=>E(I) AND P(I+10)>P(I) THEN 870
790 IF E(I+10)<E(I) AND P(I+10)>P(I) THEN 930
800 IF E(I+10)=>E(I) AND P(I+10)<P(I) THEN 990
810 IF E(I+10)<E(I) AND P(I+10)<P(I) THEN 1040
820 FOR I1=I+1 TO I+9
```

```
830 E(I1)=E(I)
840 P(I1)=P(I)
850 NEXT I1
860 GO TO 1080
870 FOR I1=I+1 TO I+9
880 P(I1)=P(I)+(I1-I)*X/10
890 IF E(I+10)<>E(I) THEN 905
895 E(I1)=E(I)
900 GO TO 910
905 E(I1)=E(I)+(I1-I)*X*T/10
910 NEXT I1
920 GO TO 1080
930 FOR I1=I+1 TO I+9
940 P(I1)=P(I)+(I1-I)*X/10
950 E(I1)=E(I)-(I1-I)*X*T/10
960 NEXT I1
970 GO TO 1080
980 FOR I1=I+1 TO I+9
990 P(I1)=P(I)-(I1-I)*X/10
1000 IF E(I+10)<>E(I) THEN 1015
1005 E(I1)=E(I)
1010 GO TO 1020
1015 E(I1)=E(I)+(I1-I)*X*T/10
1020 NEXT I1
1030 GO TO 1080
1040 FOR I1=I+1 TO I+9
1050 P(I1)=P(I)-(I1-I)*X/10
1060 E(I1)=E(I)-(I1-I)*X*T/10
1070 NEXT I1
1080 NEXT I
1085 REM END OF INTERPOLATION
2000 REM THIS ROUTINE CALCULATES THE SUMS OF [(E(J))[P(J)^2-P(J-1)^2]]
2010 DIM S(301)
2011 S=0
2020 REM IF FIRST ENTERED POINT HAS P(1)<>0 THEN LABEL DATA
```

```
2030 REM IN PROPER SEQUENCE
2040 IF P(1)=>R/35 THEN 2120
2050 REM
2060 FOR I=2 TO J
2070 S(1)=0
2080 H=((10↑E(I)+10↑E(I-1))*(P(I)↑2-P(I-1)↑2)/2
2090 S(I)=S(I-1)+H
2100 NEXT I
2110 GO TO 2220
2120 DIM E1(301),P1(301)
2130 FOR I=1 TO J
2140 E1(J+1-I)=E(I)
2150 P1(J+1-I)=P(I)
2160 NEXT I
2170 FOR I=1 TO J
2180 E(I)=E1(I)
2190 P(I)=P1(I)
2200 NEXT I
2210 GO TO 2050
2220 REM END OF SUMMATION. FINAL SUM IS S(J)
2230 REM
2240 REM RESCALE PARTIAL SUMS
2250 FOR I=1 TO J
2260 S(I)=S(I)/S(J)
2270 NEXT I
2280 REM END OF RESCALING
2290 REM
2300 REM GRAPH ENERGY CONTENT
2310 FOR I=3 TO J
2320 MOVE P(I-1),LGT(S(I-1)*10)
2330 DRAW P(I),LGT(S(I)*10)
2340 NEXT I
2350 REM END ENERGY CONTENT GRAPH
2360 REM
2370 REM WRITE R(50),R(90)
```

```
2380 DIM N(2)
2390 N(1)=0.5
2400 N(2)=0.9
2410 FOR I1=1 TO 2
2420 FOR I=1 TO J
2430 IF S(I)=>N(I1) THEN 2450
2440 NEXT I
2450 R1=P(I)-((P(I)-P(I-1))*((S(I)-N(I1))/(S(I)-S(I-1))))
2460 PRINT USING 2470:"R(",N(I1),")=",R1,"(UM)"
2470 IMAGE //,45X,2A,1D.1D,2A,4D,4A
2480 NEXT I1
2490 END
```

```
100 REM THIS PROGRAM CALCULATES THE ENERGY CONTENT OF A FOCAL SPOT
110 REM
120 INIT
130 REMARK GENERATE 4 CYCLE SEMILOG SHEET
140 PAGE
150 VIEWPORT 6,69,10,100
160 WINDOW 0,70,-0.05,4
170 AXIS 10,0,0,0
180 FOR I=2 TO 70 STEP 2
190 MOVE I,0
200 RDRAW 0,4
210 NEXT I
220 I=1
230 J=1
240 I=I+J
250 IF I>10000 THEN 310
260 AXIS 0,0,0,LGT(I)
270 IF I=10 OR I=100 OR I=1000 THEN 290
280 GO TO 240
290 J=I
300 GO TO 240
310 REMARK END OF 4 CYCLE SEMILOG GENERATION
320 REM
330 REM SCALING OF VERTICAL AXIS
340 REM
350 REM DEFINE MIRROR TRANSMISSION BELOW
360 R1=0.45
370 REM
380 HOME
390 PRINT " ","   ","GGG         ";"SHOT NUMBER IS ";
400 INPUT D$
410 PRINT USING 420:R1
420 IMAGE//45X,"TRANSM/PASS R1R2 = ",1D.2D
430 R2=R1
```

```
440 I1=0
450 MOVE -6,0
460 PRINT I1;
470 MOVE -6,LGT(1/R2)
480 I1=I1+1
490 PRINT I1;
500 MOVE 0,LGT(1/R2)
510 FOR I=1 TO 25
520 RDRAW 1,0
530 RMOVE 2,0
540 NEXT I
550 R2=R2*R1
560 IF LGT(1/R2)>4 THEN 580
570 GO TO 470
580 REM END VERTICAL SCALING
590 REM
600 REM USER RESCALES HORIZONTAL AXIS
610 FOR I=1 TO 2
620 MOVE 54,-0.05
630 PRINT "JJ";
640 PRINT "RADIUS(UM)","GGG"
650 NEXT I
660 MOVE 68,-0.05
670 PRINT "J";
680 INPUT R
690 WINDOW 0,R,-0.05,4
700 FOR J=1 TO 6
710 MOVE R/7*J,-0.05
720 A9=1/7*R*J
730 A$=STR(A9)
740 A$=SEG(A$,1,5)
750 RMOVE -R/20,0
760 PRINT "J";
770 PRINT A$
780 NEXT J
```

```
790 REM END OF HORIZONTAL SCALING
800 REM
810 REM DATA ENTRY
820 HOME
830 PRINT USING 840:"SPOT DATA","RADIUS    HEIGHT",    L?"
840 IMAGE ////,50X,9A,///,47X,14A,6A
850 DIM P(301),E(301)
860 P=0
870 E=0
880 I1=0
890 Z$="G"
900 FOR J=1 TO 301 STEP 10
910 HOME
920 I1=INT(I1+1)
922 FOR K=1 TO I1
924 PRINT
926 NEXT K
930 PRINT USING 940:Z$
940 IMAGE 10/,48X,1A,S
950 INPUT P(J)
959 X$="K"
960 PRINT USING 961:Z$,X$
961 IMAGE 57X,A,A,S
970 INPUT A1
975 PRINT USING 976:X$
976 IMAGE 65X,A,S
977 INPUT L$
980 IF A1=0 THEN 1010
990 E(J)=LGT((1/R1)^A1)
1000 GO TO 1020
1010 E(J)=0
1020 IF J<>1 THEN 1060
1030 MOVE P(J),E(J)
1040 DRAW P(J),E(J)
1050 GO TO 1110
```

```
1060 MOVE P(J-10),E(J-10)
1070 DRAW P(J),E(J)
1100 IF L$="L" THEN 1120
1110 NEXT J
1120 REM END DATA ENTRY
1130 REM
1140 REM INTERPOLATE BETWEEN ENTERED POINTS
1150 FOR I=1 TO J-10 STEP 10
1160 IF P(I+10)=P(I) THEN 1230
1170 T=ABS((E(I+10)-E(I))/(P(I+10)-P(I)))
1180 X=ABS(P(I+10)-P(I))
1190 IF E(I+10)=>E(I) AND P(I+10)>P(I) THEN 1280
1200 IF E(I+10)<E(I) AND P(I+10)>P(I) THEN 1360
1210 IF E(I+10)=>E(I) AND P(I+10)<P(I) THEN 1410
1220 IF E(I+10)<E(I) AND P(I+10)<P(I) THEN 1490
1230 FOR I1=I+1 TO I+9
1240 E(I1)=E(I)
1250 P(I1)=P(I)
1260 NEXT I1
1270 GO TO 1530
1280 FOR I1=I+1 TO I+9
1290 P(I1)=P(I)+(I1-I)*X/10
1300 IF E(I+10)<>E(I) THEN 1330
1310 E(I1)=E(I)
1320 GO TO 1340
1330 E(I1)=E(I)+(I1-I)*X*T/10
1340 NEXT I1
1350 GO TO 1530
1360 FOR I1=I+1 TO I+9
1370 P(I1)=P(I)+(I1-I)*X/10
1380 E(I1)=E(I)-(I1-I)*X*T/10
1390 NEXT I1
1400 GO TO 1530
1410 FOR I1=I+1 TO I+9
1420 P(I1)=P(I)-(I1-I)*X/10
```

```
430  IF E(I+10)<>E(I) THEN 1460
1440 E(II)=E(I)
1450 GO TO 1470
1460 E(II)=E(I)+(II-I)*X*T/10
1470 NEXT II
1480 GO TO 1530
1490 FOR II=I+1 TO I+9
1500 P(II)=P(I)-(II-I)*X/10
1510 E(II)=E(I)-(II-I)*X*T/10
1520 NEXT II
1530 NEXT I
1540 REM END OF INTERPOLATION
1550 REM THIS ROUTINE CALCULATES THE SUMS OF [(E(J)>[P(J)↑2-P(J-1)↑2]]
1560 DIM S(301)
1570 S=0
1580 REM IF FIRST ENTERED POINT WAS P(1)<>0 THEN LABEL DATA
1590 REM IN PROPER SEQUENCE
1600 IF P(1)=>R/35 THEN 1680
1610 REM
1620 FOR I=2 TO J
1630 S(1)=0
1640 H=(10↑E(I)+10↑E(I-1))*(P(I)↑2-P(I-1)↑2)/2
1650 S(I)=S(I-1)+H
1660 NEXT I
1670 GO TO 1780
1680 DIM E1(301),P1(301)
1690 FOR I=1 TO J
1700 E1(J+1-I)=E(I)
1710 P1(J+1-I)=P(I)
1720 NEXT I
1730 FOR I=1 TO J
1740 E(I)=E1(I)
1750 P(I)=P1(I)
1760 NEXT I
1770 GO TO 1610
```

```
1780 REM END OF SUMMATION. FINAL SUM IS S(J)
1790 REM
1800 REM RESCALE PARTIAL SUMS
1810 FOR I=1 TO J
1820 S(I)=S(I)/S(J)
1830 NEXT I
1840 REM END OF RESCALING
1850 REM
1860 REM GRAPH ENERGY CONTENT
1870 FOR I=3 TO J
1880 MOVE P(I-1),LGT(S(I-1)*10)
1890 DRAW P(I),LGT(S(I)*10)
1900 NEXT I
1910 REM END ENERGY CONTENT GRAPH
1920 REM
1930 REM WRITE R(50),R(90)
1940 DIM N(2)
1950 N(1)=0.5
1960 N(2)=0.9
1970 FOR I1=1 TO 2
1980 FOR I=1 TO J
1990 IF S(I)=>N(I1) THEN 2010
2000 NEXT I
2010 R1=P(I)-(P(I)-P(I-1))*(S(I)-N(I1))/(S(I)-S(I-1))
2020 PRINT USING 2030:"R(",N(I1),")=",R1,"(UM)"
2030 IMAGE //,45X,2A,1D.1D,2A,4D,4A
2040 NEXT I1
2050 END
```

APPENDIX I

```
1 REM THIS PROGRAM USES PRESSURES DEFINED OVER THE FWHM
2 REM OF THE LASER PULSE. AS A RESULT VELOCITIES CALCULATED
3 REM HERE ARE TOO BIG BECAUSE THE TARGET CONTINUES TO
4 REM ACCELERATE AFTERWTHE FWHM TIME. TO USE THIS PROGRM
5 REM PROPERLY SCALE IRRADIANCE SO THAT ONE EXPERIMENTAL
6 REM SHOT COMES OUT OK; THE USE THIS IRRADIANCE TO
7 REM PREDICT THE BEHAVIOUR OF ALL OTHER SHOTS.
8 REM ANOTHER OPTION IS TO CHOP THE PULSE AT THE FWHM POINT
9 REM THEN RUN THE CHOPPED PULSE.
10 REM NOTE THAT THE MASS ABLATION RATE IS DEFINED OVER
11 REM THE FULL PULSE WIDTH.
100 PAGE
110 INIT
120 PRINT "I***MOTION OF PLANAR FOIL***"
130 PRINT "JJ]ENTER THE FOLLOWING"
140 PRINT "]IRRADIANCE (W/CM↑2)=";
150 INPUT I1
160 PRINT "]TARGET DENSITY (GM/CM↑3)=";
170 INPUT R
180 PRINT "]TARGET THICKNESS (UM)=";
190 INPUT D
200 PRINT "]FWHM LASER DURATION (NSEC)=";
210 INPUT T
220 PRINT "]LARGEST TIME OF INTEREST>FWHM (NSEC)=";
230 INPUT T1
240 PRINT "]HOW MANY TIME STEPS (<>3) ?";
250 INPUT D1
260 PRINT "]J]DO YOU WANT TO ITERATE IRRADIANCE?";
270 INPUT Y$
280 IF Y$="Y" OR Y$="YES" THEN 300
290 GO TO 320
300 PRINT "]]PRESS RETURN TO ITERATE WHEN CALCULATION IS OVER"
305 FOR I=1 TO 5000
306 REM THIS IS A TIME LOOP
```

```
307  NEXT I
310  I$="0"
320  S=(T+T1)/D1
330  D1=D1+1
340  REM  DRAW AXIS
350  PAGE
360  VIEWPORT 0,100,10,85
370  WINDOW -T,T1,0,1
380  AXIS 0.5,0.2,0,0
390  MOVE -T,0
400  DRAW -T,1
410  DRAW T1,1
420  DRAW T1,0
430  T$="TIME (NSEC)  0.5NSEC/INT."
440  MOVE 0,0
450  PRINT "J";
460  PRINT "0";
470  PRINT "JJJJJJJJJJJJJJ";
480  PRINT T$
490  MOVE 0,1
500  PRINT "K";
510  PRINT "1";
520  HOME
530  PRINT USING 540:"I (W/CM↑2) =",I1,"TARGET DENS. (GM/CM↑3) ="
540  IMAGE 12A,1E,10X,24A,S
550  PRINT USING 560:R,"TARGET THICKNESS (UM) =",D,"FWHM (NS) =",T
560  IMAGE 2D.2D,/,23A,2D.2D,10X,11A,2D.2D,S
570  PRINT USING 580:"TIME STEPS =",D1-1
580  IMAGE /,12A,6D
590  WINDOW 1,D1,0,1
600  REM END OF AXIS PLOT
610  REM DEFINE IRRADIANCE
620  REMTNEXT LINE IS NORMALIZED TO PEAK =1 FOR GRAPHING
630  DEF FNE(X)=EXP(-((2*X/T)↑2)*LOG(2))
640  REM NEXT LINE NORMALIZED TO INTEGRAL OVER TIME =1
```

```
650 DEF FNI(X)=FNE(X)*0.9394/T
660 REM .9394/T IS THE NORMALIZATION FOR FNE(X)
670 REM IRRADIANCE SCALING FOR PRESSURE AND MASS ABLATION RATE
680 REM THESE FUNCTIONS WILL BE NORMALIZED AND USED LATER
690 DEF FNQ(X)=FNI(X)^0.8
700 DEF FNC(X)=FNI(X)^0.6
710 DIM E(D1)
720 DIM Q(D1)
730 DIM C(D1)
740 DIM Q1(D1)
750 DIM C1(D1)
760 FOR I=1 TO D1
770 X=-T+(I-1)*S
780 E(I)=FNE(X)
790 Q(I)=FNQ(X)
800 C(I)=FNC(X)
810 NEXT I
820 CALL "DISP",E
830 MOVE 0.7*D1,E(0.7*D1)
840 PRINT "PULSE"
850 CALL "INT",Q,Q1
860 CALL "INT",C,C1
870 DIM M(D1)
880 DIM M1(D1)
890 DIM P(D1)
900 REM PRESSURE AND ABLATION RATE DEFINED HERE
910 REM THESE ARE NORMALIZED TO MEASURED VALUES AT10^13 W/CM^2
920 FOR I=1 TO D1
930 B=INT(1+3*T/(2*S))
940 B1=INT(1+T/(2*S))
950 P(I)=2.5E+12*Q(I)*T*(I1/1.0E+13)^0.8/(S*(Q1(B)-Q1(B1)))
960 M(I)=T*2.5*C(I)*(I1/1.0E+13)^0.6*(1/R)/(S*4*C1(D1))
970 REM LINE 830 IS IN CGS, NEXT LINE IS IN UM/NSEC
980 NEXT I
990 REM GET TARGET MASS BY INTEGRATING MASS ABL. RATE
```

```
1000 CALL "INT",M,M1
1010 FOR I=1 TO D1
1020 M(I)=D-M1(I)*S
1030 IF M(I)<=0 THEN 1510
1040 E(I)=M(I)/D
1050 NEXT I
1060 CALL "DISP",E
1070 MOVE D1,1
1090 PRINT "   FINAL TARGETЛНННННННTHICKNESS(UM)ЛННННННННН";
1098 PRINT USING 1100:M(D1)
1100 IMAGE 6D.2D
1110 DIM A(D1)
1111 DIM G1(D1)
1120 DIM U(D1)
1130 DIM Y(D1)
1140 REM DEFINE ACCELERATION ARRAY IN CGS UNITS
1150 FOR I=1 TO D1
1160 A(I)=P(I)/(R*M(I)*1.0E-4)
1161 REM DEFINE THE SQR OF ACCELERATION TO GO INTO RALEIGH TAYLOR EXP.
1162 G1(I)=SQR(A(I))
1170 NEXT I
1180 CALL "MAX",A,Z,J
1190 DIM A1(D1)
1200 FOR I=1 TO D1
1210 A1(I)=A(I)/Z
1220 NEXT I
1230 CALL "DISP",A1
1240 MOVE D1,0.2
1250 PRINT "   MAX ACC.(CGS)";"ЛНННННННННН";
1260 PRINT USING "E":Z
1270 REM INTEGRATE TO GET VELOCITY ARRAY
1280 CALL "INT",A,U
1298 REM INTEGRATE THE SQR OF ACCELERATION TO GET THE EXPONENT
1300 REM IN THE RALEIGH TAYLOR GROWTH RATE
1302 CALL "INT",G1,G1
```

```
1305 MOVE D1,0.8
1310 PRINT " INT((ACC)↑.5)";"ᒧᒧᒧᒧ";"(CGS)";"ᒧᒧᒧᒧᒧᒧᒧᒧᒧᒧ";
1320 PRINT USING "E";G1(D1)*S*1.0E-9
1330 REM INTEGRATE TO GET DISTANCE TRAVELED BY TARGET
1340 CALL "INT",U,Y
1350 U1=U(D1)*S*1.0E-9
1360 X1=Y(D1)*S*S*1.0E-9*1.0E-9*10000
1370 REM U1 IS IN CM/SEC, X1 IS IN UM
1380 FOR I=1 TO D1
1390 U(I)=S*1.0E-9*U(I)/U1
1400 Y(I)=S*S*1.0E-9*1.0E-9*10000*Y(I)/X1
1410 NEXT I
1420 CALL "DISP",U
1430 MOVE D1,0.6
1440 PRINT " MAX VEL.(CGS)ᒧᒧᒧᒧᒧᒧᒧᒧᒧᒧᒧᒧ";
1450 PRINT USING "E";U1
1460 CALL "DISP",Y
1470 MOVE D1,0.4
1480 PRINT " ᒧGMAX DIST.(UM)ᒧᒧᒧᒧᒧᒧᒧᒧᒧᒧᒧᒧ";
1490 PRINT USING 1100:X1
1500 GO TO 1550
1510 REM BURNED THRU
1520 X=-T+(I-1)*S
1530 HOME
1540 PRINT "ᒧᒧᒧᒧᒧᒧᒧᒧᒧᒧᒧGGG***BURNED THRU*** AT";X;"NSEC"
1550 IF Y$="Y" OR Y$="YES" THEN 1570
1560 GO TO 1650
1570 INPUT I$
1580 IF I$="" THEN 1600
1590 GO TO 1650
1600 PAGE
1610 PRINT "INPUT FRACTIONAL CHANGE IN IRRADIANCE"
1620 INPUT F1
1630 I1=I1*(1+F1)
1640 GO TO 340
```

1650 END

APPENDIX J

EXPERIMENTAL METHODS FOR STUDYING THE RAYLEIGH-TAYLOR

INSTABILITY OF ABLATIVELY ACCELERATED TARGETS*

J.Grun,[+] M. H. Emery, M.J. Herbst, E.A. McLean

S.P. Obenschain, B.H. Ripin, J.A. Stamper and R.R. Whitlock

We describe new diagnostic methods for the study of hydrodynamic instabilities in ablatively accelerated targets. These methods include face-on x-ray backlighting that does not require a backlighting laser beam (for growth rate measurement), and a tracer dot technique (for tracking ablation plasma flow). The targets in our experiments are periodically perturbed to provide initial conditions for the growth of the Rayleigh-Taylor instability.

1

INTRODUCTION

Designs of hollow, directly irradiated inertial fusion pellets are constrained by the growth rates of the Rayleigh-Taylor (R-T) instability[1] in the ablation region. During the past few years we have used nonperturbed planar targets to model the dynamics of such fusion pellets early in the implosion phase, before spherical convergence effects become dominant.[2-5] We have successfully accelerated these targets up to 160 km/sec while keeping the target relatively cool (< 10 eV) and uniform (15%).[3,4] The target velocities were consistent with ablation pressures and ablation rates measured on the thrust (laser) side of the target.[3,5] Moreover, target nonuniformities observed in these experiments were shown to be related to nonuniformities in the irradiance profile:[3,4] We have not as yet observed any nonuniformities of accelerated nonperturbed targets that could be definitely ascribed to a hydrodynamic instability.[6]

To study the development of hydrodynamic instabilities such as the R-T during the ablation phase we have initiated experiments using accelerated periodically-perturbed targets.[7-10] Using perturbed targets[11,12] for R-T studies has these advantages:

- By seeding the instability with well-defined initial conditions experiment and theory may be compared more directly than is otherwise possible.

- The known periodicity makes it easier to differentiate between R-T effects which result from the initial periodic perturbation and other effects which are not related to the perturbation.

2

- By varying the wavelength and amplitude of the initial perturbation we
control the linear growth rate and the number of e-foldings necessary
to reach the nonlinear regime. Consequently, the linear and nonlinear
evolution of the instability is easier to study.

Our targets fall into two classes (Fig. 1), targets that are corrugated
(wiggly) with a constant areal mass density and targets that have a
periodically varying mass per unit area. The first type of target has an
initial amplitude perturbation only. The second type of target develops both
an amplitude and velocity perturbation early in the laser pulse due to the
differential acceleration across the target surface. Also, in the second
target type changes in the areal mass density across the target surface – and
hence the instability growth rate – may be more easily related to the initial
target perturbations.

To get measurable growth rates we accelerate the targets to 10^7 cm/sec
with a 5 nsec FWHM, 1.06 µm laser pulse. Under these conditions about 23
classical e-foldings ($\int \sqrt{kg}\ dt$) are expected for perturbation periods of
10 µm: Perturbations with periods as large as 300 µm are expected to grow
with about 4 classical e-foldings (Fig. 1). Thus, even if actual R-T growth
rates are reduced from $\sqrt{kg}$ by a factor of 2 or 3 as some predict,[13-15]
measurable growth rates can still be achieved in our parameter regime.

The following sections describe proof-of-principle tests[9,10] of two
experimental methods designed to study the linear and nonlinear evolution of
the R-T instability. The first method is a face-on x-ray backlighting
technique with which we hope to measure areal mass nonuniformity development
and, hence, the linear growth rates of the instability. The unique feature of
this technique is that it does not require a separate x-ray source or a

3

separate backlighting laser beam. The second method uses x-ray emission from tracer dots[16] to map out the ablation plasma flow from accelerated perturbed targets. This method may be capable of detecting the vortex shedding[17] and Kelvin-Helmholtz like rollup that are predicted to occur on the ablation side of unstable targets.[18]

FACE-ON X-RAY BACKLIGHTING

The R-T instability in a periodically perturbed target causes mass to flow laterally near the ablation surface from the thinner to the thicker parts of the target. Consequently, measurements of areal mass across the target surface at some known time into the laser pulse, or measurements of the rate-of-change of areal mass density across the target surface, can be related to the instability growth rates.

We deduce areal mass variations from the attenuation of an x-ray pulse that has passed through the spike and bubble structure in a target predicted to be R-T unstable. These x rays originate from a thin layer of magnesium that has been buried within a periodically perturbed target made of carbon. In these initial experiments the depth at which magnesium is buried is chosen so that the 5 nsec FWHM laser pulse burns through to the magnesium at 2.5 nsec past the peak laser intensity. The sequence of events is as shown in Fig. 2: First, the outer carbon layer is heated and ablates, accelerating the target but emitting relatively few x rays above 1 KeV. Once the outer carbon layer is depleted (and hopefully the R-T is well developed) the thin magnesium layer rapidly heats up emitting the short burst of > 1 KeV x rays that are used to radiograph the target.

Figure 3 shows the experimental setup. The C/Mg/C perturbed target is viewed by three pinhole cameras and a PIN-diode all filtered with 1/2 mil

4

beryllium. (An x-ray streak camera may also be used in the future.) One of the two pinhole cameras on the laser side of the target provides a two-dimensional image of the x-ray flash source; the second, with a carbon step filter in front, provides a calibration of the film density as a function of the carbon areal mass that the x rays pass through. The third camera, at the target rear, records the radiograph of the target. The diode is used to measure the duration of the Mg x-ray pulse and its timing.

This face-on x-ray backlighting method has some very nice features: No separate backlighting laser beam is needed; alignment of diagnostics is easier than in a comparable experiment with a separate backlighting source; the diagnostics are simple, and the system is self-calibrating on each shot. It is also possible to account for x-ray source nonuniformities during data reduction by comparing the x-ray source photograph with the radiograph. On the other hand, the target is somewhat complicated and there may be some space versus time distortion due to possible non-simultaneity of the Mg emission across the target.

Our first experiments tested whether the magnesium pulse was sufficiently brighter than the less intense but longer duration carbon x rays, whether the x-ray film density is a sufficiently sensitive function of the carbon target areal mass density, and whether the magnesium x-ray pulse is sufficiently short to make a meaningful growth rate measurement with a pinhole camera. To check the ratio of magnesium to carbon x-ray emission we shot a perturbed target in which the buried magnesium layer and the overlaying carbon had the shape of a disk of about the same diameter as the laser focal spot. The laser focal spot was offset with respect to this disk so that a part of the beam was incident on pure carbon, exciting carbon x rays only, and a part was incident on the C/Mg/C layer. The laser irradiance and thicknesses of C/Mg layers were

chosen so that the magnesium would light up at about 2 nsec past the peak of the pulse and deplete 1/2 nsec later. Figure 4 describes the experimental parameters and shows photographs of the x-ray source as well as the resulting radiograph. The radiograph shows a clear picture of the perturbed target. The exposure levels caused by x rays from the layered C/Mg/C region were about 6 times greater than exposures from the pure C region for a pinhole diameter of 6-8 μm and a pinhole camera magnification of 2.5. The signal/noise ratio in this experiment is therefore adequate.

It is interesting to note that the radiograph in Fig. 4 shows some large-scale nonuniformities that are not correlated with the initial target perturbation. Some of these nonuniformities appear in the x-ray source photo as well and are probably related to imperfections in the carbon/magnesium coatings. These types of nonuniformities can be accounted for in data reduction; also, improvements in the fabrication of the layered targets can be made. Other small-scale nonuniformities appear in the radiograph but not in the x-ray source. These may be caused by the instability mechanism itself or, perhaps, by variations in target thickness caused by a nonuniform laser beam. In either case, two-dimensional pinhole pictures will be necessary to monitor and understand the phenomenon.

The functional relationship between the film density and the areal density of carbon that the x rays passed through depends on the location of the film's H-D curve - or equivalently on the source intensity, spectrum, duration, the amount of intervening carbon, pinhole diameter, camera magnification and so on. Because so many variables affect the result, in the future we intend to take in situ calibration measurements on each shot through an array of pinholes.

For this experiment calibration was done on separate shots. An example

6

of a film density versus carbon areal density curve for an 8 μm diameter pinhole, camera magnification of 2 and other conditions similar to Fig. 4 is shown in Fig. 5. Under these conditions the useful range of film density corresponded to areal mass density less than 1.5 mg/cm^2. The ratio of C/Mg layer to C x-ray induced density (signal/noise) was high. A larger, 13 μm diameter, pinhole showed reduced signal/noise but carbon thicknesses up to 2 mg/cm^2 were easily distinguishable.

We measured the duration of the magnesium x-ray pulse using a filtered MRD-500 photodiode, which has a 1/2 nsec rise time. However, since this measurement is spatially integrating, nonuniformities in the laser pulse which ablate the target at different rates as well as imperfections in the carbon/magnesium layers broaden the diode pulse; the result is an upper limit on the x-ray pulse duration for a given location on the target. This upper limit was measured to be 2 nsec FWHM. In future experiments we will deposit the magnesium layer locally within the focal spot, improve the quality of our targets, and improve the temporal resolution so as to measure the actual x-ray pulse duration.

What if the magnesium x-ray pulse is not significantly shorter than 2 nsec - can meaningful measurements still be made? The answer is yes - although the flexibility of this backlighting method would be reduced. For example, during the latter part of the laser pulse the number of classical integrated R-T growth periods $\left(\int_{-\infty}^{t} \sqrt{kg} \, dt \right)$ changes by only 20% since the laser power, and therefore, target acceleration are falling rapidly (Fig. 2). A measurement of such a slowly varying quantity is possible with a 2 nsec x-ray pulse. But a 2 nsec FWHM x-ray pulse is too long to allow multiple flash experiments where laterally offset magnesium layers are buried at varying depths in the target to temporally and spatially resolve the evolution

7

of areal mass perturbations with pinhole camera diagnostics. An x-ray streak camera would have to be used under such circumstances.

TRACER METHOD FOR FLOW VISUALIZATION

The ablation plasma flow from a R-T stable and R-T unstable target is predicted to be very different. If a R-T stable target is irradiated by a relatively uniform laser beam the ablation plasma flows in a fan pattern which resembles that of an incompressible fluid squirting from a circular nozzle.[16] In a linearly unstable R-T target, however, non-colinear pressure and density profiles in the ablation plasma are thought to generate vorticity near the ablation surface causing the ablating plasma to be shed from the target in a circulating pattern resembling that of a Kármán vortex street.[17] In nonlinearly unstable R-T targets the vorticity is thought to be advected up the sides of R-T spikes producing a Kelvin-Helmholtz-like rollup of the spike tips.[15,18] The degree of rollup may depend on the details of initial perturbation (square vs sinusoidal),[15] and the wavelength of the perturbation.[18] These phenomena may be responsible for the reduction of the linear R-T growth rates below classical ($\sqrt{kg}$) and for the eventual saturation of the instability.[17,18]

Figure 6 shows the nonlinear Kelvin-Helmholtz-like rollup of the spike tips of a strongly perturbed R-T unstable target as predicted by the NRL FAST 2D simulation.[18] The corresponding flow pattern is shown in Fig. 7.

We are attempting to apply tracer methods used successfully in other experiments,[3,16,19] to detect the above phenomena in periodically perturbed targets predicted to be R-T unstable. The experimental arrangement is shown in Fig. 8. A row of aluminum or silicon tracer dots is embedded into or deposited on the surface of a periodically-perturbed polystyrene (CH) or

8

carbon target. (For the experiments below the tracer material was aluminum deposited on a carbon surface.) When the target is irradiated the tracers and the target surface heat-up and ablate away. Since the tracers are much stronger emitters of x rays in the spectral band of the pinhole camera (≥ 1 keV) than either carbon or polystyrene, the location of tracer ions in the ablation plasma flow is identified through their emission. We assume that the tracers do not significantly perturb the dynamics of the ablation plasma flow. This assumption is reasonable since the speed of Al, Si, and CH or C target ions, measured with time-of-flight ion collectors, is the same. Also for a uniform electron density in the ablation plasma the fully-ionized ion mass density for Al and CH (C) targets differ by only 12% (4%): Si and C fully-ionized ion mass densities differ only by 0.2%. Embedded Si tracers should not perturb the target dynamics significantly either since Si and C densities are about equal (2.32 vs 2.25 gm/cm^3).

Examples of the targets we use are shown in Fig. 8. The target types are: wiggly CH targets with Al dot tracers, areal mass perturbed carbon targets with Al dot tracers, and areal mass perturbed carbon targets with rectangular aluminum tracers that lie only on the thicker parts of the target and have, therefore, the same periodicity as the target perturbations.

For the experiments described below the targets were viewed edge-on with a pinhole camera. Since this gives no time resolution the expected circular plasma motion will show up as a smearing of the tracer image. In the future we intend to also use an x-ray streak camera to get the desired temporal resolution and spatially two-dimensional information.

Our experiments show that the plasma flow from perturbed and nonperturbed targets can indeed be very different. In the nonperturbed case each tracer dot maps into a distinct flux tube as the ions flow away from the target (Fig.

9

8,9). In contrast, flux tubes from perturbed targets merge together indicating that lateral plasma flow occurs. This is seen most clearly in Fig. 9 which resolves the flow from a 200 µm period, 2:1 areal mass perturbed target using six tracer dots per period. A similar target with a 50 µm period (Fig. 10) shows such a merging of flux tubes also but with poorer resolution (2 tracer dots/period). The lateral plasma flow deduced from these figures resembles that expected from R–T unstable targets, but more mundane mechanisms associated with dynamic breakup of these heavily perturbed targets cannot be excluded. Future experiments with improved time resolution and more extensive parameter variation will differentiate between the possible flow mechanisms.

It is interesting to note that the x-ray emission from the thicker portions of the heavily perturbed target in the edge-on photos of Fig. 9 and Fig. 10 is greater than the emission from the thinner portions. The same phenomenon is seen in Fig. 11 which shows a frontal view of the emission from a heavily perturbed carbon target. Since the height of the initial perturbation step in all these targets is much smaller than the critical to ablation distance, these brightness variations appear to be due to phenomena occurring during the target acceleration. For example, similar phenomena caused by a R–T spike shielding a R–T bubble from laser radiation have been observed in numerical simulations.[14] Effects not related to the R–T may also explain our observations: For instance, if the thinner part of the target accelerates ahead of the thicker part, the critical to ablation distance may be smaller near the thicker part than near the thinner part. If this were so, laser energy would transport preferentially to the thicker part causing it to emit more brightly. In any case care must be taken experimentally that the target self emission, which can acquire the periodicity of the imposed perturbations, does not distort areal mass measurements. Cases in which the

ratio of backlighter to target x-ray emission is not very large or the contrast of the backlighter x rays as they pass through the thicker and thinner parts of the target is not very large require special care.

Very interesting and unexpected plasma flow patterns were seen in a few cases. The most interesting of these is shown in Fig. 12. Here the target was an areal mass perturbed type with tracers that were in phase with the 150 μm perturbation period. The plasma flow from most of this target exhibits the lateral expansion that has been observed in Fig. 9 and Fig. 10. But the flow from one location behaves very differently: The plasma near the target surface in this location is compressed and is dimmer than plasma from other comparable regions of the target. Further from the target surface a dramatic decompression occurs and coincidently the plasma emission increases. Still further from the target surface the plasma becomes compressed and dimmer but this time the compression ratio is much smaller. (The second compression cycle is seen on the negative though it may not be clearly visible on the figure.) This phenomena is all the more amazing since it is seen in a time-integrated pinhole picture. The flow pattern, therefore, resembles a standing-wave-like phenomenon.

CONCLUSION

We are developing methods to measure the growth rate and ablation characteristics of hydrodynamically unstable targets. In our experiments perturbations which may seed the instability are purposely introduced in the targets. The first experiments using a face-on x-ray backlighting method and a tracer-dot method have been described. Both methods show promise. Parametric studies will be attempted in the near future.

11

ACKNOWLEDGMENTS

REFERENCES

1. G. Taylor, Proc. Roy. Soc. A201, 192 (1950).

2. B.H. Ripin, R. Decoste, S.P. Obenschain, S.E. Bodner, E.A. McLean, F.C. Young, R.R. Whitlock, C.M. Armstrong, J. Grun, J.A. Stamper, S.H. Gold, D.J. Nagel, R.H. Lehmberg, J.M. McMahon, Phys. Fluids 23(5), 1012 (1980); 24, 990(E) (1981); J. Grun, Naval Research Laboratory Memorandum Report 4491, 1981; R.R. Whitlock, S.P. Obenschain, J. Grun, Appl. Phys. Lett. 41, 429 (1982).

3. J. Grun, S.P. Obenschain, B.H. Ripin, R.R. Whitlock, E.A. McLean, J. Gardner, M.J. Herbst, J.A. Stamper, Naval Research Laboratory Memorandum Report Number 4747, 1982 (accepted for publication in Physics of Fluids).

4. S.P. Obenschain, J. Grun, B.H. Ripin, E.A. McLean, Phys. Rev. Lett. 46, 1402 (1981); 48, 709(E) (1982).

5. J. Grun, R. Decoste, B.H. Ripin, J. Gardner, Appl. Phys. Lett. 39, 545 (1981).

6. Other authors have also looked for the Rayleigh-Taylor instability in ablatively accelerated targets: J.D. Kilkenny, J.D. Hayes, C.S. Lewis, and P.T. Rumsby, J. Phys. D: Appl. Phys. 13, L123 (1980); A. Raven, H. Azechi, T. Yamanaka, and C. Yamanaka, Phys. Rev. Lett. 47, 1049 (1981).

7. B.H. Ripin, S.P. Obenschain, J. Grun, C.K. Manka, M.J. Herbst, E.A. McLean, J.A. Stamper, R.R. Whitlock, J.M. McMahon, S.E. Bodner, Bull. Am. Phys. Soc. 25, 946 (1980).

8. J. Grun, S.P. Obenschain, R.R. Whitlock, M.J. Herbst, B.H. Ripin, E.A. McLean, M.H. Emery, J. Gardner, Bull. Am. Phys. Soc. 26, 1023 (1981).

9. J. Grun, M.J. Herbst, E.A. McLean, S.P. Obenschain, B.H. Ripin, J.A. Stamper, R.R. Whitlock, F. Young, Abstract of the 12th Annual Conference on the Anomalous Absorption of Electromagnetic Waves in Sante Fe, NM (1982).

10. J. Grun, S.P. Obenschain, M.J. Herbst, M. Emery, R.R. Whitlock, B.H. Ripin, J.A. Stamper, Bull. Am. Phys. Soc. 27, 1028 (1982).

11. Perturbed targets were also used in electron beam driven experiments by M.A. Sweeny, F.C. Perry, J. Appl. Phys. 52, 4487 (1981).

12. Other laboratories now using or planning to use perturbed targets in Rayleigh-Taylor experiments include Rutherford Appleton Laboratory and Lawrence Livermore National Laboratory: Rutherford Annual Report to the Laser Facility Committee 1982; Karnig O. Mikaelian (private

communication).

13. R.L. McCrory, L. Montierth, R.L. Morse, and C.P. Verdon, Phys. Rev. Lett. 46, 336 (1981).

14. M.H. Emery, J.H. Gardner, J.P. Boris, Phys. Rev. Lett. 48, 677 (1982).

15. R.G. Evans, A.J. Bennett, G.J. Pert, Phys. Rev. Lett. 49, 1639 (1982).

16. M.J. Herbst, J. Grun, Phys. Fluids 24, 1917 (1981).

17. M.H. Emery et al., 9th International Conference on Plasma Physics and Controlled Nuclear Fusion Research, Paper W9, Baltimore, MD (September 1-8, 1982). M.H. Emery, J.H. Gardner, and J.P. Boris, Bull. Am. Phys. Soc. 27, 1042 (1982). (Submitted to Phys. Rev. Lett.)

18. M.H. Emery, J.H. Gardner, J.P. Boris, Appl. Phys. Lett. 41, 808 (1982).

19. M.J. Herbst, P.G. Burkhalter, J. Grun, R.R. Whitlock, M. Fink, Rev. Sci. Instr. 53, 1418 (1982).

Fig. 1   Hydrodynamic instabilities are studied using accelerated, periodically perturbed targets. Amplitude modulated targets with constant areal mass and areal mass modulated targets are illustrated. The number of classical Rayleigh-Taylor e-foldings during the laser pulse is shown as a function of final target speed to illustrate where measurable growth rates may be achieved in the experiment. λ is the wavelength of the Rayleigh-Taylor mode.

Fig. 2   Schematic of the temporal behavior of the laser pulse, magnesium x-ray flash, and $\int_{-\infty}^{t} \sqrt{kg}\, dt$ integrated over the laser pulse. The exact duration of the x-ray flash is uncertain as indicated by the dashed lines. If the x-ray flash is bright and of short duration the instability growth may be temporally resolved using pinhole cameras.

Fig. 3   Setup of the face-on x-ray backlighting experiment. The function of each diagnostic is described in the text. The arrow indicates the incident laser direction.

Fig. 4   Radiograph of a perturbed target and an image of the x-ray source. On this shot the buried magnesium layer, which has the shape of a disk, is offset with respect to the focal spot. The oval brighter images are caused by the x rays emitted by the magnesium layer. Th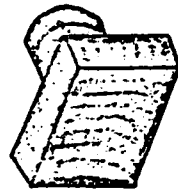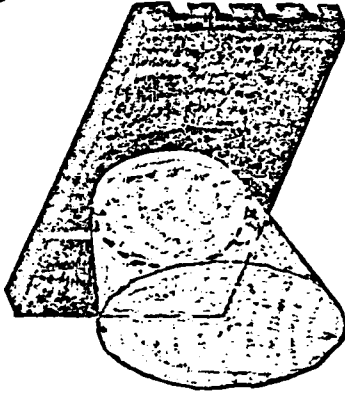e dimmer part of the image is caused by the emission of carbon x rays only. The parameters of this shot are: target perturbation period = 50 μm with peak (valley) thickness = 8.7 μm (5.4 μm), upper carbon over layer thickness = 1 μm, and Mg-

layer thickness = 0.1 µm; average irradiance = 1×10^{13} W/cm^2.

Fig. 5   Optical density of x-ray film as a function of the areal density of a cold carbon filter for an 8 µm pinhole and a camera magnification of 2. The irradiance and C/Mg layer thicknesses were similar to those of Fig. 4. The Mg/C x-ray source curve and the C x-ray source curve were obtained on separate shots.

Fig. 6   Density contours of a nonlinearly unstable Rayleigh-Taylor target predicted by the NRL Fast 2D code. The target parameters and time of the "snapshot" are shown in the figure.

Fig. 7   Predicted ablation plasma flow patterns for the same conditions as in in Fig. 6.

Fig. 8   Experimental arrangement and targets used to visualize the ablation plasma flow from periodically perturbed targets. Upper left: the experimental arrangement. Lower left: fan-like plasma flow from an accelerated planar target. Upper right: corrugated plastic target with aluminum tracer dots. Lower right: carbon targets with perturbed areal mass and tracer dots. Target dimensions are exaggarated for clarity in these sketches.

Fig. 9   Plasma flow from a flat (left) and a perturbed target (right). The perturbation period is 200 µm with an areal mass ratio (thick/thin) of 2. There are approximately 6 tracer dots per perturbation period. Unlike the flat target case where flux tubes of individual tracer dots are visible, the individual flux tubes in the perturbed case are not distinguishable. The perturbed target photos were taken on the same shot through three different diameter pinholes. The smallest pinhole photo is on the bottom; the largest pinhole photo on the top.

16

Fig. 10   Plasma flow from a target perturbed with a 50 μm period.   The
           photographs of the perturbed target were taken on the same shot
           through three different diameter pinholes.   The smallest pinhole
           photo is on the bottom; the largest pinhole photo on the top.
           There are about two tracer dots per perturbation period.

Fig. 11   Pinhole photograph of $\geq$ 1 KeV x-ray emission taken from the laser
           side of a heavily perturbed carbon target.

Fig. 12   Unusual plasma flow from a perturbed target diagnosed with aluminum
           tracers matched to the perturbation period.   Note the compression
           and expansion of ablation plasma on the right laser side of the
           photograph.

SEED INSTABILITY

1.05um

5ns FWHM

10^{13} W/cm^2

1mm DIAMETER SPOT
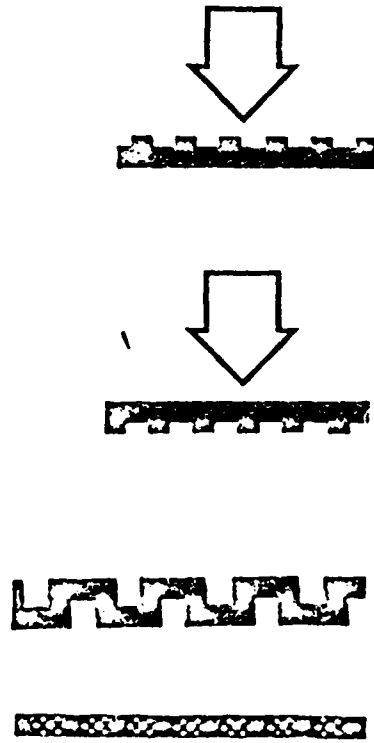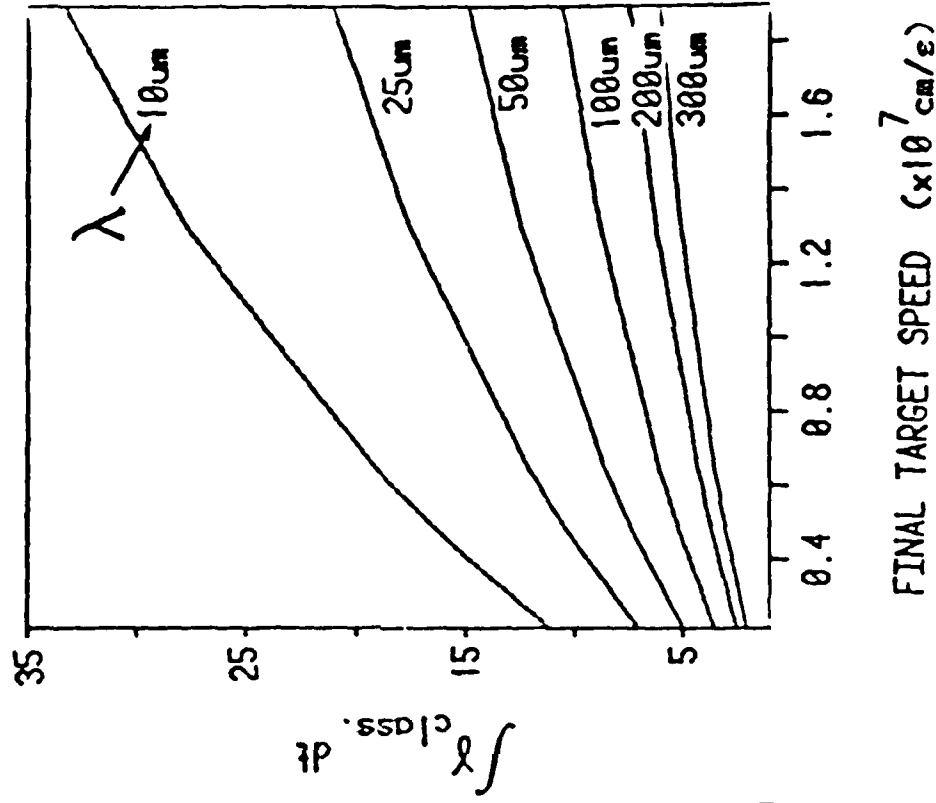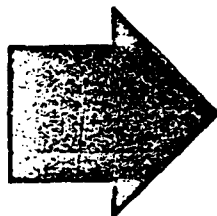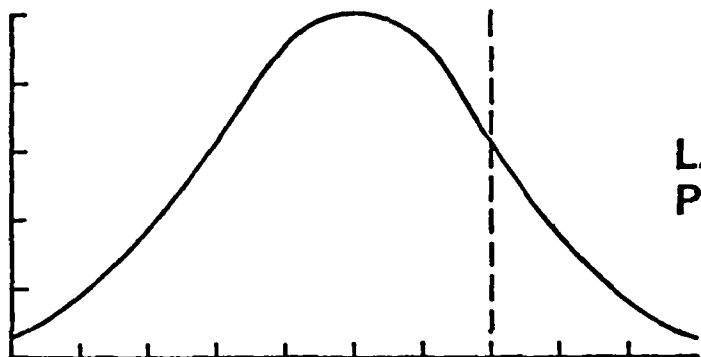
LASER
PULSE
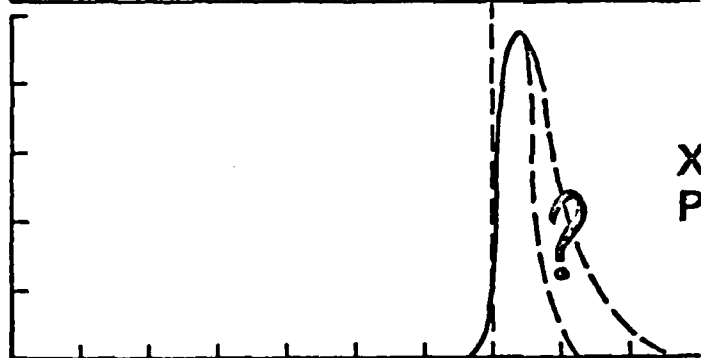
X-RAY
PULSE

ARBITRARY SCALE
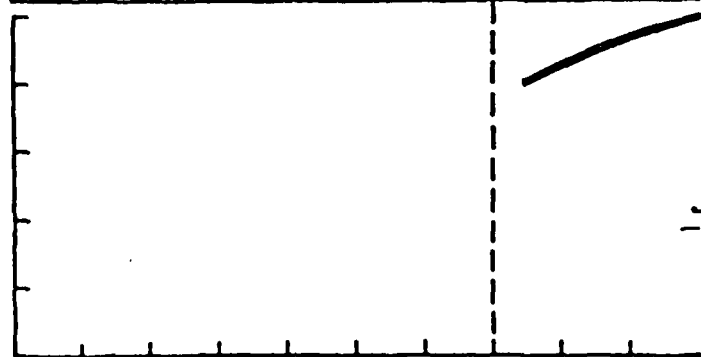
$$\int_{-\infty}^{t} [\text{ACCELERATION}]^{\frac{1}{2}} dt$$

$(V_{FINAL} = 1 \times 10^7 cm/sec)$

TIME (ns)

SETUP

DIODE OR X-RAY STREAK CAMERA

CARBON

Mg (X-RAY SOURCE)

DIODE OR X-RAY STREAK CAMERA

CARBON FILTER

C/Mg LAYER

LASER

RADIO GRAPH

X-RAY SOURCE

(8μm DIAMETER PINHOLE)

(6μm DIAMETER PINHOLE)

1mm
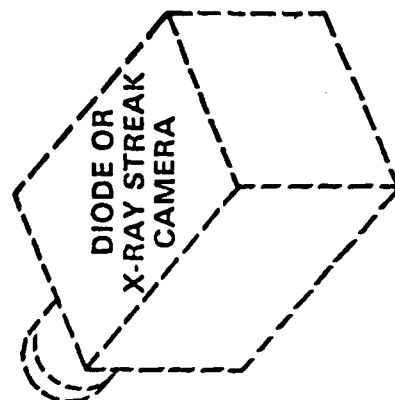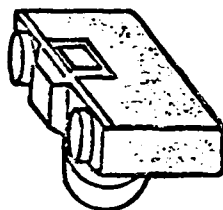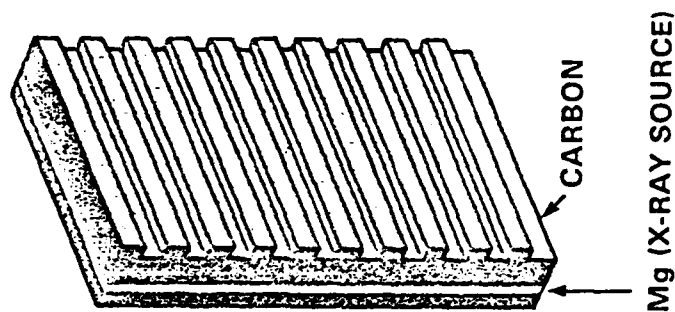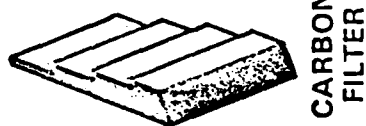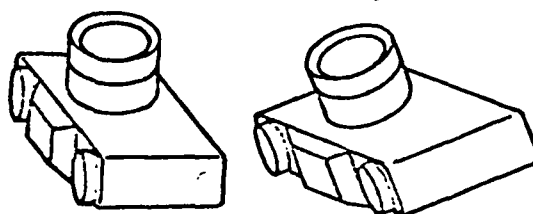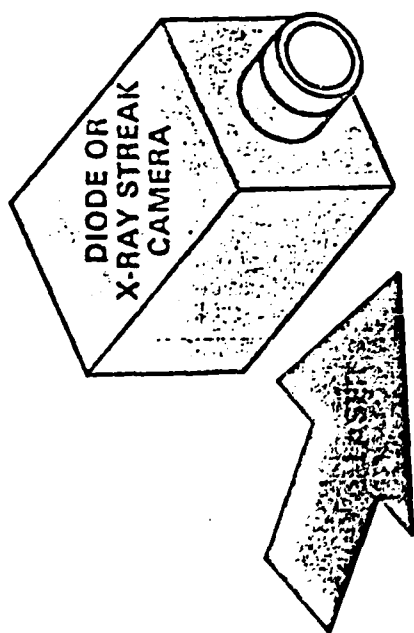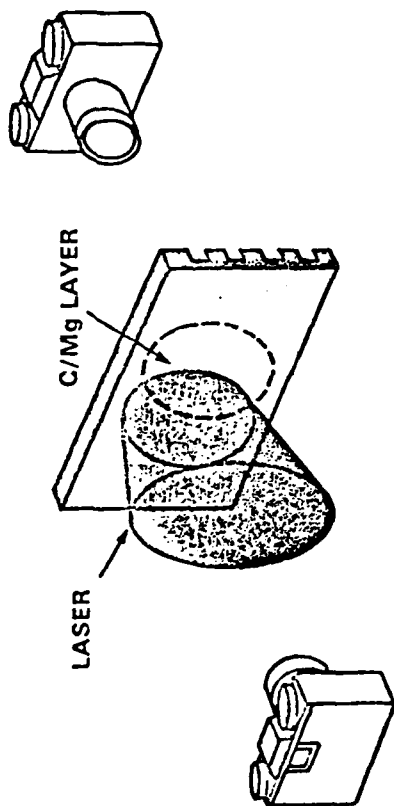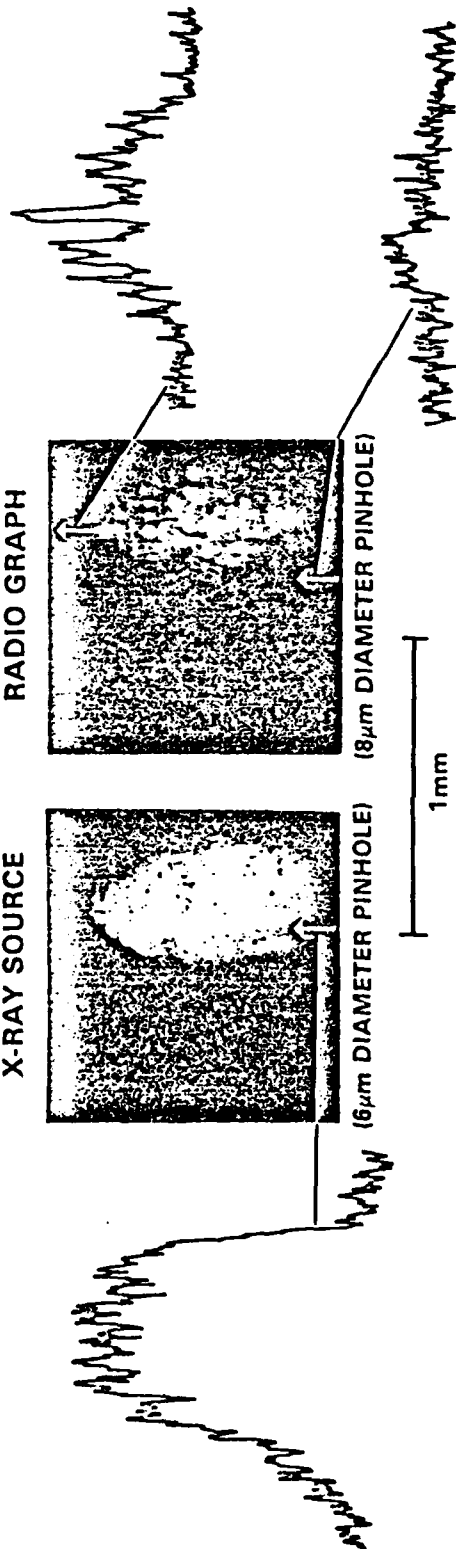
X-RAY SOURCE

CARBON
FILTER

X-RAY SOURCE
X Mg/C LAYER
● C
(8μm DIAMETER PINHOLE)

AREAL DENSITY OF CARBON (mg/cm²)

OPTICAL DENSITY
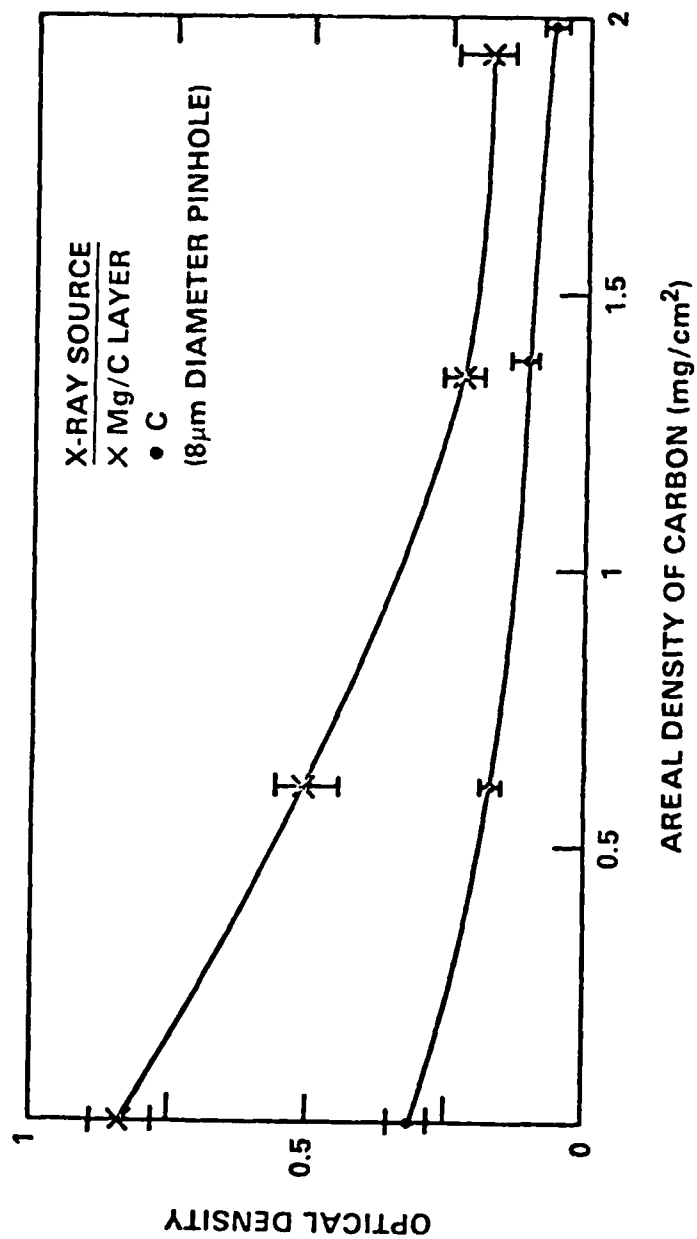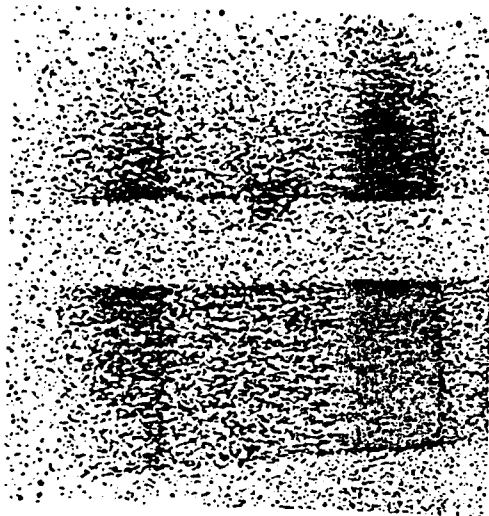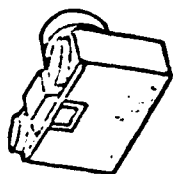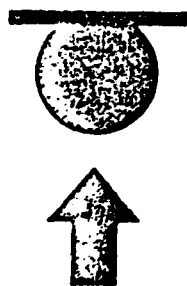
MEASURE HOT AND COLD SIDE
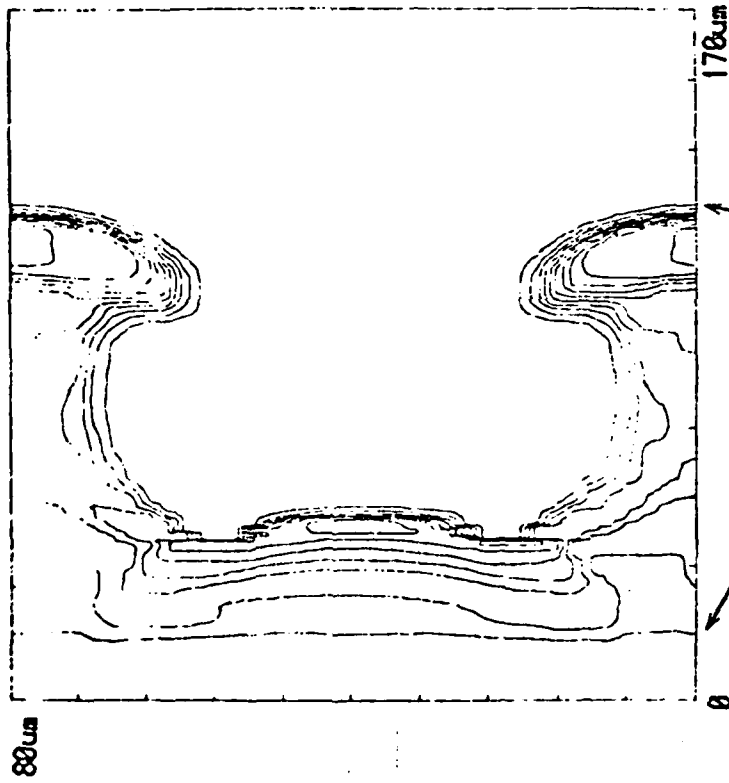
(1.4ns AFTER LASER PEAK)

$2 \times 10^{13} W/cm^2$

3.5ns FWHM

15um CH (thick part)

MASS RATIO ~ 1.7

DENSITY

10% of SOLID
(10% INCREMENTS)
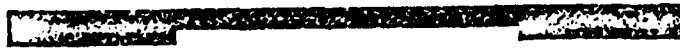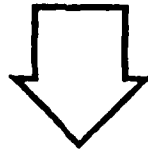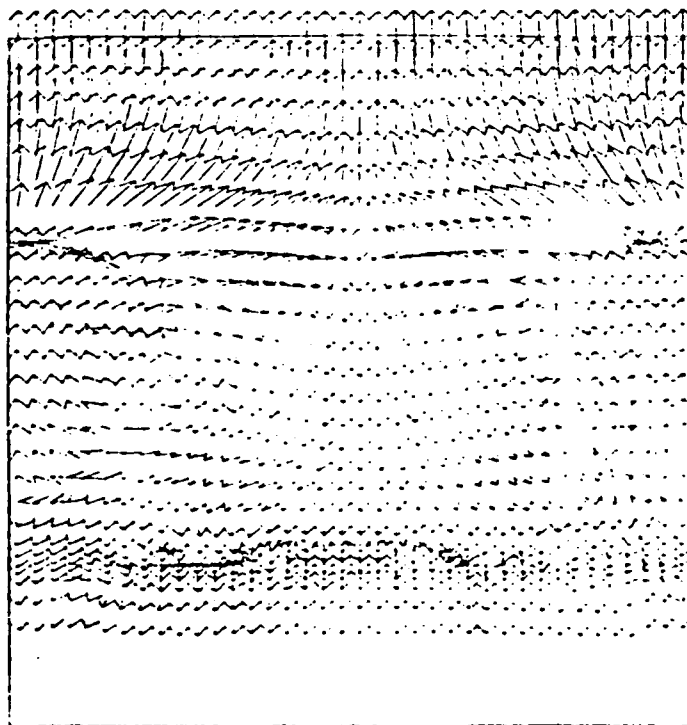
PERTURBATION PERIOD
150UM
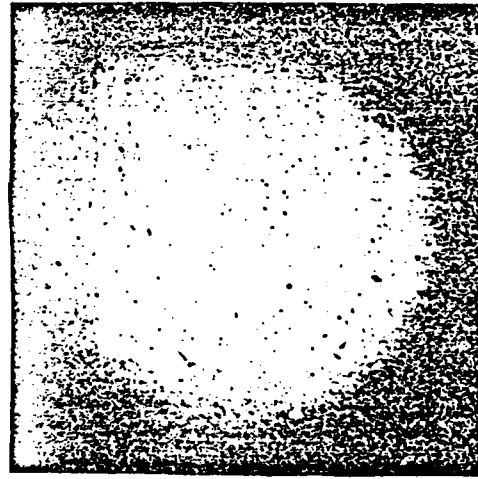
THICK/THIN
1.9
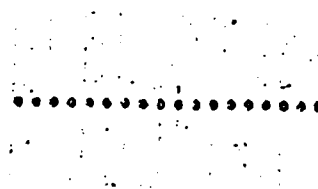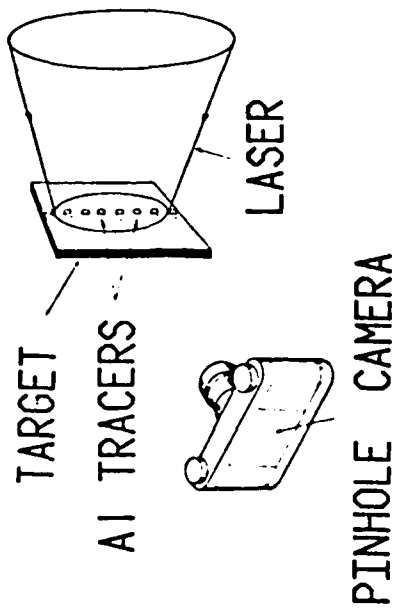
50um PERIOD
(CH TARGET)
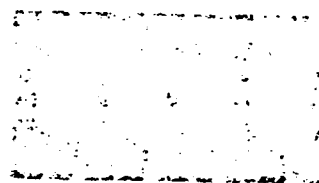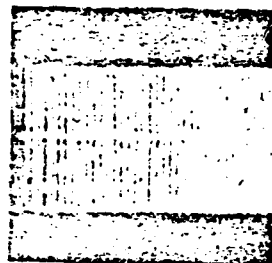
50um PERIOD

100um PERIOD

50um PERIOD

(CARBON TARGETS)

TARGET

AI TRACERS

LASER

PINHOLE CAMERA

1 mm

$1 \times 10^{13} W/cm^2$

200um PERIOD

1.6mg/cm2 (thick)

$\dfrac{\text{thick mass}}{\text{thin mass}} - 2$

1mm

1.5mg/cm2

35um

SHOTS 11844,60

SHOT 11887

1 mm
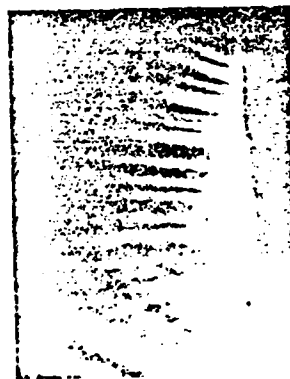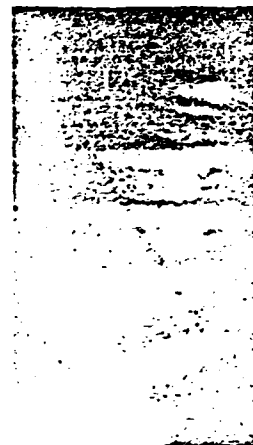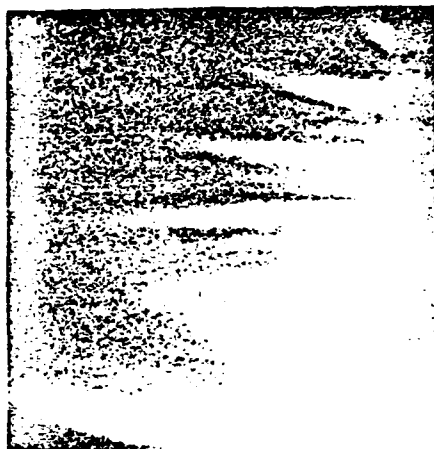
$1 \times 10^{13} W/cm^2$

TARGET

1.6 mg/cm2

$\dfrac{\text{thick mass}}{\text{thin mass}} - 2$

PERIOD - 50um

TRACERS

10um DIAMETER DOTS

35um CENTER TO CENTER
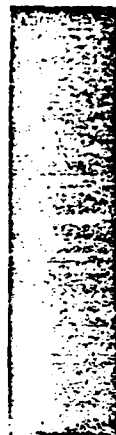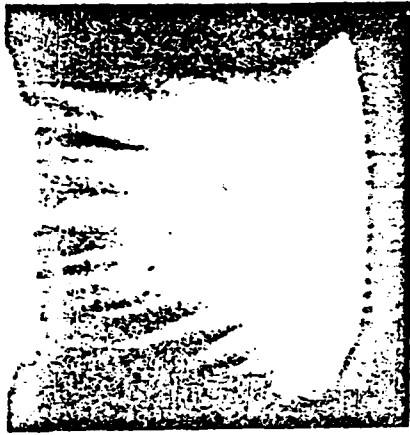
$4 \times 10^{12} \text{W/cm}^2$

0.8mg/cm^2 (thick)

$\dfrac{\text{thick mass}}{\text{thin mass}} - 1.3$

1mm

150um

SHOT 11863

APPENDIX K

REPORT DOCUMENTATION PAGE		READ INSTRUCTIONS BEFORE COMPLETING FORM
1. REPORT NUMBER NRL Memorandum Report 4893	2. GOVT ACCESSION NO.	3. RECIPIENT'S CATALOG NUMBER
4. TITLE (and Subtitle) MEASUREMENTS OF LASER COUPLING AND PLASMA PROFILES IN LONGER-SCALELENGTH PLASMAS		5. TYPE OF REPORT & PERIOD COVERED
		6. PERFORMING ORG. REPORT NUMBER
7. AUTHOR(s) M.J. Herbst, P.G. Burkhalter, J. Grun,* S.P. Obenschain, J.A. Stamper, F.C. Young, E.A. McLean, B.H. Ripin, and R.R. Whitlock		8. CONTRACT OR GRANT NUMBER(s)
9. PERFORMING ORGANIZATION NAME AND ADDRESS Naval Research Laboratory Washington, D.C. 20375		10. PROGRAM ELEMENT PROJECT, TASK AREA & WORK UNIT NUMBERS DPE AI08-79DP 40092(172) 47-0859-0-2
11. CONTROLLING OFFICE NAME AND ADDRESS U.S. Department of Energy Washington, D.C. 20545		12. REPORT DATE September 30, 1982
		13. NUMBER OF PAGES 22
14. MONITORING AGENCY NAME & ADDRESS(if different from Controlling Office)		15. SECURITY CLASS. (of this report) UNCLASSIFIED
		15a. DECLASSIFICATION/DOWNGRADING SCHEDULE

16. DISTRIBUTION STATEMENT (of this Report)

Approved for public release; distribution unlimited.

17. DISTRIBUTION STATEMENT (of the abstract entered in Block 20, if different from Report)

18. SUPPLEMENTARY NOTES

*Present Address: Mission Research Corp., Alexandria, VA 22312

19. KEY WORDS (Continue on reverse side if necessary and identify by block number)

Laser-matter interaction
Plasma instabilities
X-ray spectroscopy
Plasma diagnostics

20. ABSTRACT (Continue on reverse side if necessary and identify by block number)

Novel configuration of our two-beam laser allows laser-coupling experiments to be performed in longer-scalelength plasmas ($L_n \simeq 250\text{-}600$ μm at $n_c/10$), which better simulate reactor-sized pellet plasmas. Preliminary observations show increased backscatter, as expected, but also reveal large reductions in $2\omega_0$ and high-energy x-ray emissions. The latter may indicate lessened importance of resonance absorption in longer-scalelength plasmas. Measurements of plasma profiles are at least as important as coupling measurements in these experiments and we show new diagnostic techniques

(Continued)

DD FORM 1473 EDITION OF 1 NOV 65 IS OBSOLETE
1 JAN 73
S/N 0102-014-6601

20   ABSTRACT (Continued)

based upon tracer-dot methods. These include the first techniques available for velocity profile measurement, as well as an improved x-ray spectroscopic method for density and temperature profile measurement.

CONTENTS

MEASUREMENTS OF LASER COUPLING AND PLASMA PROFILES IN LONGER-SCALELENGTH PLASMAS

I. INTRODUCTION

To maximize applicability of current laser-plasma coupling experiments to high-gain laser fusion, these experiments should include three very important characteristics. First, laser-target coupling studies should be performed in plasmas with longer density, temperature, and velocity scalelengths to minimize the extrapolation which must be made from present experiments to the multimillimeter-scalelength plasmas anticipated for high-gain pellets. Second, measurements should be made over a wide range of scalelengths to provide a number of benchmarks for the plasma and hydrodynamics codes which are used to make the extrapolation. This is important because the absorption physics in long-scalelength plasmas may be qualitatively (as well as quantitatively) different from that in short-scalelength plasmas; the various processes which determine absorption efficiency depend differently on plasma scalelengths, and the processes which determine the absorption efficiency in short-scalelength plasmas might not be the same processes which are most important in long-scalelength plasmas. Finally, it is important that a complete set of plasma scalelength measurements be made in these experiments. If one measures absorption or scattered light and does not specify the scalelengths, free parameters are available which may be used in a hydro-code calculation to fit the measurements; for example, the flux limiter may be varied (which alters the plasma profiles) to obtain agreement with the experiment. In this case, the physics assumptions in the calculation are not being properly tested, and no confidence is developed in the ability of the hydro-code to predict laser-target coupling in reactor-sized plasmas.

Standard measurements of laser coupling with solid targets exhibit weaknesses on all three points. As illustrated in Fig. 1, these generally involve focusing the laser to a small spot in order to obtain the higher intensities of interest for high-gain scenarios. Planar geometry, rather than spherical, is commonly used because somewhat longer plasma scalelengths can be produced with fixed laser power and intensity. Even so, scalelengths produced by a small focal spot are still much shorter than reactor scalelengths because of the divergent flow of plasma from the finite planar spot. Moreover, variations of laser intensity and plasma scalelength cannot be made independently. If the laser power is varied to change the irradiance at constant spot size, the plasma scalelength varies also; if laser spot size is varied to control plasma scalelength, laser irradiance and focal quality change as well. Measurements of density and temperature profiles have not been made routinely in these experiments, and techniques for velocity profile measurement have not been developed.

Significant physics results have been obtained in previous experiments designed to address laser coupling in longer scalelength plasmas; these experiments have also had limitations. Using underdense gas targets to eliminate complicating effects due to the presence of a critical surface, investigators have made positive identifications of stimulated Brillouin backscatter[1-4] and sidescatter[5] and of stimulated Raman scattering.[6] They have also observed the saturation of Brillouin backscatter[7-9] and sidescatter.[5] Measurements[4,10] and calculations[11] suggest that coupling to these plasmas is dependent upon the dynamics of ionization and heating waves, as well as upon the hydrodynamic expansion lateral to the

1

laser axis; thus, the dynamics of the gas target plasmas are as complicated as the dynamics of solid target plasmas but are less similar to the dynamics of reactor pellet plasmas. Furthermore, the scalelengths in these underdense gas targets are often so long that they can be treated by the theory of parametric instabilities in homogeneous plasmas; therefore, one does not check the inhomogeneous theory of relevance to reactor pellets. More recent experiments with inhomogeneous, overdense gas targets[12-14] overcome this latter problem. However, the important effect of the flow velocity gradient along the laser axis is still not present.

At NRL, longer-scalelength solid-target experiments in progress are designed to include effects of flow velocity gradients while overcoming the abovementioned deficiencies of standard solid-target experiments. To produce longer scalelength plasmas, two separate beams from our Nd laser ($\lambda = 1.054$ μm) may be focused in different planes, as shown in Fig. 2. One beam, operating with up to 250 J in a 3-5 ns pulse, is brought to a large diameter (≈ 1 mm) spot at the target to produce plasmas with density scalelengths $L_n \equiv n/\nabla n$ of 250-600 μm at $n_c/10$. The second beam is tightly focused inside the first to give the high intensities of interest for laser-plasma coupling experiments. By reducing the pulse duration of the second beam to $\tau_L < 0.5$ ns (with laser energies as high as 25 J), we can minimize the perturbation to the long-scalelength hydrodynamic flow of the first beam that is caused by this higher intensity region. Both high intensity and long scalelength can be achieved in these experiments, and the two parameters may be varied independently since the scalelength is determined by the larger spot size and the intensity by the smaller spot size. This new method for performing longer-scalelength coupling experiments has evolved from prepulse techniques pioneered by NRL in the mid-1970's.[15] As will be discussed later in this paper, we are developing new plasma diagnostic techniques to make improved measurements of density and temperature profiles, as well as the first measurements of velocity profiles.

II. PRELIMINARY LONGER-SCALELENGTH EXPERIMENTS

Preliminary observations of laser-plasma coupling have been made using this two-beam configuration to produce longer scalelengths. As indicated in Fig. 3, a significant increase in backscatter through the lens is observed when the large-focus beam is combined with the tightly focused beam; this occurs both for long pulselength and short pulselength operation of the higher intensity beam, although the maximum intensity achievable in the former case is lower due to laser protection considerations. Despite the large increase observed in backscatter from the carbon targets used in these experiments, the maximum backscatter is 10 percent; thus, the backscatter accounts for only a small fraction of the incident energy. Measurements of scattered light at other angles, which have not yet been reduced, may alter this picture.

While the increase in backscatter in these preliminary longer-scalelength experiments was entirely predictable from parametric instability theory,[16] two other observations are more surprising. Time-integrated images of second-harmonic emission, taken at 90° to the incident laser axis, are shown in Fig. 4. When a single high-intensity beam is focused on a carbon target, as in the left hand image, a localized region of copious $2\omega_0$ emission is observed. When this same high-intensity beam is incident upon the longer scalelength plasma set up by the large-focus beam, the intensity of the $2\omega_0$ emission is not detectable, as in the right-hand image.

The second surprising observation is in the x-ray emission. Time integrated spectra of 1-50 keV x-rays are obtained with arrays of PIN diodes and photomultiplier-scintillator detectors. With the single high-intensity beam incident upon a carbon target, x rays in the 10-50 keV spectral range are easily detected, as indicated in Fig. 5. However, with the same high-intensity beam incident upon the longer scalelength plasma, the intensity of x rays in this spectral region falls below detection thresholds (see Fig. 5). The upper bounds on the x-ray flux at 50 and 20 keV represent reductions from the single-beam case by factors of at least 30 and 1000, respectively! These reductions are consistent with observations made in longer-scalelength gas-jet targets at KMS.[14]

2

At least two explanations might be offered to account for the observations of $2\omega_0$ and energetic x ray emission. First, a longer scalelength near critical density may directly reduce the importance of resonance absorption; this could explain the disappearance of both $2\omega_0$ emission and high-energy x-rays, and would indicate that the experimental conditions are such that the relative importance of various absorption processes is changing. The observations may also be explained by a reduced laser intensity at the critical surface, due to increased inverse Bremsstrahlung absorption or Brillouin scatter in the underdense plasma. The increased reflectivity through the lens in these preliminary experiments is insufficient to account for this, but measurements of scattered light at other angles, which have not yet been reduced, may alter the picture.

III. PLASMA PROFILE MEASUREMENTS

As mentioned above, measurements of plasma density, temperature, and velocity profiles are at least as important in these experiments as measurements of absorbed energy, scattered light, and x rays. Without these measurements, scalelengths in hydrocodes may be varied to fit the experimental observations, and our confidence in the ability of these codes to extrapolate the physics correctly to reactor conditions is not increased.

To overcome the deficiency of previous coupling experiments, NRL is developing new methods for measurement of plasma profiles. All of these new methods have evolved from a technique presented at the 1981 Anomalous Absorption Meeting, which allowed the first visualizations of material flowlines from laser-irradiated targets.[17] We use a special target, as shown in Fig. 6, which has Al tracer dots embedded within a polystyrene (CH) substrate. Here, the dots are 25 μm in diameter and are spaced by 50 μm center-to-center. Regions of Al flow from each of the dots are easily identified as tracks of stronger emissivity in pinhole-camera images of x-ray emission above 1 keV, because the Al line emission in this spectral region is much stronger than either the C or H continuum emission.

Examples of flow visualizations obtained in this way are shown in Fig. 7. These three images, obtained with different-sized pinholes on a single shot, show tracks of stronger volume emissivity resulting from the Al dots. Images obtained with smaller pinholes provide better spatial resolution, while those obtained with larger pinholes give greater sensitivity and allow visualization of the flow further from the target. A more thorough treatment of the flow patterns may be found in Ref. 17; the one property relevant to the present discussion is the distinctness of the streamlines. Since these x-ray images are time-integrated over the 4-nsec x-ray pulsewidth (FWHM), the absence of smearing of the streamlines suggests that we are in a nearly steady flow regime. Further experimental evidence for this flow condition is obtained from streaked images of $3\omega_0/2$ emission, which imply a nearly stationary $n_c/4$ surface.[18]

If we are, in fact, in a steady flow regime, we may use the flow visualizations in conjunction with a measured density profile to infer the fluid velocity profile in the plasma. As indicated in Fig. 8, the method relies upon the steady-state mass conservation equation, which tells us that the product of the density n in a streamtube, the cross-sectional area A of the streamtube, and the fluid velocity v in the streamtube is a constant, C. If we measure the density profile by interferometry or some other technique, and we obtain the area A from the flow visualizations, we need only to evaluate the constant C in order to obtain absolute values for the velocity. (Relative values may be obtained without C.) Experimentally, we may obtain C by imposing a boundary condition far from the target where the velocity has reached a constant value; in this region, we equate the velocity with that measured far from the target by time-of-flight ion detectors.

Data from a proof-of-principle experiment have been reduced using this model, as shown in Fig. 9. The density profile obtained interferometrically shows a $1/z^2$ dependence of the density with distance z far from the target (bottom of Fig. 9). In this same region, the flow visualizations show a spherically divergent flow, giving A proportional to z^2. Since the product of density and area is constant in this region, the model of Fig. 8 implies that the flow velocity is constant (top of Fig. 9); it is in this

3

region that we equate the velocity to that measured in the far field by ion detectors. In closer to the target, the density variation changes and we begin to infer a change of the flow velocity from its far-field value. Interestingly, the region of nearly constant velocity extends inward approximately to the $n_c/10$ surface. This could explain the fact that Brillouin scatter from solid targets often seems to emanate from this lower density region[15]; velocity gradients may stabilize the Brillouin process at higher density. To infer the velocity profile for higher densities than 0.3 n_c, the limit of the $3\omega_0$ interferometric probe under these conditions, a technique for measuring the higher densities closer to the target is needed.

To access higher densities, we are developing an improved x-ray spectroscopic method, as illustrated in Fig. 10.[19] Here, a polystyrene target with a single embedded Al spot is used, but now the Al is serving as a localized source of x-ray line emission for spectroscopic diagnosis. The Al line radiation is collected by an imaging spectrograph with the entrance slit oriented to give spatial resolution along the laser axis. This technique has three major advantages over standard laser-plasma spectroscopy (where the target is entirely Al). First, emission is obtained only from a known volume within the plasma, rather than by integrating along the diagnostic line-of-sight through regions of differing density and temperature; thus, local measurements are made directly, without the need for deconvolution. Second, effects of plasma reabsorption of the emitted radiation are greatly reduced, particularly if a higher Z spot is embedded in a lower Z target; this simplifies interpretation of measured spectra. Third, the reduced size of the emitter leads to better spectral resolution because source broadening of the detected radiation is reduced.

To demonstrate this third point, data obtained with this new technique are compared with standard spectroscopic data in Fig. 11. In Fig. 11A, a set of pinhole images from an Al target show that a large volume of plasma participates in the x-ray emission, as one would expect. In contrast, pinhole images from a single-spot target show a well-confined channel of Al line emission within a larger-diameter region of plastic continuum emission, as seen in Fig. 11C. The result of this reduced emitter diameter is that better spectral resolution is seen in the spectrum obtained with a spotted target, in Fig. 11D, than is seen in the standard spectrum of Fig. 11B. More details on this new technique may be found in Ref. 19.

With this improved spectral resolution, one expects that better comparisons between data and spectroscopic models will be made and that these will lead to improved density and temperature measurements.[20] A standard technique for plasma density measurement relies upon the ratio between the He-like intercombination line (He 2^3P) and the He-like resonance line (He-α)[21]; the measured variation of this ratio with distance z from the target is shown in the left-hand graph of Fig. 12. Collisional-radiative equilibrium mode's indicate that this ratio should fall monotonically with increasing density except for plasma opacity effects very near to the target.[22] For $z \geqslant 200\ \mu$m, this expected behavior is observed and leads to the solid portion of the density profile curve in the right-hand graph of Fig. 12; this yields densities up to 0.5 n_c. For $z < 200\ \mu$m, we observe an apparent levelling off or even an increase in the He 2^3P/He-α ratio. At this time, we believe that this is due to interfering spectral lines which nearly underlie the He 2^3P line and increase relative to it as the density increases. In previous experiments, the spectral resolution was not sufficient to distinguish these from the intercombination line; with our greater spectral resolution, we are on the verge of resolving these lines. Were we to naively apply previous models to the apparently saturated line ratio, we would obtain a density shelf at 5×10^{20} electrons/cm^3 for $z < 200\ \mu$m. In fact, we believe the He 2^3P/He-α ratio continues to decrease, as indicated by the speculative dashed curve. This would imply higher densities, as shown by the dashed curve in the right-hand graph of Fig. 12; densities up to $2n_c$ should be accessible with this technique. We are currently working on eliminating the problem by using a more detailed model, which should result in reliable measurement of these higher densities.

For temperature determinations, we rely upon intensity ratios between He-like and H-like Rydberg lines. Intensity variations of three of the stronger lines with distance from the target are shown in the left-hand side of Fig. 12, and temperatures inferred from the ratios of these lines are shown in the

right-hand graph of the same figure. For $z < 200\,\mu$m, the temperatures are speculative because the inferred temperatures are dependent upon the inferred densities which are speculative at this region, as discussed above.

One final note concerns a new, untested idea to improve the velocity profile measurement. The method described earlier in Figs. 8 and 9 suffered from three drawbacks: (1) it required the assumption of steady state, (2) it required simultaneous measurement of the density profile, and (3) it gave only a time-averaged velocity profile. To overcome all three of these problems, we propose the use of layered tracer dots, as shown in Fig. 13. By making the tracer dot from alternating layers of two materials which have distinguishable x-ray emissivity, we should obtain a direct measure of the velocity profile with time resolution. We may follow the front of each of these layers as it transits the blowoff plasma by imaging the x rays onto the slit of a streak camera; the resultant z, t curve of the front directly measures the velocity profile. The time evolution of this profile is obtained from the multiple layers; each interface gives us the velocity profile at one time.

IV. STATUS REPORT

To summarize, studies of laser coupling in longer-scalelength plasmas which better simulate reactor plasmas are underway at NRL, as indicated in Fig. 14. Preliminary observations do show increased backscatter, as expected. The concomitant decrease in second-harmonic and high-energy x-ray emissions may indicate that we are entering a new physics regime where longer scalelengths are reducing the relative importance of resonance absorption.

Because we realize that these experiments are best used to benchmark the codes that are used for scaling to reactor-sized plasmas, we believe that measurements of plasma profiles are at least as important as measurements of laser-target coupling. We have demonstrated one technique and proposed a second improved technique for velocity profile measurement; these are the first techniques available for measurement of the velocity profile, which is important in evaluating parametric instability mechanisms. In addition, we have demonstrated an improved method for x-ray spectroscopic measurements, and we are developing the necessary improved models for extraction of plasma density and temperature. We hope to make more definitive statements on laser-coupling and profile measurements in longer-scalelength plasmas in the near future.

V. ACKNOWLEDGMENTS

REFERENCES

1. J.J. Turechek and F.F. Chen, Phys. Rev. Lett. **36**, 720 (1976).

2. R. Massey, K. Berggren, and Z.A. Pietrzyk, Phys. Rev. Lett. **36**, 963 (1976).

3. A.A. Offenberger, M.R. Cervenan, A.M. Yam, and A.W. Pasternak, J. Appl. Phys. **47**, 1451 (1976)

4. N.H. Burnett, H.A. Baldis, G.D. Enright, M.C. Richardson, and P.B. Corkum, J. Appl. Phys. **48**, 3727 (1977)

5. M.J. Herbst, C.E. Clayton, and F.F. Chen, J. Appl. Phys. **51**, 4080 (1980).

6. R.G. Watt, R.D. Brooks, and Z.A. Pietrzyk, Phys. Rev. Lett. 41, 170 (1978).

7. A. Ng, L. Pitt, D. Salzmann, and A.A. Offenberger, Phys. Rev. Lett. 42, 307 (1979).

8. M.J. Herbst, C.E. Clayton, and F.F. Chen, Phys. Rev. Lett. 43, 1591 (1979).

9. Z.A. Pietrzyk and T.N. Carlstrom, App. Phys. Lett. 35, 681 (1979).

10. M.J. Herbst, C.E. Clayton, W.A. Peebles, and F.F. Chen, Phys. Fluids 23, 1319 (1980).

11. N.H. Burnett and A.A. Offenberger, J. Appl. Phys. 45, 2155 (1974).

12. F.J. Mayer, G.E. Busch, C.M. Kinzer, and K.G. Estabrook, Phys. Rev. Lett. 44, 1498 (1980).

13. A.A. Offenberger and A. Ng, Phys. Rev. Lett. 45, 1189 (1980).

14. J.A. Tarvin, F.J. Mayer, D.C. Slater, G.E. Busch, G. Charatis, T.R. Pattinson, R.J. Schroeder, and D. Sullivan, Phys. Rev. Lett. 48, 256 (1982).

15. B.H. Ripin and E.A. McLean, Appl. Phys. Lett. 34, 809 (1979) and references contained therein.

16. C.S. Liu, M.N. Rosenbluth, and R.B. White, Phys. Fluids 17, 1211 (1974).

17. M.J. Herbst and J. Grun, Phys. Fluids 24, 1917 (1981).

18. M.J. Herbst, J.A. Stamper, R.H. Lehmberg, R.R Whitlock, F.C. Young, J. Grun, and B.H. Ripin, to appear in Proceedings of the 1981 Topical Conference on Symmetry Aspects of Inertial Fusion Implosions, ed. by S. Bodner, NRL.

19. M.J. Herbst, P.G. Burkhalter, R.R. Whitlock, J. Grun, and M. Fink, NRL Memorandum Report 4812, 1982 (to appear in Rev. Sci. Inst.).

20. P.G. Burkhalter, M.J. Herbst, D. Duston, R.R. Whitlock, and J. Grun, Proceedings of 1982 IEEE International Conference on Plasma Science and NRL Memorandum Report (to be published).

21. V.A. Boiko, S.A. Pikuz, and A. Ya. Faenov, J. Phys. B 12, 1889 (1979).

22. D. Duston and J. Davis, Phys. Rev. 21A, 1664 (1980).
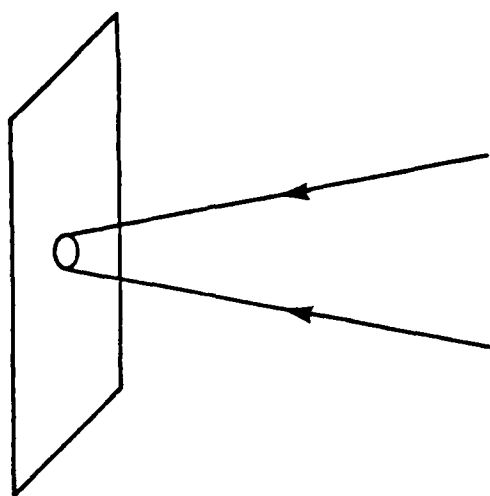
$$E \leqslant 250J$$
$$t = 3\text{-}5 \text{ ns}$$
$$f/6, \ d_{50} \approx 80\mu m$$
$$I \leqslant 10^{15} \text{ W/cm}^2$$
$$L_n \ (n_c/10) \leqslant 200\mu m$$

Fig. 1 — Standard arrangement for laser-coupling experiments uses a tightly focused beam to achieve high intensity. At NRL, a single beam with 250 J in 3-5 ns can be focused to 80 μm diameter spot (50% energy content) by an f/6 lens, giving incident intensities up to 10^{15} W/cm^2. In this case, plasmas can be generated with density gradient scalelengths at $n_c/10$ which just exceed 200 μm.
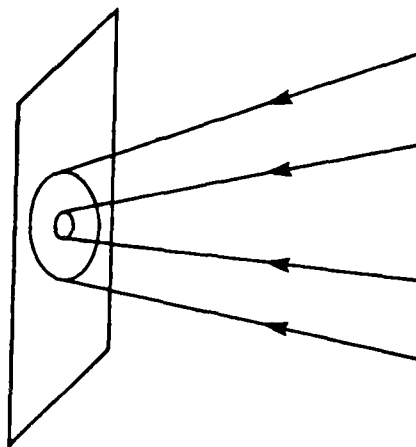
Fig. 2 — Novel configuration of two-beam laser allows production of longer-scalelength plasmas for coupling experiments. One beam with 3-5 nsec pulselength is brought to large focal diameter ($\simeq 1$ mm) to produce longer scalelengths ($L_n \simeq 250$-600 μm at $n_c/10$), while a second beam is tightly focused within the first to produce higher intensities of interest. The pulselength of the high-intensity beam may be shortened to minimize its perturbation to the long-scalelength flow.

3-7 FOLD BACKSCATTER INCREASES

AT MID-10^{13} (5 ns) AND MID-10^{14} (<0.5 ns)

WHEN LARGE-FOCUS BEAM PRESENT

Fig. 3 — Summary of preliminary backscatter observations.

$2\,\omega_o$ IMAGES:
STANDARD vs. LONGER SCALELENGTH

1 mm

(11938)   (11940)

STANDARD
$\tau_L < 0.5$ns

LONGER
SCALELENGTH
$\Delta t = 5.4$ns
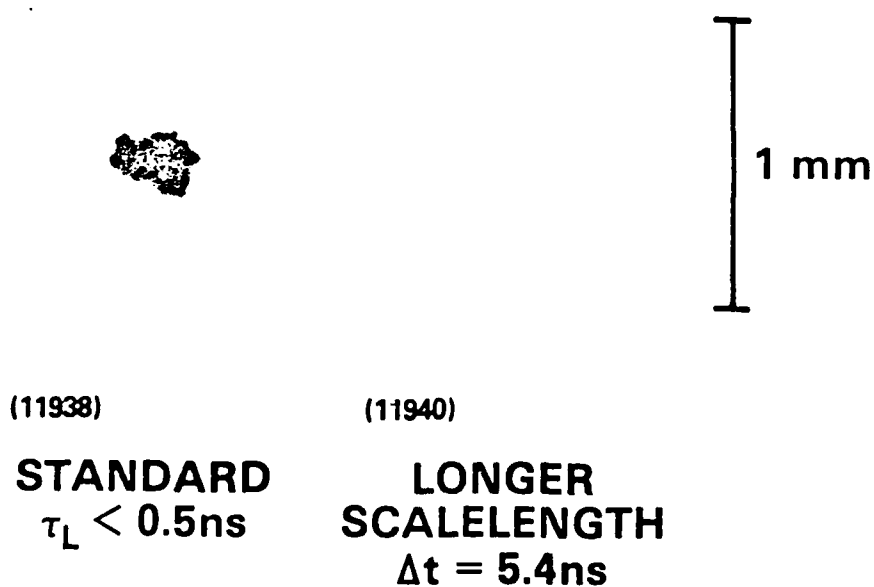
Fig 4 — Comparison of time-integrated images of second harmonic emission for two modes of operation. The laser is incident from the left and the images are negatives. With a single high-intensity beam, the image on the left shows copious $2\omega_0$ emission. When the same high-intensity beam is focused into a longer-scalelength plasma, as shown in Fig 2, the $2\omega_0$ emission disappears. The delay of the short-pulse, high intensity beam is 5.4 nsec after the peak of the longer pulse

9

HIGH-ENERGY X-RAYS:
STANDARD vs. LONGER SCALELENGTH
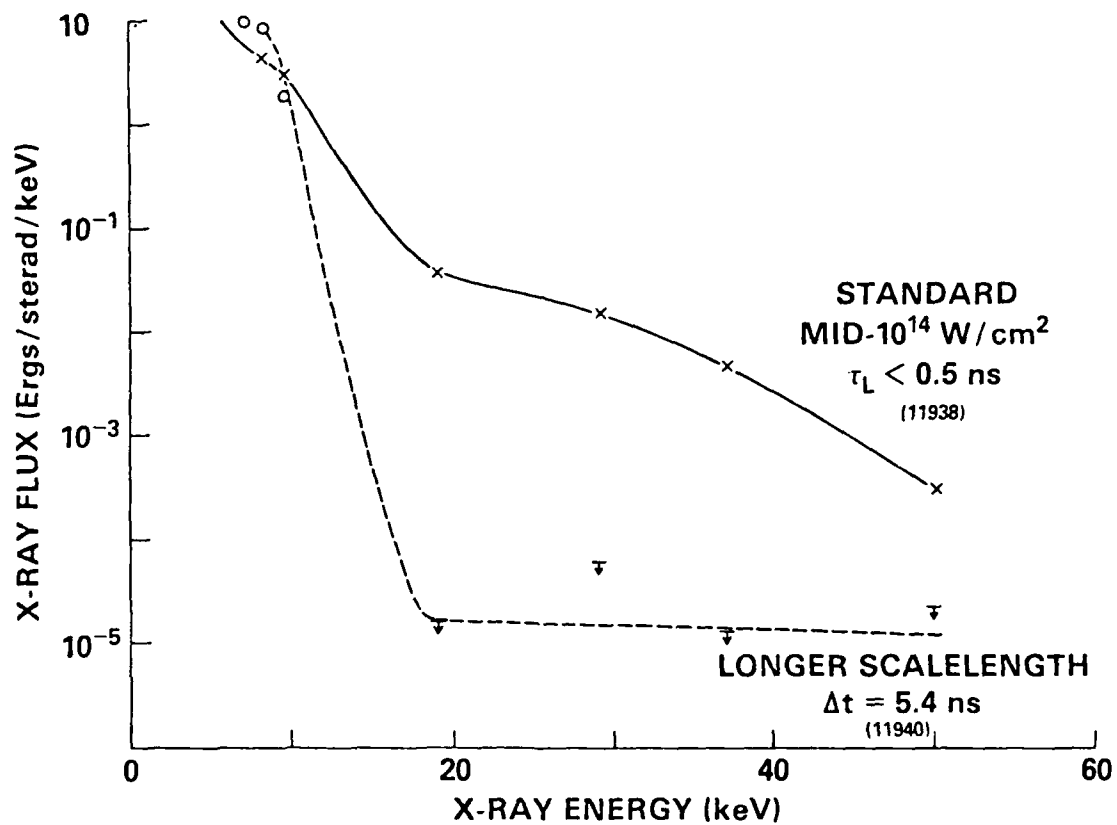
Fig 5 — Comparison of high-energy x-ray spectra for two modes of operation. With a single, short-pulse, high-intensity beam, an x-ray tail corresponding to $T_h \approx 7$ keV is observed. This tail falls below the detection threshold for a long-scalelength target plasma. The delay of the short-pulse, high-intensity beam is 5.4 nsec after the peak of the longer pulse.

CH TARGET

AI DOTS

LASER
LIGHT CONE

X-RAY PINHOLE CAMERA
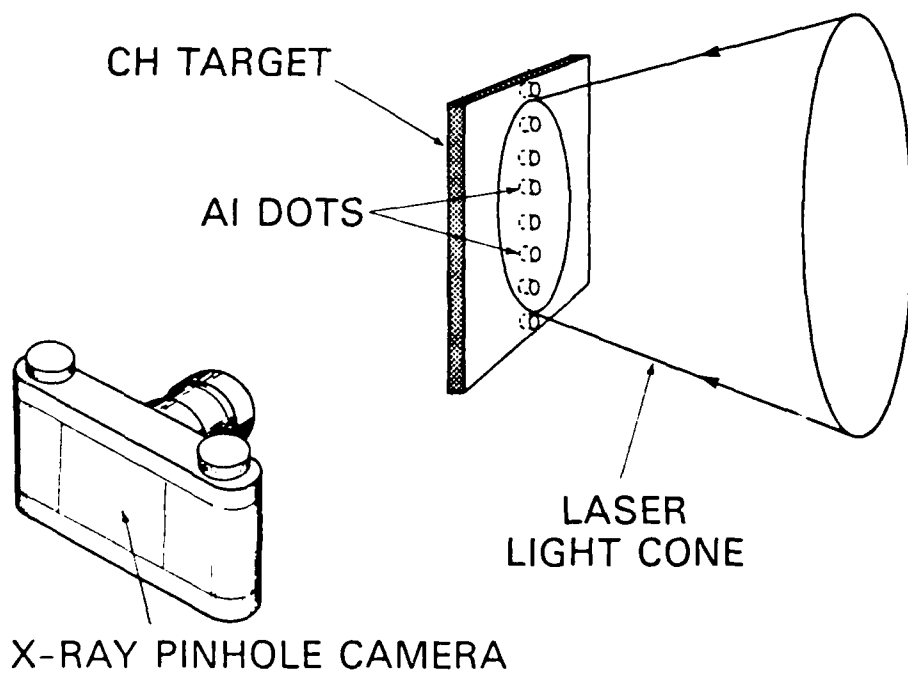
Fig. 6 — Schematic illustration of the experimental arrangement for visualization of hydrodynamic flows.
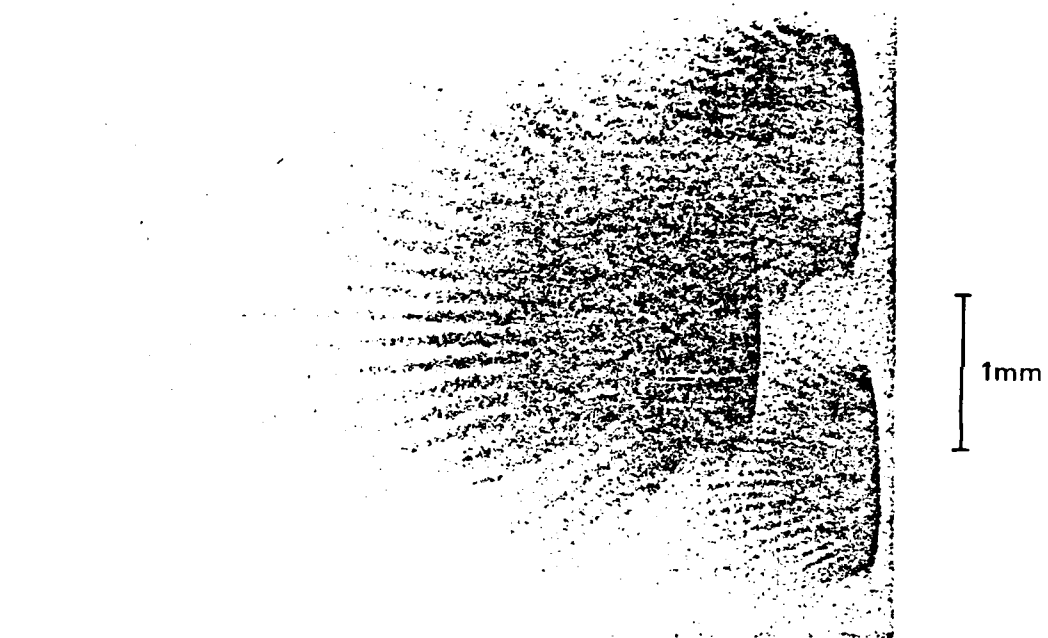
Fig 7 — Time integrated images of x-ray emission obtained for single laser shot with 13, 28, and 54 μm diameter pinholes. Laser is incident from left, and images are negatives. Camera filter is nominally 15 μm thick Be. 230 J of laser energy is focused to 940 μm diameter spot (90° energy content) to give $I_0 = 8 \times 10^{12}$ W/cm² on 50 μm thick CH target.

STEADY-STATE MASS CONSERVATION

$$n\,A\,v = \text{constant, } C$$

$$v = \frac{C}{nA}$$

BOUNDARY CONDITION:
v_∞ FROM TIME-OF-FLIGHT DETECTORS

Fig. 8 — Model for inferring fluid velocity profile.

DENSITY AND FLOW VELOCITY
PROFILES BELOW 0.3 n_c

$E_L = 35J$ $d_{90} \cong 650\mu m$ $I_{90} \cong 2 \times 10^{12}$ W/cm^2 $d_{plasma} \cong 620\mu m$
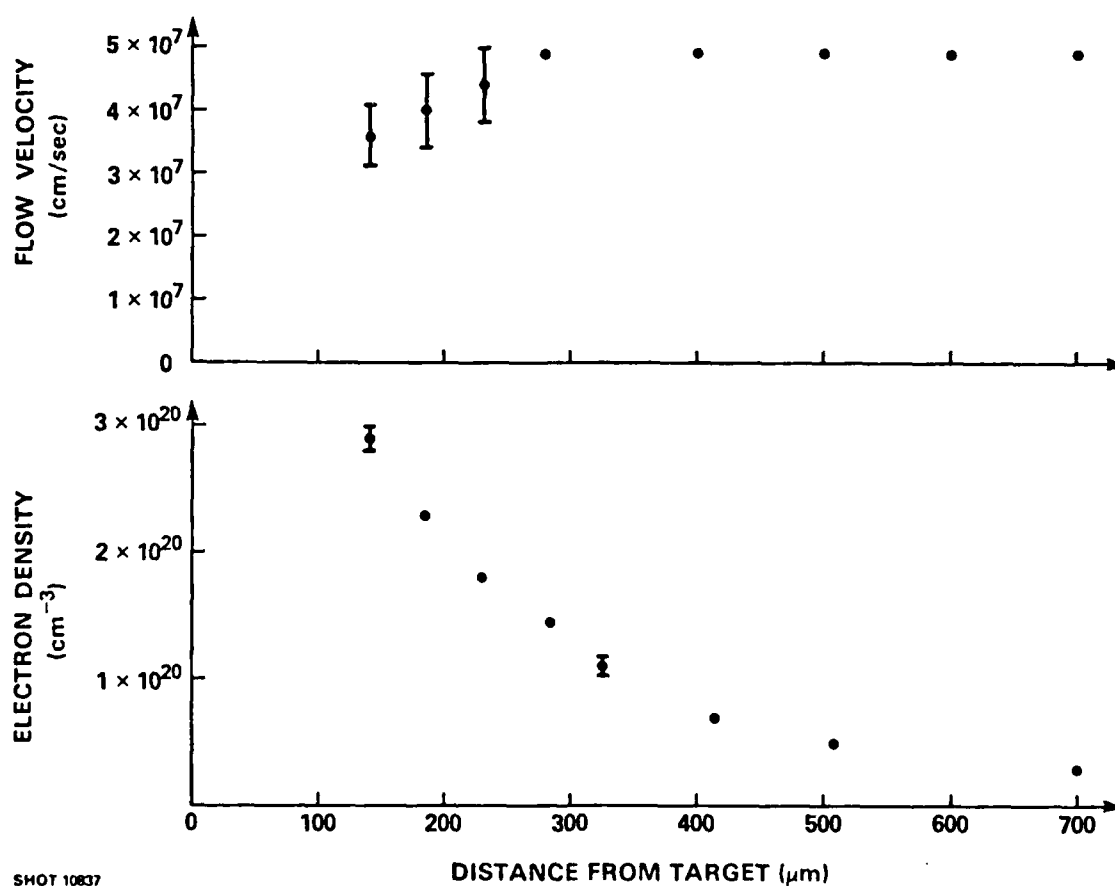
SHOT 10837

Fig. 9 — Sample of data reduced using model of Fig. 8. Density profile is obtained interferometrically with short-pulse ($\tau_L < 0.5$ ns) $3\omega_0$ probing beam

14

EMBEDDED A*l* SPOT

IMAGING
SPECTROGRAPH

LASER FOCAL SPOT
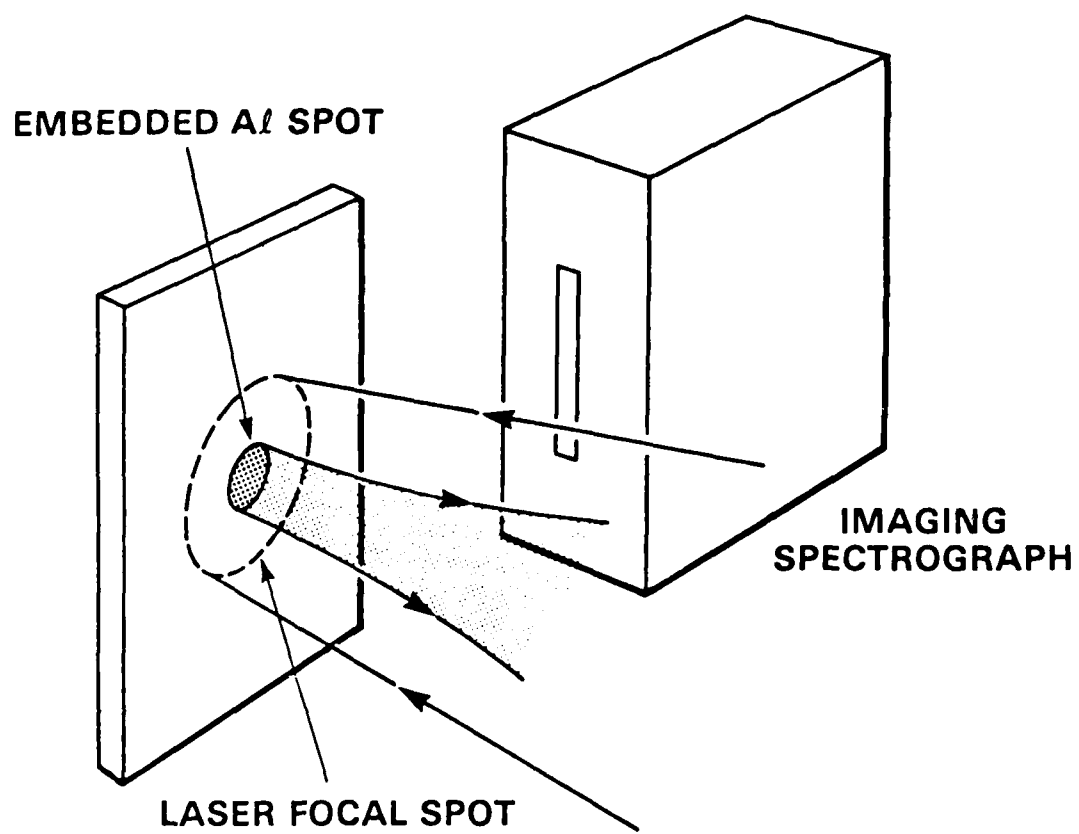
Fig 10 — Experimental arrangement for spot spectroscopy

15

(A)

(B)

1mm

500μm

λ(Å) 6   7   8

1mm

500μm

(C)

(D)
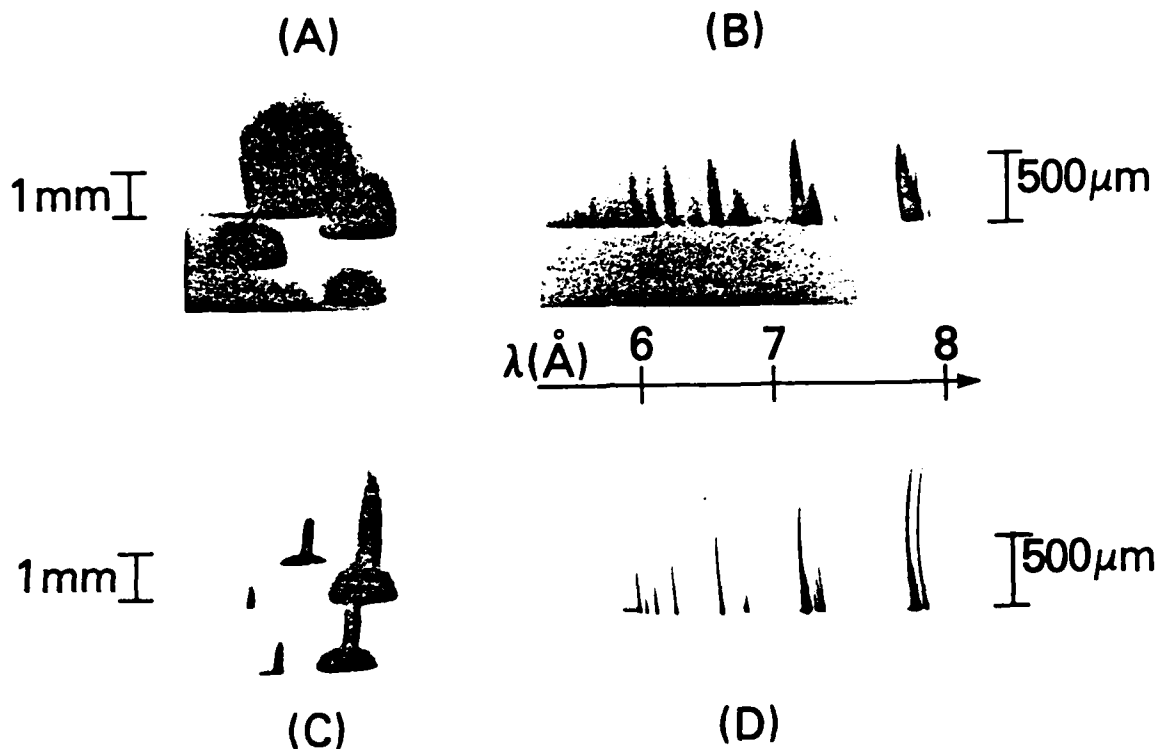
Fig. 11 — Qualitative comparison between data obtained with Al foil target and data acquired using CH plastic target locally embedded with Al. the vertical axis for (A) through (D) corresponds to the laser axis, with the laser incident from above and the target surface at bottom. (A) is obtained with Kodak 3490 film, and (B) through (D) are on Kodak No-Screen Film. (A) X-ray pinhole camera images, obtained with an array of pinholes (5-55 μm diameter), for an Al foil target. Laser intensity $I_0 = 3 \times 10^{12}$ W/cm², due to 100 J focused to 1100 μm diameter spot (90% energy content). (B) Spectrum obtained for Al foil target at $I_0 = 8 \times 10^{12}$ W/cm², with 110 J focused to 600 μm diameter spot. (C) Pinhole images as in (A), but for CH target embedded with 180 μm diameter Al spot. 225 J of laser energy focused to 900 μm diameter spot yields $I_0 = 8 \times 12^{12}$ W/cm². (D) Spectrum from same shot as (C).

16

n_e AND T_e FROM Al-SPOT SPECTROSCOPY
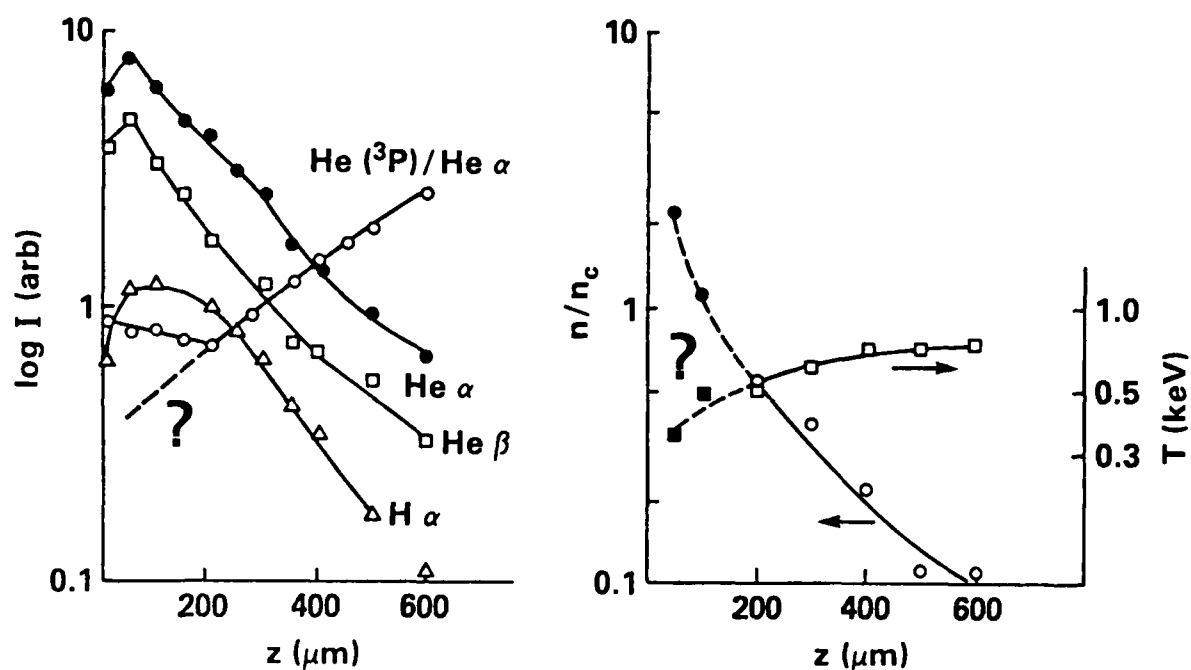
$I_{90} \approx 7.3 \times 10^{12} W/cm^2 \quad d_{90} \approx 1mm \quad E = 273J \quad \tau_L = 4ns$ (11505)

Fig. 12 — Preliminary reduction of spot spectroscopy data. Left-hand graph shows spatial variation of intensities of He-like α and β lines and of H-like α line, as well as of ratio of He-like intercombination to resonance lines. Right-hand graph shows density and temperature information extracted from line ratios within spectrum. Note that dotted portions of density and temperature profiles are based upon speculative extrapolation of He ^{3}P/Heα ratio shown in graph at left.

17

LASER FOCAL SPOT
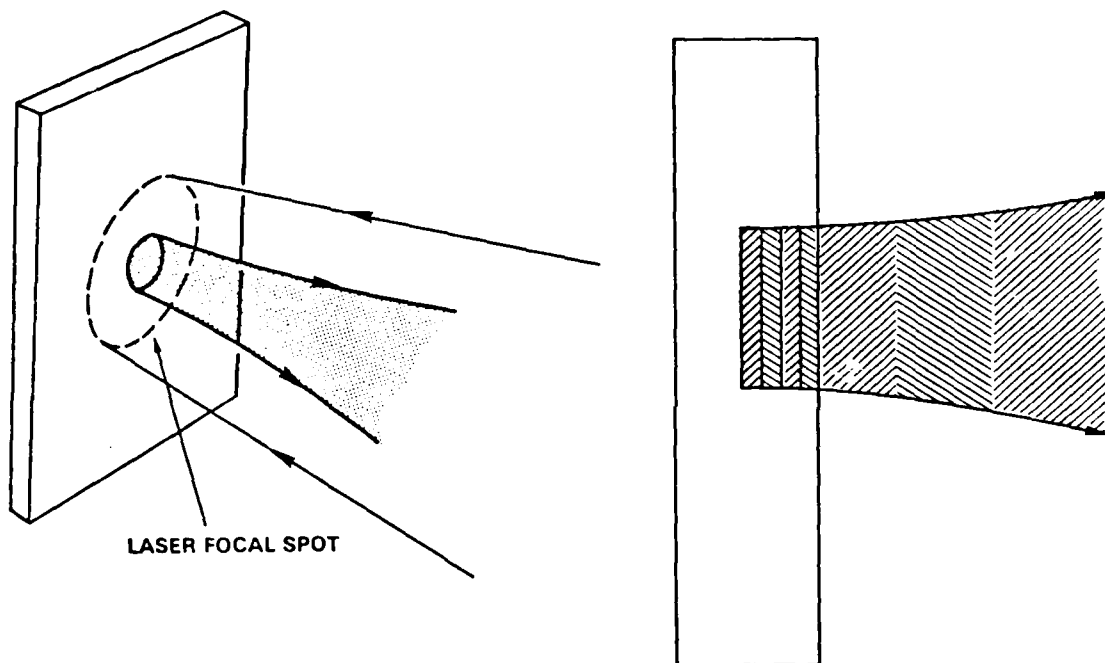
Fig. 13 — New idea for time-resolved measurement of velocity profile. Illustration at left shows that we use laterally localized tracer, as per spot spectroscopy technique. Cross-section of target at right, however, shows that embedded spot is now made of alternating layers of two materials, which ablate sequentially in time during laser irradiation.

18

STATUS REPORT

I. LONGER-SCALELENGTH EXPTS.
UNDERWAY

- INCREASED BACKSCATTER
- DECREASED 2 ω_o & HIGH-ENERGY
  X-RAYS

II. DIAGNOSTIC DEVELOPMENT
CONTINUING

- FIRST TECHNIQUES FOR V PROFILE
- SPOT SPECTROSCOPY FOR n, T

Fig. 14 — Summary of work-to-date.

APPENDIX L

REPORT DOCUMENTATION PAGE		READ INSTRUCTIONS BEFORE COMPLETING FORM
1 REPORT NUMBER NRL Memorandum Report 5003	2 GOVT ACCESSION NO.	3 RECIPIENT'S CATALOG NUMBER
4 TITLE (and Subtitle) NEW MEASUREMENT TECHNIQUES USING TRACERS WITHIN LASER-PRODUCED PLASMAS		5 TYPE OF REPORT & PERIOD COVERED Interim report on a continuing NRL problem.
		6 PERFORMING ORG. REPORT NUMBER
7. AUTHOR(s) M.J. Herbst, P.G. Burkhalter, D. Duston, M. Emery, J. Gardner, J. Grun*, S.P. Obenschain, B.H. Ripin, R.R. Whitlock, J.P. Apruzese and J. Davis		8 CONTRACT OR GRANT NUMBER(s)
9. PERFORMING ORGANIZATION NAME AND ADDRESS Naval Research Laboratory Washington, DC 20375		10 PROGRAM ELEMENT, PROJECT, TASK AREA & WORK UNIT NUMBERS DOE AI08-79DP 40092(172); 47-0859-0-3; DNA 62715H; 47-1606-0-3
11. CONTROLLING OFFICE NAME AND ADDRESS U. S. Department of Energy Washington, DC 20545		12. REPORT DATE January 6, 1983
		13. NUMBER OF PAGES 35
14. MONITORING AGENCY NAME & ADDRESS(If different from Controlling Office)		15. SECURITY CLASS. (of this report) UNCLASSIFIED
		15a. DECLASSIFICATION/DOWNGRADING SCHEDULE

16. DISTRIBUTION STATEMENT (of this Report)

Approved for public release; distribution unlimited.

17. DISTRIBUTION STATEMENT (of the abstract entered in Block 20, If different from Report)

19. KEY WORDS (Continue on reverse side if necessary and identify by block number)

Plasma diagnostics
Laser-plasma interactions
X-ray spectroscopy

Fluid flow visualization
Rayleigh-Taylor instability

20. ABSTRACT (Continue on reverse side if necessary and identify by block number)

The use of locally embedded tracers within laser-irradiated solid targets has led to a new class of diagnostic methods for laser-produced plasmas. Demonstrated uses of tracers include the first visualizations of hydrodynamic flow of laser-ablated material and improved spectroscopic measurements of plasma density and temperature profiles; comparisons with a two-dimensional hydrodynamics computer code are shown. Proposed future uses of tracers include the first measurements of fluid velocity profiles and improved determinations of mass ablation rates.

DD , FORM JAN 73 1473   EDITION OF 1 NOV 65 IS OBSOLETE
S/N 0102-014-6601

18. *Supplementary Notes (Continued)*

This paper was prepared for presentation at the Sixth International Workshop on Laser Interaction and Related Plasma Phenomena held in Monterey, CA on October 25—29, 1982.

CONTENTS

NEW MEASUREMENT TECHNIQUES USING TRACERS
WITHIN LASER-PRODUCED PLASMAS

I.   INTRODUCTION

Many of the physical processes which are important to the ablative-compression approach to laser-pellet fusion are intimately related to plasma density, temperature, and velocity profiles. Inverse bremsstrahlung absorption and parametric instabilities are closely coupled with underdense plasma profiles. Similarly, energy transport between the critical density surface and the ablation surface is interrelated with overdense plasma profiles. Therefore, laser-plasma interaction experiments can better address these physics issues if they include measurements of the plasma profiles. If experiments are performed in planar rather than spherical geometry, the problem becomes two-dimensional since the plasma profiles and the above-mentioned physical processes are affected by lateral flow of energy out of the finite focal spot. One then desires measurements of the area over which the absorbed energy is distributed and, if possible, of both axial and lateral profiles.

A new genre of diagnostic methods is being developed at the Naval Research Laboratory to address these and other problems. The unique feature of these new methods is the use of tracer materials which are locally embedded into the solid target to be irradiated. Tracers which are localized within the focal region remain localized within the blowoff plasma, due to the collisional or fluid nature of the flow of material ablated from the target. By imaging characteristic radiation from a linear array of such tracer dots, we have demonstrated the first visualizations of the hydrodynamic flow of material within laser produced plasmas;[1] this technique and its applications are discussed in Sec. II. As described in Sec. III, improved measurements of plasma density and temperature profiles have also been demonstrated, by using the tracer dots as local sources of spectroscopic diagnostic lines.[2] Comparisons with these measurements provide the most direct calibration of hydrodynamics computer codes, because plasma profiles are the experimental observables most closely coupled to mechanisms of energy absorption and transport in laser-produced plasmas. Therefore, comparisons between experiments and the Naval Research Laboratory hydro-codes are found throughout Secs. II and III. In Sec. IV, the use of layered tracer spots is proposed for time-resolved measurements of fluid velocity profiles[3] and for improved measurements of mass ablation rates.

II.   FLUID FLOW VISUALIZATIONS AND THEIR USES

The simplest use of tracer dots is for visualization of the hydrodynamic flow of material from the laser irradiated target, for which the experimental arrangement is as shown in Fig. 1. The distinguishing feature of this configuration is the target: thick polystyrene $[(CH)_x]$ with a linear array of 25 μm diameter, aluminum tracer dots. These dots are embedded so that their initial surfaces are flush with that of the surrounding target, and their thicknesses are chosen to exceed the expected ablation depth on any given shot. With the tracer spots aligned to fall along a diameter of the laser-irradiated region, between 10 and 500 J of Nd-laser energy (λ = 1.054 μm) is brought onto the target in a 3-5 nsec pulse. A camera with an array of pinholes is used to obtain time-

1

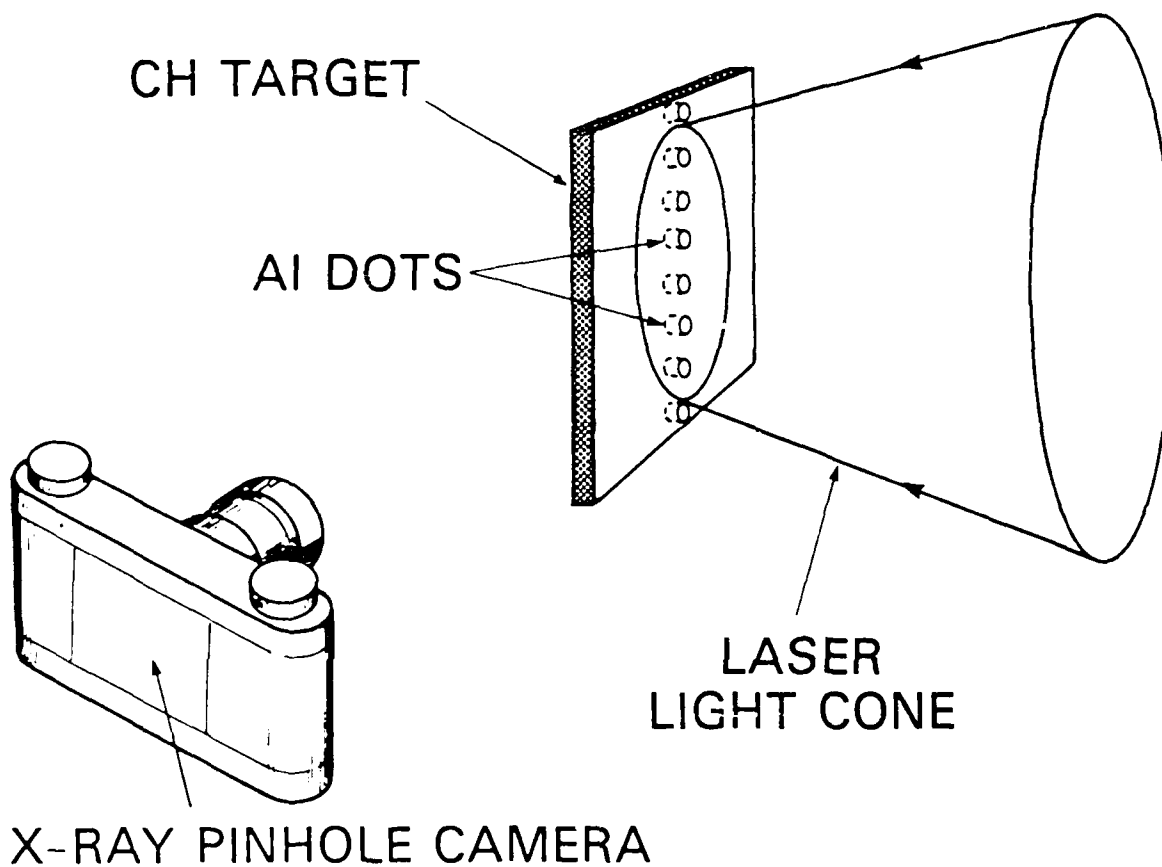CH TARGET

AI DOTS

LASER
LIGHT CONE

X-RAY PINHOLE CAMERA

Fig. 1   Experimental configuration for visualization of hydrodynamic flow.

2

integrated images of x-ray emission at 90° to the target normal. The 15 μm beryllium filter used on the camera allows imaging of photons with energy $h\nu > 1$ keV. Since aluminum line emission is more intense than carbon or hydrogen continuum emission in the spectral band of the pinhole camera, streamlines of material flowing from the aluminum spots are identifiable as tracks of strong x-ray emission in the images (see Fig. 2).

Flow visualization experiments have been performed at a variety of laser focal conditions with incident intensities I_{90} (averaged within the 90% energy-content diameter d_{90}) between 10^{12} and 2×10^{14} W/cm^2. On each shot. a series of laser isointensity patterns is recorded in an equivalent focal plane to that of the target,[4] with a factor of 2.2 in intensity between successive patterns. From these records, we may plot focal intensity distributions, such as those shown in Fig. 3. (These one-dimensional profiles represent azimuthal averages of the real two-dimensional profiles of the laser; these are used as input to the hydro-codes.) Note that the focal distribution near best focus of our f/6 lens is qualitatively different from that in the quasi-near field. The most obvious difference is near the center of the distribution, where large focal spots tend to exhibit local minima in intensity. Equally important, however, are differences in the wings of the distributions, as will be discussed in Sec. II.B. It should also be noted that intensities I_{50} (averaged over 50% energy content diameter d_{50}) and I_{pk} (peak intensity) tend to be higher than I_{90} by factors of 2 and 4, respectively.

While we have not conclusively demonstrated that the presence of the tracers does not perturb the visualized flow, there is some evidence that the perturbation should be minimal. First, the fully ionized mass densities for Al and $(CH)_x$ differ by only 12% at a given electron density in the blowoff plasma. Moreover, the average velocity of ablated ions as determined by Faraday cups is the same for the two materials.

In the following sections, the various physics issues that may be addressed by flow visualization methods are discussed. The shape of the visualized flows, as shown in Sec. II.A, is related to the outward hydrodynamic flow of plasma, and provides a valuable check for the hydrodynamics codes. In Sec. II.B, we present the observed sizes of the fluid sources under various irradiation conditions; this should indicate the degree to which absorbed laser energy spreads laterally as it flows inward from the absorption region to the ablation region near the edges of the focal spot. Lateral energy transport can also be important near the center of the focal spot if the irradiation there is nonuniform.[5,6] Flow visualizations obtained with intentionally perturbed laser beams qualitatively show this effect,[6] as described in Sec. II.C. Another proposed application for these flow visualizations, outlined in the final section, is for diagnosis of the Rayleigh-Taylor instability.[7]

A. Shape of the Visualized Flows

While the size of the observed fluid source varies with laser intensity and spot size, the shape of the flow pattern seems to be remarkably constant. As shown in Fig. 2, streamlines curve away from the
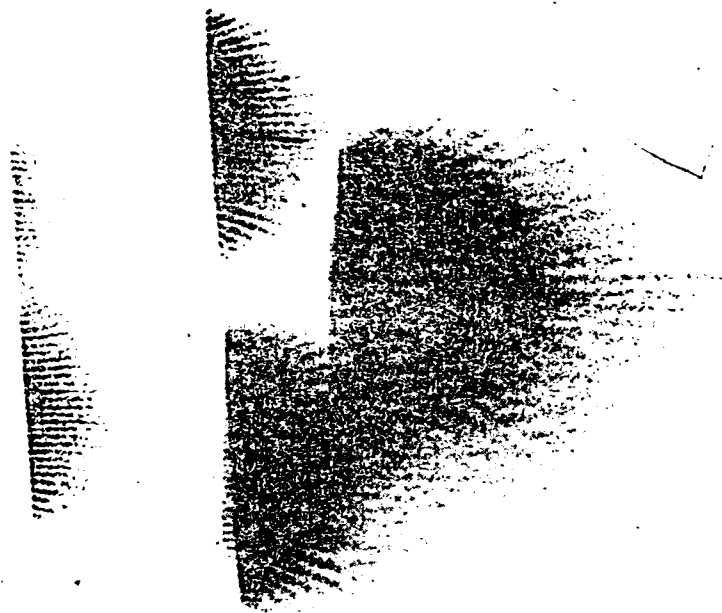
R-586

Fig. 2 Five flow visualizations obtained on a single shot with 5, 9, 13, 28, and 54 μm diameter pinholes. The laser is incident from the right, and the target surface is to the left. $I_{90} \simeq 3.2 \times 10^{12}$, $d_{90} \simeq 1470$ μm, and the laser energy is 212 J.
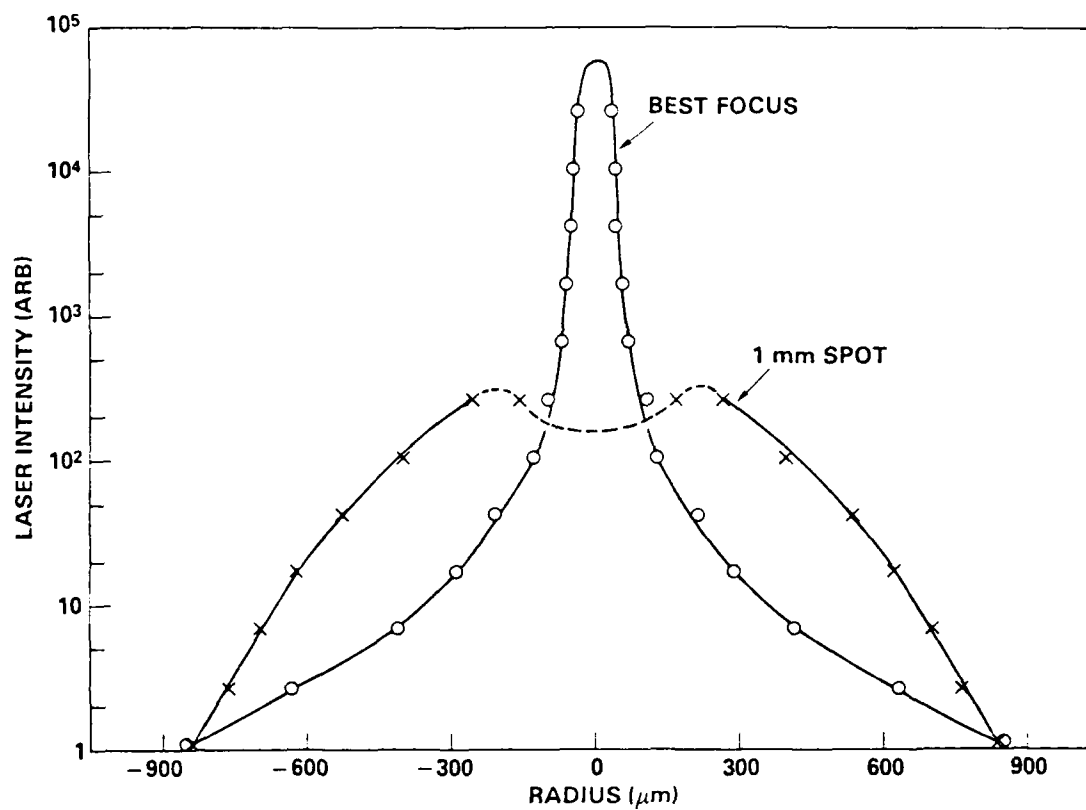
4

Fig. 3 Azimuthally averaged laser energy profiles for best focus of our f/6 lens and position in the quasi-near field where $d_{90} \approx 1075$ μm.

target normal at a rate which depends upon r/r_0, where r is the displacement of a given streamline from the center of the fluid source and r_0 is the radius of the fluid source. Each streamline attains a constant direction within a distance $z = r$ from the target surface; beyond $z = r_0$, all streamlines are following straight-line paths corresponding to a far-field, spherically diverging flow.

The shape of the visualized flows is in good agreement with NRL's two-dimensional hydrodynamics codes. As shown in Fig. 4, the measured streamline angles θ relative to the target normal are well predicted by a cylindrical (r and z) hydrodynamics simulation of the experiment. The computer model, described elsewhere in these proceedings,[8] uses a sliding-grid Eulerian mesh with flux-corrected transport, classical $T^{5/2}$ thermal conduction, and inverse bremsstrahlung absorption. The calculation uses the measured laser pulse duration and an azimuthal average of the measured laser focal distribution (such as those in Fig. 3). The slight asymmetry of the experimental data about $r = 0$ is a gentle reminder that real laser profiles are not perfectly symmetric, but prohibitively expensive, three-dimensional codes would be required to accurately simulate such focal nonuniformities. While Fig. 4 shows agreement at one distance z from the target, sets of such plots at varying z convince us that the code is correctly calculating the shape of the flow.

The fluid nature of the flow is not surprising, since the plasma radii are much greater than the ion-ion collision mean free path. The fact that time-integrated flow visualizations compare well with snapshots of the code, as in Fig. 4, suggests that we may also have a nearly steady flow; this is not entirely unreasonable, since the laser pulse length exceeds the acoustic transit time across a plasma radius. Experimental evidence that the flow is nearly steady, at least during the period of maximal x-ray emission, is obtained from streak photography of images of $3/2\omega_0$ emission from the $n_c/4$ surface.[9] The position along the laser axis of this surface appears relatively stationary for the duration of the $3/2\omega_0$ emission, a period of up to 3 nsec near the time of peak laser intensity.

The shape of the flow affects far-field particle diagnostics such as ion collectors or plasma calorimeters. First, the angular distribution of ablated mass observed by these diagnostics may be determined by the collisional flow near the target, which imparts a fluid velocity direction to each fluid element. As the material drifts through the collisionless region further from the target, some lateral spreading of material results from random thermal motions; since directed ablation velocities are generally much greater than ion thermal velocities, this should not greatly increase the angular range set by the fluid flow. Indeed, charge collector and plasma calorimeter measurements indicate that half of the ablated mass appears in a cone about the target normal with a 40° half-angle;[10] this is consistent with the angular spread inferred from flow visualizations.

Ion detectors are further affected because the flow, except for any smearing due to thermal expansion in the collisionless region, maps different regions of target surface into different diagnostic solid angles. A single ion detector at a specific angle far from the target then

VECTOR FLUID FLOW AT Z = 85 μm
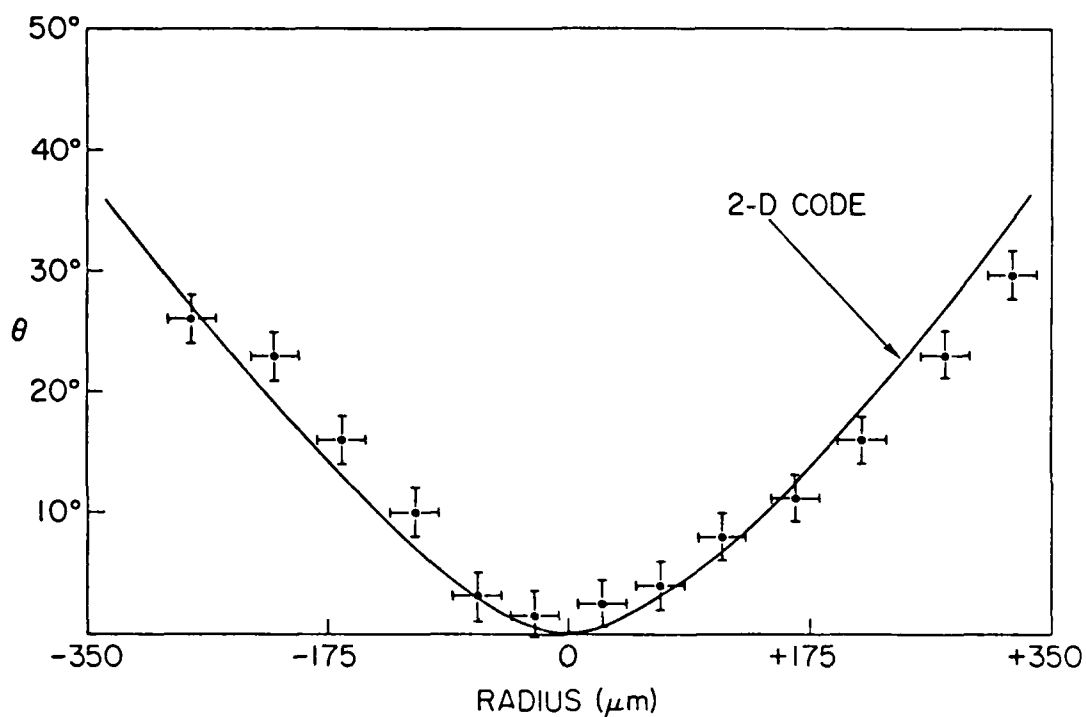## 2-D CODE vs EXPERIMENT

Fig. 4 Comparison between measured and calculated streamline angles θ relative to the target normal as functions of the radial displacement from the center of the flow. Values are taken at one distance z = 85 μm from the target surface. The calculation uses measured experimental conditions: $I_{90} = 2 \times 10^{12}$ W/cm^2, $d_{90} = 650$ μm, laser energy is 35 J.

samples only a portion of the irradiated region. To measure parameters averaged over the focal spot, one should use an array of detectors at a range of angles. The error that may result if too few detectors are used depends upon the uniformity of the laser illumination at the target, the ratio of the directed ablation velocity to the ion thermal velocities, and the solid angle subtended by the detectors used.

B.   Sizes of the Visualized Flows

The sizes of the visualized flows are well-defined and useful observables. From the flow visualizations, we define the fluid source size to be the diameter of the region at the target surface from which streamlines are seen to emanate. This quantity does have physical significance; as discussed below, it most likely reflects the diameter within which the plasma temperature is high enough for excitation of Al K-lines. It is also a well-defined quantity, in the sense that it is not extremely sensitive to the size of pinhole used to detect the x-rays. As seen in Fig. 2, the same number of streamlines is observed in the three largest pinhole images, despite a factor of 17 variation in pinhole collection efficiency. This may indicate the rapidity with which the temperature is falling at the edge of the x-ray images. The advantage of this observable over the size of standard pinhole images lies mainly in the ease of observation. The size of standard images is usually sensitive to pinhole size. In order to define a plasma size, one must densitometer the images, deconvolve the pinhole size, and invert the data to obtain isointensity contours of x-ray emission.

The observed fluid source diameter d_0 varies with laser intensity and spot size. As indicated in Fig. 5, d_0 increases with laser energy at fixed spot size and increases with spot size at fixed laser energy. One interesting observation is that the sensitivity of d_0 to laser energy is greater for the smaller focal spot sizes. Several possible explanations exist for such an observation: there is the potential effect of higher lateral thermal conductivity, which could result from higher plasma temperatures at the higher intensities, as well as the possibility of increased lateral flow due to fast electrons. A closer look at the shapes of the wings of the laser focal distributions in Fig. 3 suggests another explanation. By locating the position within the focal distributions at which a given intensity occurs and plotting the variation of that position with increasing laser energy, we generate curves such as shown in Fig. 5. Within experimental uncertainty (approximately a factor of 2), the intensity for both curves shown in Fig. 5 is 2×10^{11} W/cm^2. The correlation with the data points suggests that the edge of the fluid source consistently occurs at that particular intensity in the wings of the laser focal distribution. This could be explained by the existence of a threshold intensity for heating to a temperature at which the Al K-lines are excited; this heating could be directly due to laser energy deposition or could be due to laser heating to a temperature at which the thermal conductivity allows lateral transport of energy from higher intensity regions. It is not likely that intensity thresholds for ionization of the target play any role in determining the fluid source size, since the two-dimensional hydrodynamics codes calculate the flow pattern correctly (see
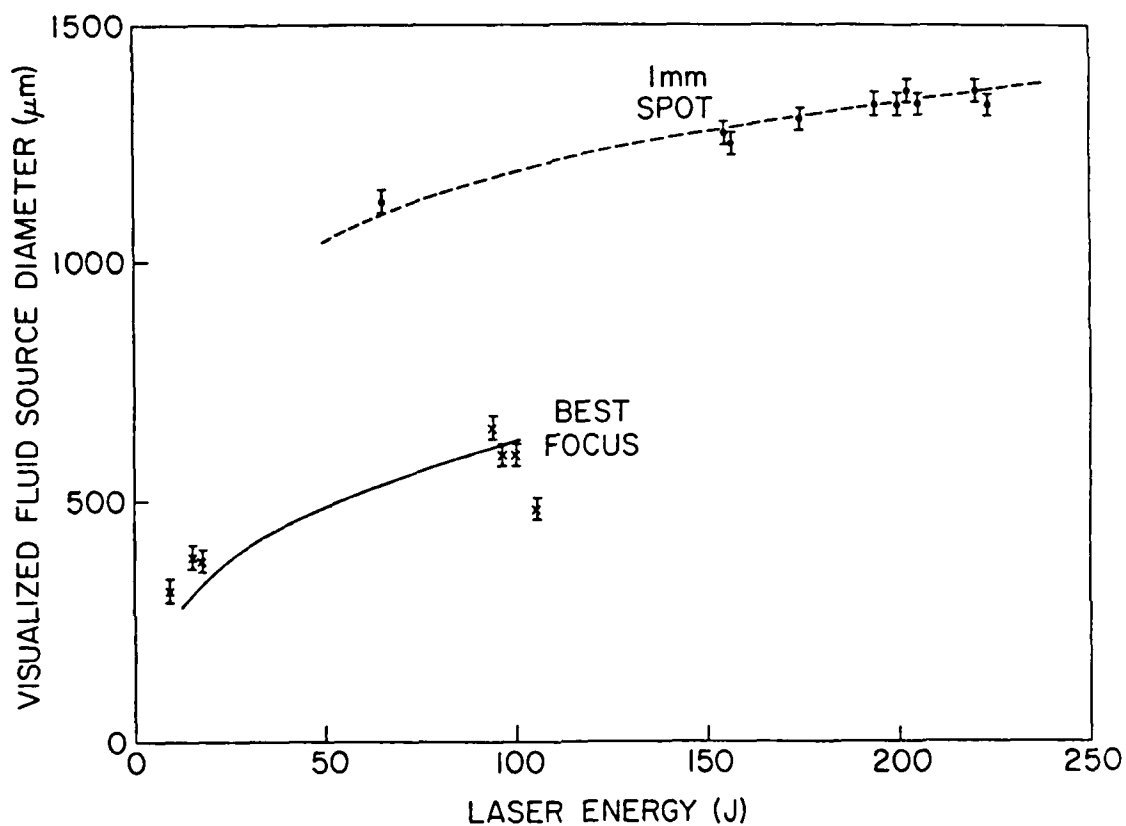
8

Fig. 5 Variation of fluid source diameter (data points) with laser energy for the two laser focal conditions shown in Fig. 3. Curves show the location of 2×10^{11} W/cm^2 intensity in the wings of the focal profile as function of laser energy for these same two focal conditions.

Fig. 4) while assuming initial ionization everywhere on the target.

If the fluid source size is entirely determined by the shape of the wings of the laser focal distribution, one might infer that the effects of lateral energy transport at the edges of the focal spot are minimal or that the lateral energy flow does not result in a high plasma temperature at the focal periphery. This empirical observation may be purely coincidental, however. Further comparisons should be made between the experiment and code at a variety of intensities and focal spot sizes before such a conclusion can be drawn.

C.   Flow Visualizations with Intentionally Perturbed Laser Intensity Distributions

Lateral energy transport between absorption and ablation surfaces can also be addressed by flow visualizations in the presence of intentionally imposed laser nonuniformities. This diagnostic complements target acceleration experiments, where velocity modulations $\Delta v/v$ have been measured as a function of imposed intensity modulations $\Delta I/I$;[5,6,11] with the tracer technique one hopes to access the modulation in ablation pressure $\Delta P/P$ which couples $\Delta v/v$ to $\Delta I/I$.[6]

The idea is qualitatively illustrated in Fig. 6, where two flow visualizations are compared. The upper image is obtained with a deeper and wider intensity minimum imposed into the center of the focal distribution. Under these conditions, target acceleration results[5] indicate little smoothing of the intensity modulation by lateral thermal transport between absorption and ablation surfaces. Indeed, the flow visualization shows two seemingly independent fluid sources, with no detectable ablation from the central region where the intensity is low. In contrast, the lower image is obtained at higher average irradiance, with a shallower and narrower intensity minimum in the center of the beam; under these conditions, smoothing of the intensity modulation is observed in the target acceleration studies.[5] Flow is now seen from the center of the focal region, although compression of this region due to inward flow of surrounding streamlines indicates that there is residual pressure modulation. More quantitative analysis of pressure modulations requires comparisons of flow visualizations with the code or development of new techniques discussed in Sec. III.C.

D.   Detection of the Rayleigh-Taylor Instability

Another potential use of the flow visualization method is for observation of hydrodynamic instability of accelerating targets.[7] Two-dimensional hydrodynamic simulations of foils unstable to Rayleigh-Taylor growth have shown that nonuniform ablation from the target surface accompanies the nonlinear state of the instability.[12] In the extreme limit of bubble-and-spike formation, these computer calculations show that all of the plasma flowing from the target can be emanating from the tips of the spikes, while none flows from the target surface in the regions of the bubbles. Preliminary flow visualization experiments have been performed to look for this nonuniform ablation,[7] using targets with periodically

10
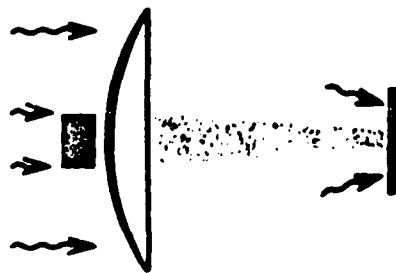
1mm

R-587

Fig. 6   Sketch at left indicates the method used to impose a minimum in the center of the quasi-near field focal profile; a strip mask blocks the center of the lens. Upper flow visualization is obtained with $I_{90} \approx 3 \times 10^{12}$ W/cm^2 within $d_{90} \approx 1450$ µm and an approximate 8-to-1 intensity modulation in the center of the beam. Conditions for lower visualization are $I_{90} \approx 6 \times 10^{12}$ W/cm^2 within $d_{90} \approx 950$ µm and a 6 to 1 dip in the beam center.

11

perturbed areal densities to seed instability growth at given wavelengths.[13] The use of these perturbed targets also allows one to selectively deposit the tracers at locations which are expected to develop into the spikes of the unstable target; one can then look for the tracer material to appear everywhere in the blowoff, signifying the expected nonuniformity in ablation. These preliminary experiments have produced flow patterns which show qualitative deviations from the usual patterns, but they are not yet fully explained.[7]

III. SPOT SPECTROSCOPY: IMPROVED DENSITY AND TEMPERATURE MEASUREMENTS

A natural extension of the tracer technique is into the area of spectroscopic plasma diagnosis.[2] As pointed out in Sec. II, it is the strong line emission from the ablated tracer material which allows visualization of 25 μm diameter streamlines within 1 mm diameter plasmas. These emitted lines can also serve for spectroscopic measurements of plasma density and temperature.[14] The new technique, spot spectroscopy, has three major advantages over standard spectroscopic methods. Standard spectroscopic measurements are integrated along a diagnostic line of sight through an inhomogeneous plasma. One could use straightforward inversion techniques to obtain spatially resolved emissivities from the chord-integrated data if the plasmas were optically thin,[14] but effects of plasma opacity on the radiation exiting the plasma are non-negligible at the higher densities of interest.[15,16] A more complicated inversion technique might also account for the spatially varying opacity; however, the more typical procedure has been to predict the plasma profile with a hydrodynamics computer code and to compare the experimentally observed spectrum with those calculated for chord integrations across the inhomogeneous plasma.[17,18] In that case, one is dependent upon the correctness of the hydrodynamics model as well as the atomic physics model, and one would obviously prefer to make more direct determinations of density and temperature. Two of the three advantages of spot spectroscopy alleviate these problems of standard spectroscopy: 1) the localized source of spectroscopic lines should eliminate chord integration across an inhomogeneous plasma, and 2) the smaller source size also reduces complicating effects due to plasma opacity. The third advantage of spot spectroscopy is that better spectral resolution can be realized, since spectral resolution with standard x-ray spectroscopy is usually limited by source broadening due to finite plasma size.

A. The Experiment

Except for the presence of the tracer in the target, the experimental arrangement for the new technique is much the same as for standard x-ray spectroscopy. As shown in the illustration of Fig. 7, the target has a single aluminum tracer spot embedded in the center of the focal region; the variety of laser irradiation conditions used are the same as those used for the flow visualization technique (see Sec. II). Aluminum line radiation in the 5-8 Å spectral region is collected by an x-ray crystal spectrograph with a viewing axis parallel to the target surface. The spectrograph slit is oriented to yield spatial resolution in one direction along the laser

ALUMINUM TARGET
SPECTRUM:

500μm

λ(Å) 6 7 8
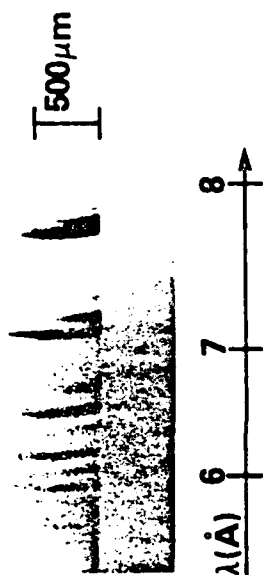
SPOTTED TARGET
SPECTRUM:

500μm

EMBEDDED Al SPOT
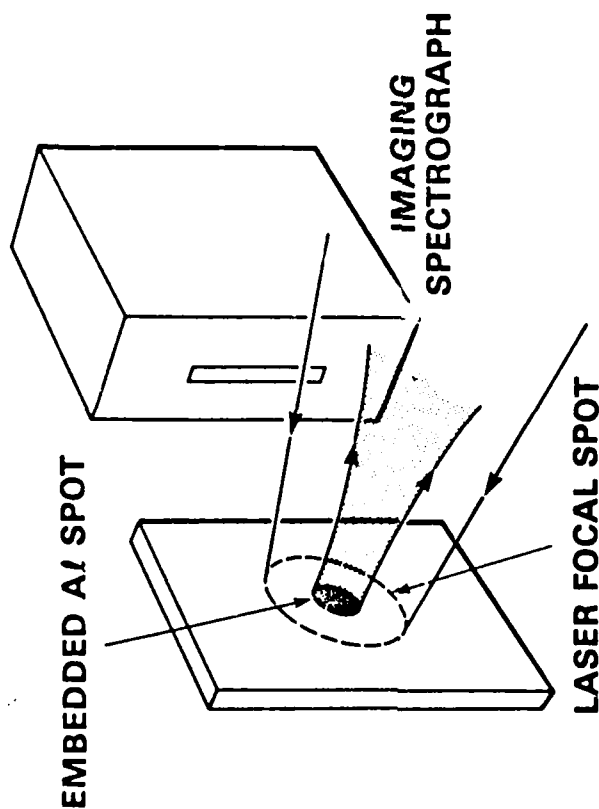
IMAGING
SPECTROGRAPH

LASER FOCAL SPOT

Fig. 7   Sketch at left shows experimental configuration for spot
spectroscopy. The upper spectrum is obtained from an Al foil target
with $I_{90} \approx 8 \times 10^{12}$ W/cm^2 within $d_{90} \approx 600$ μm and with a laser energy
of 110 J. A (CH)$_x$ foil target with a 180 μm diameter, embedded Al
spot is used to acquire the lower spectrum, with $I_{90} \approx 8 \times 10^{12}$ W/cm^2
within $d_{90} \approx 900$ μm and a laser energy of 225 J. The vertical axis
for both spectra corresponds to the laser axis, with the laser
incident from above and the target surface at bottom.

13

axis; resolution in the other two spatial dimensions results from the knowledge of the position of the localized tracer within the focal spot. The spectra are recorded on Kodak No-Screen film, for which a film model based upon an absolute calibration[20] is available. A beryllium filter of nominally 15 μm thickness protects the film from visible exposure.

More specific conditions depend upon the goals of the particular experiment. As with standard x-ray spectroscopy, one may vary the crystal type and geometry, the spectrograph slit width and magnification, and the slit-to-target distance in order to achieve the optimal tradeoff between spectral resolution, spatial resolution along the laser axis, and sensitivity. An additional variable available with spot spectroscopy is the diameter of the embedded tracer; this allows one to specify spatial resolution in the direction lateral to the laser axis, but it also impacts achievable spectral resolution and sensitivity. The specific choice of parameters for the present work are the same as those listed in Ref. 2.

Data obtained with the new technique do show the expected improvement in spectral resolution. With an aluminum foil target, as shown in Fig. 7, the spectral widths of the lines near the target surface are quite broad; the widths exceed those expected for other broadening mechanisms, and reflect source broadening due to the large Al plasma extent transverse to the laser axis. Also shown in Fig. 7 is a spectrum obtained using a $(CH)_x$ target with an embedded Al dot. Line widths near the target surface are much narrower, and sets of lines are clearly resolved that are not resolved in the Al foil spectrum.

B. Density and Temperature Profiles

Several features of the experimental spectra may be used in determinations of plasma density and temperature. In the present work, we extract temperatures from intensity ratios of various helium-like (Al XII) ionic lines to hydrogen-like (Al XIII) ionic lines. These ratios are compared with calculated ratios from a cylindrical plasma/atomic physics model of a finite, homogeneous plasma with diameter equal to the measured tracer plasma diameter.[21] At least four methods exist for density determination: 1) the often-used technique based upon the ratio between the helium-like resonance and intercombination lines,[22] 2) a method based upon the ratio between two helium-like satellite lines ($1s2s\ ^3S \rightarrow 2s2p\ ^3P$ and $1s2p\ ^3P \rightarrow 2p^2\ ^3P$),[15] 3) Stark profile analysis of higher Rydberg members, and 4) profile analysis of opacity-broadened lines near the target surface. To date, we have exploited the first two methods, though we have discovered a need to modify the first method when comparing with the experiment; preliminary work is underway on the two remaining techniques.

A problem with previous models for density measurement is identified during data reduction.[23] Variations of intensity of various spectral features with distance from the target are plotted in Fig. 8. Plots are shown of the three strongest helium-like and hydrogen-like lines used in determining temperature, but the more important curve in the figure shows the variation of the ratio of the helium-like intercombination ($He\ ^3P$) and resonance ($He\ \alpha$) lines. As mentioned above, this ratio is routinely used
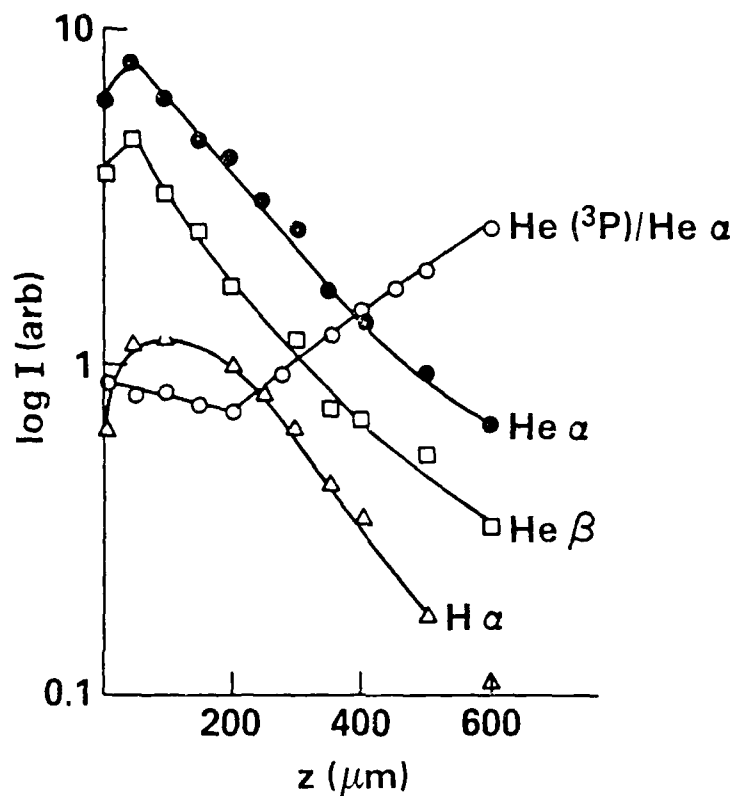
$I_{90} \approx 7.3 \times 10^{12} \text{W/cm}^2 \quad d_{90} \approx 1 \text{ mm} \quad E = 273 \text{J} \quad \tau_L = 4 \text{ns} \quad (11505)$

Fig. 8 Variation of spectral intensities of helium-like α and β and hydrogen-like α Rydberg lines with distance z from target. Also shown is the variation of the ratio of the helium-like intercombination line to the resonance line. The target is $(CH)_x$ with a 65 μm diameter, embedded Al spot. $I_{90} = 7.3 \times 10^{12}$ W/cm^2 within $d_{90} = 1$ mm and the laser energy is 273 J.
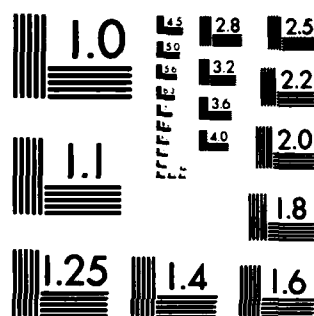
MICROCOPY RESOLUTION TEST CHART

NATIONAL BUREAU OF STANDARDS-1963-A

for density measurement. Collisional-radiative equilibrium (CRE) models indicate that this ratio should fall monotonically with increasing density except for plasma opacity effects very near to the target.[21] For $z >$ 200 μm, this expected behavior is observed and leads directly to measured densities up to 0.5 n_c. For $z <$ 200 μm, however, we observe an apparent levelling off or even an increase in the line ratio; were we to naively apply previous models to this data, we would infer a density shelf of n = 0.5 n_c for $z \leq$ 200 μm. With our improved spectral resolution, we can almost resolve satellite lines which nearly underlie the long-wavelength side of the intercombination line, and interfere with the intercombination intensity measurement. These lines, identified as the lithium-like s,t satellites [$1s^2 2s^2 S_{1/2} \rightarrow 1s(2s2p^1P)^2P_{3/2}$ and $1s^2 2s\ ^2S_{1/2} \rightarrow 1s(2s2p^1P)^2P_{1/2}$] are seen in the CRE calculations to increase in intensity relative to the intercombination line as the density increases. When the sum of the calculated intercombination and satellite intensities is compared with the data, measured densities continue to increase for z < 200 μm, as shown in Fig. 9.[23] The densities measured in this way are then in reasonable agreement with those measured for $z \leq$ 100 μm using technique (2) of the previous paragraph; for z > 100 μm, no such comparison is possible, because of insufficient intensity in the helium-like satellite lines.

The density and temperature profiles measured in this way are in fair agreement with those calculated using the two-dimensional hydrodynamics code. Error bars on measured densities are shown only for $z \leq$ 100 μm, where they reflect the range of values from the two methods available in that region; error bars for z > 100 μm are not necessarily any smaller, but are more difficult to estimate. Even without these experimental uncertainties at the lower densities, agreement in Fig. 9 is seen to be good. Agreement is not quite as good between the calculated and measured temperature profiles in Fig. 9. Temperatures near the target ($z \leq$ 100 μm) and beyond the point of peak temperature ($z >$ 400 μm) are in good agreement, but the details of the intermediate region reveal discrepancies as large as 35%; further comparisons between experiments and calculations will be required to resolve these differences.

To demonstrate that this agreement is sensitive to details of the physics contained in the code, we also show profiles in Fig. 9 from calculations without inverse bremsstrahlung absorption included. Using a simple dump of laser energy at the critical surface, the underdense density and temperature profiles are greatly changed and they no longer agree with the measured profiles. It is interesting to note that the overdense profiles obtained with inverse bremsstrahlung are very similar to those obtained with the critical dump, indicating that overdense profiles are not sensitive to details of the underdense absorption physics.

Comparisons such as these provide the most direct calibration of hydrodynamics codes. Density, temperature, and velocity profiles are the experimental observables most closely coupled to mechanisms of energy absorption and transport in laser-produced plasmas. The ability to reproduce measured profiles is, therefore, a severe test of the ability of the code to treat these physical processes.

16

DETAILS OF ABSORPTION PHYSICS GREATLY AFFECT DENSITY AND TEMPERATURE PROFILES

O 65μm Al DOT (11505)
□ 115μm Al DOT (11244)

$I_{90} \cong 7 \times 10^{12}$ W/cm^2
$d_{90} \cong 1$ mm
$\tau_L = 4$ nsec

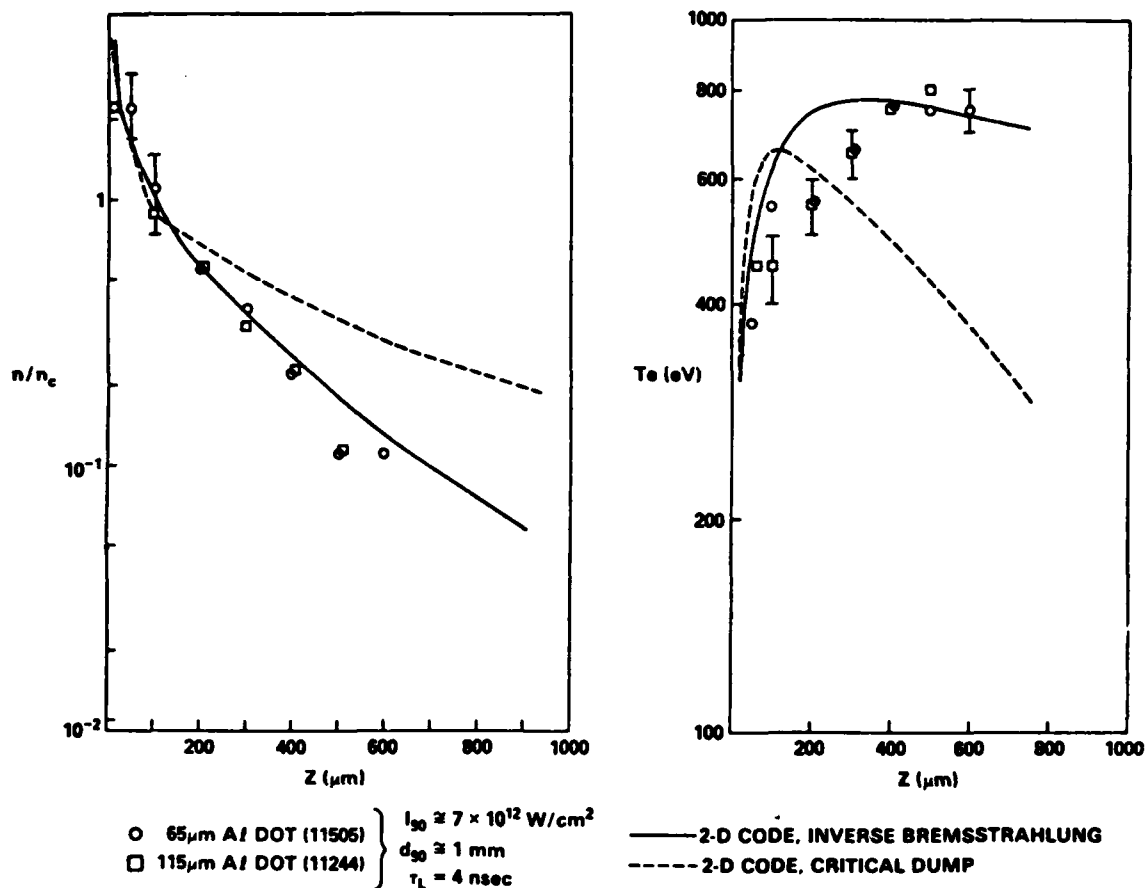——— 2-D CODE, INVERSE BREMSSTRAHLUNG
----- 2-D CODE, CRITICAL DUMP

Fig. 9 Data points show density and temperature profiles from spot spectroscopy with 65 μm (o) and 115 μm (□) diameter Al dots. Experimental conditions are $I_{90} \approx 7 \times 10^{12}$ W/cm^2 within $d_{90} \approx 1$ mm. 2-D code calculations for the same conditions are shown by the solid curve. The sensitivity of the agreement between code and experiment to details of the code physics is shown by the dotted curve, generated with the 2-D code altered to neglect inverse bremsstrahlung and to dump all energy at critical density.

17

C.   Caveats and Future Work

At least two sets of caveats regarding this work should be pointed out.   First, there are three assumptions which we make when reducing the data regarding the spatial qualities of the spectroscopic information.   As pointed out in Sec. II.B, the plasma/atomic physics model with which the data are compared simulates a homogeneous cylinder of plasma; the implicit assumption here is that the Al tracer plasma is nearly homogeneous in the radial direction.   We also assume that the Al tracer plasma equilibrates with the surrounding CH plasma if tracer spot diameters are kept sufficiently small.   This allows us to compare the spectroscopic measurements of density and temperature (which reflect conditions within the Al tracer plasma) with the results of the hydro-code (which simulates a CH target with no Al tracer) in Fig. 9.   These first two assumptions seem to be supported by the measured profiles in Fig. 9, where reduced data from two shots with different tracer diameters are shown to agree.   A third assumption is that the spectrum emitted at a given distance z from the target is determined by the density and temperature at that position, with negligible effects due to photon pumping from higher density tracer plasma closer to the target.   This assumption will be tested using the above-mentioned plasma/atomic physics model.

A second set of caveats concerns the temporal qualities of the spectroscopic information.   The present data is time-integrated; in making the comparison in Fig. 9 with an instantaneous profile from the hydro-code (at a time near the peak of the laser pulse), we are implicitly assuming that the hydrodynamics is nearly in steady state.   It is appropriate to recall the experimental inferences discussed in Sec. II.A, which support this assumption.   By comparing the measurements with a CRE model, we are also making assumptions regarding the steadiness of the atomic physics.   As the plasma flows through a given volume at a distance z from the target, we assume that its residence time in that volume is sufficiently long that states of ionization and excitation approach the equilibrium conditions appropriate for $n(z)$ and $T(z)$.   This assumption is weakest far from the target surface, where relaxation times increase with decreasing plasma density.   In this case, the state of plasma ionization and excitation becomes dependent upon conditions that exist upstream in the hydrodynamic flow, and the temperature determined by spot spectroscopy may reflect an ionization temperature rather than the local electron temperature.

In future work, time-resolved measurements of the profiles should provide a more direct answer to this second set of questions.   These measurements, as pointed out in Ref. 2, might be obtained by replacing the film with an x-ray streak camera.   An alternative approach is to bury a tracer spot of thickness t at a depth d within the target.   By varying the depth d and thickness t of the tracer on a shot-by-shot basis, one may vary the time interval during which the tracer emission occurs.

Future work may also allow us to satisfy the need for measurements of lateral profiles.   As mentioned in the introduction, the use of finite focal spots on planar targets causes the problem to become two-dimensional, and simultaneous measurement of axial and lateral profiles is desirable.

By changing the orientation of the spectrograph, one can take full advantage of its two-dimensional imaging capability. Then, using a target identical to those used in flow visualizations (Fig. 1), one obtains an image of the visualized flow in each spectral line detected by the spectrograph. In principle, this technique should allow determination of the desired profiles. Quantitative studies of lateral variations in plasma pressure, as discussed in Sec. II.C, may then be feasible.

IV.   LAYERED TRACERS: VELOCITY PROFILE AND ABLATION RATE MEASUREMENTS

Further applications of tracers become available with the use of layered tracer spots. Layered-target methods, suggested originally by G. Dahlbacka and developed by NRL,[24] facilitated studies of axial transport through measurements of mass ablation.[25] Here, we propose the marriage of layered-target techniques with our new tracer methods for measurements of fluid velocity profiles and improved measurements of mass ablation rates.

Use of a layered tracer spot should allow direct and time-resolved measurement of fluid velocity profiles. Before tracers, velocity profiles of the fluid were not measured, despite their importance for interpreting stimulated Brillouin scattering observations. In Ref. 3, we demonstrated an indirect method for inferring time-averaged profiles, but tracers also allow a direct and time-resolved measurement. As shown in Fig. 10, one can fabricate a tracer spot from alternating layers of two materials with distinguishable x-ray emissivities. As each successive layer ablates from the target, the progress through the blowoff plasma of the interface between layers may be observed with an x-ray streak camera; the camera slit is oriented to give spatial resolution along the laser axis. The $z(t)$ curves generated by the multiple interfaces may be inverted to give the velocity profiles $u(z)$ with time resolution.

The above data also yields the ablation rate through each layer of the tracer spot. This is an improvement over the original layered-target measurement of ablation rate,[25] because localization of the layers within the tracer spot alleviates complications due to variations in laser intensity across the irradiated region.

V.   SUMMARY

With tracer methods still in their infancy, we see several new techniques which are capable of addressing a variety of interesting and important physics issues. The measurements of density and temperature profiles shown in Sec. II and the proposed measurement of velocity profile discussed in Sec. IV are an important adjunct to experiments related to laser absorption in the underdense plasma. If overdense profiles can be measured with sufficient precision, issues of axial transport of energy inward from the absorption region may be treated; the applicability of the time-resolved ablation rate measurement to this problem is also clear. We have already begun to apply the flow visualization technique to questions of lateral energy spread due to finite focal spot size or due to laser
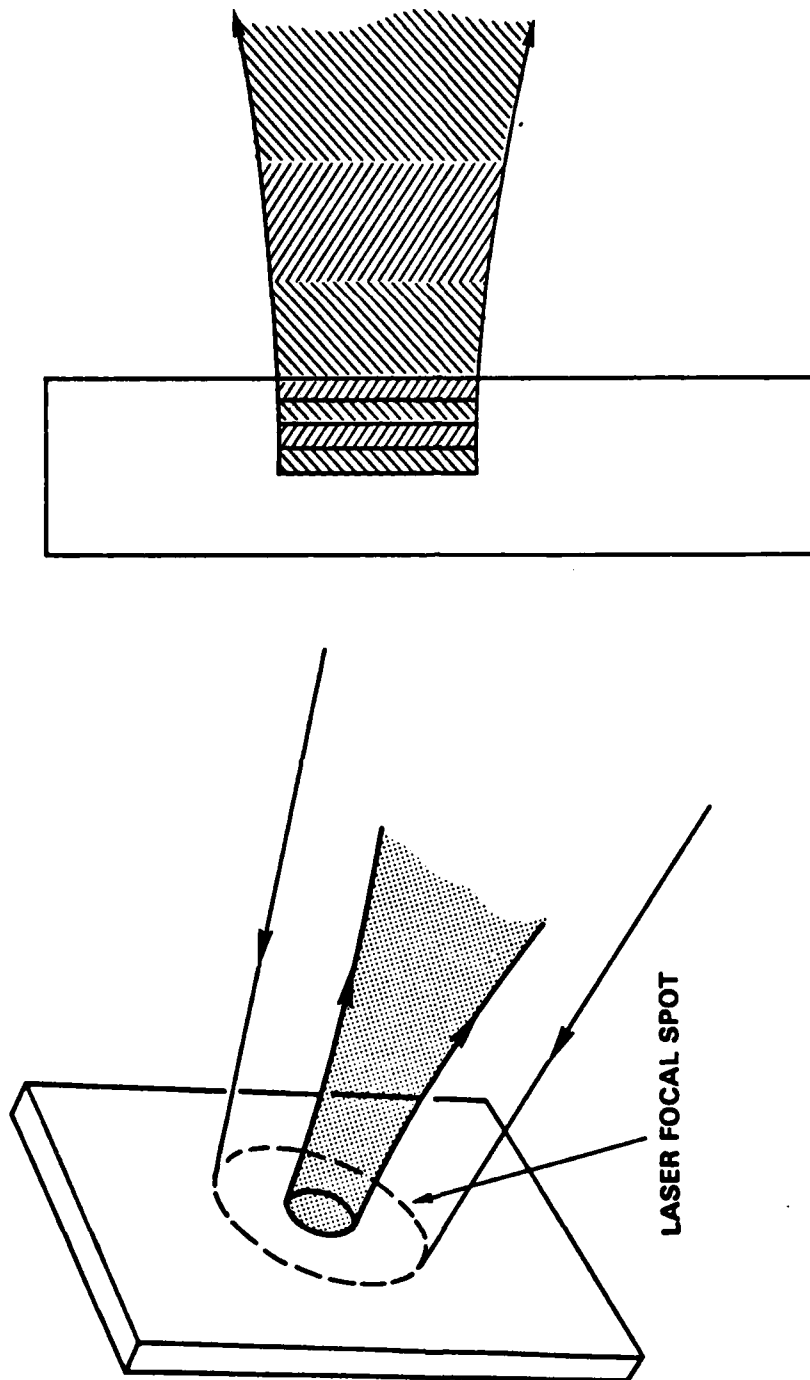
19

LASER FOCAL SPOT

Fig. 10   Illustration of proposed method for time-resolved measurement of velocity profile and for improved ablation rate measurement. At left, the target has a single tracer spot as for spot spectroscopy. The cross-section of the target, at right, shows that the embedded spot is now made of alternating layers of two materials, which ablate sequentially in time during laser irradiation.

nonuniformities, and proposed spectroscopic methods can make this more quantitative. Experiments are also underway to test the use of tracers for detection of Rayleigh-Taylor instability. Many of these measurements provide valuable data for calibration of the hydrodynamics codes upon which we rely for predictions of high-gain target performance. As many of the current ideas for use of tracers are proven and as new ideas continue to surface, we anticipate an expanding role for these methods in experiments related to the physics of laser-matter interaction and to inertial confinement fusion.

VI.   ACKNOWLEDGEMENTS

References

1. M.J. Herbst and J. Grun, Phys. Fluids 24, 1917 (1981).

2. M.J. Herbst, P.G. Burkhalter, J. Grun, R.R. Whitlock, and M. Fink, Rev. Sci. Instr. 53, 1418 (1982).

3. M.J. Herbst, P.G. Burkhalter, J. Grun, S.P. Obenschain, J.A. Stamper, F.C. Young, E.A. McLean, B.H. Ripin, and R.R. Whitlock, NRL Memorandum Report 4893 (1982, unpublished).

4. B.H. Ripin, NRL Memorandum Report 3684 (1977, unpublished).

5. S.P. Obenschain, J. Grun, B.H. Ripin, and E.A. McLean, Phys. Rev. Lett. 46, 1402 (1981).

6. J. Grun, S.P. Obenschain, B.H. Ripin, R.R. Whitlock, E.A. McLean, J. Gardner, M.J. Herbst, and J.A. Stamper, NRL Memorandum Report 4747 (1982, to be published).

7. J. Grun, S.P. Obenschain, R.R. Whitlock, M.J. Herbst, B.H. Ripin, E.A. McLean, M. Emery, and J. Gardner, Bull. Am. Phys. Soc. 26, 1023 (1981); J. Grun, M.J. Herbst, E.A. McLean, S.P. Obenschain, B.H. Ripin, J.A. Stamper, R.R. Whitlock, and F.C. Young, Proc. 12th Anomalous Absorption Conference (1982, to be published).

8. J.H. Gardner, S.E. Bodner, J.P. Boris, M.H. Emery, M. Fritts, and M.J. Herbst, to appear in Laser Interaction and Related Plasma Phenomena, V. 6, ed. H. Hora.

9. M.J. Herbst, J.A. Stamper, R.H. Lehmberg, R.R. Whitlock, F.C. Young, J. Grun, and B.H. Ripin, to appear in Proceedings of the 1981 Topical Conference on Symmetry Aspects of Inertial Fusion Implosions, ed. by S. Bodner, NRL, and NRL Memorandum Report No. 4983.

10. J. Grun, R. Decoste, B.H. Ripin, and J. Gardner, Appl. Phys. Lett. 39, 545 (1981).

11. R.R. Whitlock, S.P. Obenschain, and J. Grun, Appl. Phys. Lett. 41, 429 (1982).

12. M.H. Emery, J.H. Gardner, and J.P. Boris, Phys. Rev. Lett. 48, 677 (1982).

13. B.H. Ripin, S.P. Obenschain, J. Grun, M.J. Herbst, E.A. McLean, J.A. Stamper, R.R. Whitlock, J.M. McMahon, and S.E. Bodner, Bull. Am. Phys. Soc. 25, 946 (1980).

14. H.R. Griem, Plasma Spectroscopy (McGraw-Hill, New York, 1964).

15. D. Duston and J. Davis, Phys. Rev. 21 A, 932 (1980).

16. J.P. Apruzese, P.C. Kepple, K.G. Whitney, J. Davis, and D. Duston, Phys. Rev. $\underline{24}$ A, 1001 (1981).

17. D. Duston, J. Davis, and P.C. Kepple, Phys. Rev. $\underline{24}$ A, 1505 (1981).

18. K.G. Whitney and P.C. Kepple, J. Quant. Spectrosc. Radiat. Transfer $\underline{27}$, 281 (1982).

19. D.B. Brown, J.W. Criss, and L.S. Birks, J. Appl. Phys. $\underline{47}$, 3722 (1976).

20. C.M. Dozier, D.B. Brown, L.S. Birks, P.B. Lyons, and R.F. Benjamin, J. Appl. Phys. $\underline{47}$, 3732 (1976).

21. D. Duston and J. Davis, Phys. Rev. $\underline{21}$ A, 1664 (1980).

22. V.A. Boiko, S.A. Pikuz and A.Ya. Faenov, J. Phys. $\underline{12}$ B, 1889 (1979).

23. P.G. Burkhalter, M.J. Herbst, R.R. Whitlock, and J. Grun, Proceedings 1982 IEEE International Conference on Plasma Science.

24. F.C. Young, R.R. Whitlock, R. Decoste, B.H. Ripin, D.J. Nagel, J.A. Stamper, J.M. McMahon, and S.E. Bodner, Appl. Phys. Lett. $\underline{30}$, 45 (1977).

25. B.H. Ripin, R. Decoste, S.P. Obenschain, S.E. Bodner, E.A. McLean, F.C. Young, R.R. Whitlock, C.M. Armstrong, J. Grun, J.A. Stamper, S.H. Gold, D.J. Nagel, R.H. Lehmberg, and J.M. McMahon, Phys. Fluids $\underline{23}$, 1012 (1980) and $\underline{24}$, 990 (1981).

MED

8